JSCSEN 72(11)1039–1169(2007)

UDC 54:66

ISSN 0352–5139

Journal of the Serbian Chemical Society 72, No. 11, 1039–1169 (2007)

Journal of the Serbian Chemical Society

Electronic version

VOLUME 72

NO 11

BELGRADE 2007

Journal of the Serbian Chemical Society
JSCS@tmf.bg.ac.yu • www.shd.org.yu/JSCS

ISSN 0352–5139
J. Serb. Chem. Soc. Vol. 72, No. 11 (2007)

CONTENTS

Published by the Serbian Chemical Society
Karnegijeva 4/III, 11120 Belgrade, Serbia
Printed by the Faculty of Technology and Metallurgy
Karnegijeva 4, P.O. Box 35-03, 11120 Belgrade, Serbia

Journal of the Serbian Chemical Society
JSCS@tmf.bg.ac.yu • www.shd.org.yu/JSCS

J. Serb. Chem. Soc. 72 (11) 1039–1044 (2007)
JSCS–3637

UDC 547.633.6+547.484:542.913
Original scientific paper

Synthesis and characterization of heterocyclic substituted fluoran compounds

SACHIN V. PATEL, MANISH P. PATEL* and RANJAN G. PATEL

Department of Chemistry, Sardar Patel University, Vallabh Vidyanagar–388 120, Gujarat, India

(Received 5 September 2005, revised 1 February 2006)

Abstract: New quinazolinone-substituted fluoran compounds were synthesized by reaction of keto acid, 2'-carboxy-2-hydroxy-4-*N*-pyrrolidinylbenzophenone with different quinazolinone derivatives in the presence of conc. sulphuric acid. All the synthesized fluoran compounds were characterized by spectroscopic methods (IR, ^{1}H-NMR and UV–visible spectroscopy) and elemental analysis. The fluoran compounds are colourless or nearly colourless and develop colour on contact with electron-accepting compounds.

Keywords: fluoran, keto acid, synthesis, quinazolinone.

INTRODUCTION

Spiro[isobenzofuran-1(3*H*),9'-xanthen]-3-one,[1] commonly known as fluoran, is a parent compound of a class of leuco dyes. Fluoran compounds are substantially colourless or nearly colourless and produce colouration when they are brought into intimate contact with electron-accepting substances, such as acid clays, activated clays, phenol formaldehyde resins, bisphenol, *etc*. Fluoran compounds containing various heterocycles, such as pyrrole,[2] pyridine,[3] morpholine,[4] benzothiazole[5] and piperazine,[6] have been reported earlier. Fluoran compounds are widely used in a variety of fields, such as pressure sensitive adhesive tap,[7] paint and toys,[8] thermochromic polymers,[9] thermochromic printing inks,[10] carbonless copying papers,[11] *etc*. In the present paper, the synthesis and characterization of nearly colourless pyrrolidinyl fluoran compounds prepared from various substituted quinazolinones are described.

EXPERIMENTAL

All the used raw materials were of commercial grade and were further purified by recrystallization and redistillation before use. All melting points (m.p.) are uncorrected and expressed in °C. The IR spectra of all compounds were recorded on a Nicolet Impact-400D FTIR spectrophotometer using the KBr pellet technique. The ^{1}H-NMR spectra were recorded on a Hitachi R-1500 instrument (60 MHz) using TMS as the internal standard. Chemical shifts are given in δ (ppm). The ab-

* Corresponding author. E-mail: patelmanish1069@yahoo.com
doi: 10.2298/JSC0711039P

sorption spectra (λ_{max}) of the compounds in chloroform and 95 % acetic acid were recorded on a Shimadzu UV-240 instrument.

General procedure for the preparation of ***A*** *and* $\boldsymbol{B_{1a\text{-}f}}$ *and* $\boldsymbol{B_{2a\text{-}f}}$

A mixture of 81.5 g 1-(3-hydroxyphenyl)pyrrolidine (**a**), 74 g phthalic anhydride (**b**) and 350 ml toluene were stirred at reflux for 6–7 h under dry conditions. The reaction mixture was cooled to room temperature and the precipitate was filtered off through a funnel, washed with methanol to obtain yellow coloured 2'-carboxy-2-hydroxy-4-*N*-pyrrolidinylbenzophenone (**A**),[12] m.p. 196–8 °C (Scheme 1).

Various quinazolinone derivatives $\mathbf{B_{1a\text{-}f}}$ and $\mathbf{B_{2a\text{-}f}}$ were prepared as reported in the literature.[13,14]

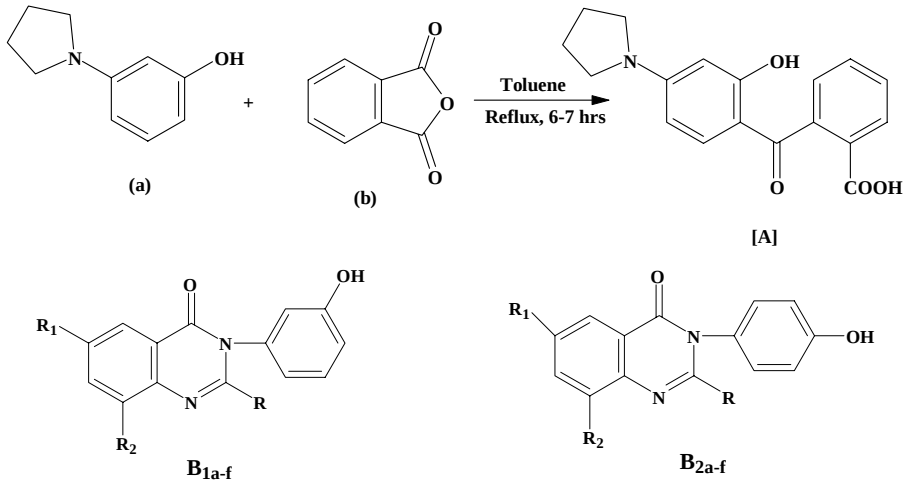

Scheme 1. 2'-Carboxy-2-hydroxy-4-*N*-pyrrolidinylbenzophenone [A]; quinazolinones $\mathbf{B_{1a\text{-}f}}$ and $\mathbf{B_{2a\text{-}f}}$; R = CH_3, C_6H_5; R_1 and R_2 = H, Br.

Preparation of fluoran compounds $\boldsymbol{C_{1a\text{-}f}}$ *and* $\boldsymbol{C_{2a\text{-}f}}$

2'-Carboxy-2-hydroxy-4-*N*-pyrrolidinylbenzophenone (**A**) (0.01 mol) and the corresponding quinazolinone $\mathbf{B_{1a\text{-}f}}$ or $\mathbf{B_{2a\text{-}f}}$ (0.01 mol) were dissolved in conc. H_2SO_4 (10 ml) and stirred at 80–85 °C for 56 h. After the completion of the reaction, the reaction mixture was poured into ice-cold water. The precipitate was filtered and washed with water. The acid-free compound was charged into water and the pH was made alkaline (pH 9–10) using aqueous NaOH to obtain the corresponding light coloured fluoran compound (Scheme 2, Table I). The product was filtered and washed with water until neutral. TLC showed a purple-coloured single spot in the solvent system toluene:ethyl acetate 7:3 (v/v).

RESULTS AND DISCUSSION

The results of the chemical and spectroscopic analyses of the prepared compounds are given below.

*2-Methyl-3-(3-oxo-6'-*N*-pyrrolidinylspiro[isobenzofuran-1(*3H*),9'-[*9H*]xanthen--3'-yl]-4(*3H*)-quinazolinone* (**C_{1a}**): Anal. calcd. for $C_{33}H_{25}N_3O_4$: C, 75.12; H, 4.77; N, 7.96. Found: C, 75.42; H, 4.45; N, 7.79. IR (KBr, cm^{-1}): 3070, 2858, 1441, 1355 (Ar-CH_3); 1775 (C=O group of lactone ring); 1660 (−C=O group of quinazolinone); 1595 (C=N); 1332 (C−N stretching of phenyl pyrrolidine). ^{1}H-NMR ($CDCl_3$, δ, ppm): 7.0–7.7 (*m*, 14H, ArH), 3.2 (*t*, 4H, NCH_2CH_2), 2.2 (*s*, 3H, $ArCH_3$), 1.9 (*m*, 4H, NCH_2CH_2).

3-(3-oxo-6'-N-*pyrrolidinylspiro[isobenzofuran-1(3*H*),9'-[9*H*]xanthen]-3'-yl]--4(3*H*)-quinazolinone* (**C_{1b}**): Anal. calcd. for $C_{38}H_{27}N_3O_4$: C, 77.40; H, 4.61; N, 7.12. Found: C, 77.35; H, 4.22; N, 7.03. IR (KBr, cm^{-1}): 1770 (C=O group of lactone ring); 1650 (C=O group of quinazolinone); 1595 (C=N); 1330 (C−N stretching of phenyl pyrrolidine). ^{1}H-NMR ($CDCl_3$, δ, ppm): 6.5–7.8 (*m*, 19H, ArH), 3.2 (*t*, 4H, NCH_2CH_2), 1.9 (*m*, 4H, NCH_2CH_2).

6-Bromo-2-methyl-3-(3-oxo-6'-N-*pyrrolidinylspiro[isobenzofuran-1(3*H*),9'--[9*H*]xanthen]-3'-yl]-4(3*H*)-quinazolinone* (**C_{1c}**): Anal. calcd. for $C_{33}H_{24}BrN_3O_4$: C, 65.35; H, 3.98; N, 6.92. Found: C, 65.78; H, 3.79; N, 6.53. IR (KBr, cm^{-1}): 3080, 2910, 1465, 1356 ($ArCH_3$); 1760 (C=O group of lactone ring); 1680 (C=O group of quinazolinone); 1605 (C=N); 1336 (C–N stretching of phenyl pyrrolidine); 565 (C−Br). ^{1}H-NMR ($CDCl_3$, δ, ppm): 7.0–8.1 (*m*, 13H, ArH), 3.2 (*t*, 4H, NCH_2CH_2), 2.2 (*s*, 3H, $ArCH_3$), 1.9 (*m*, 4H, NCH_2CH_2).

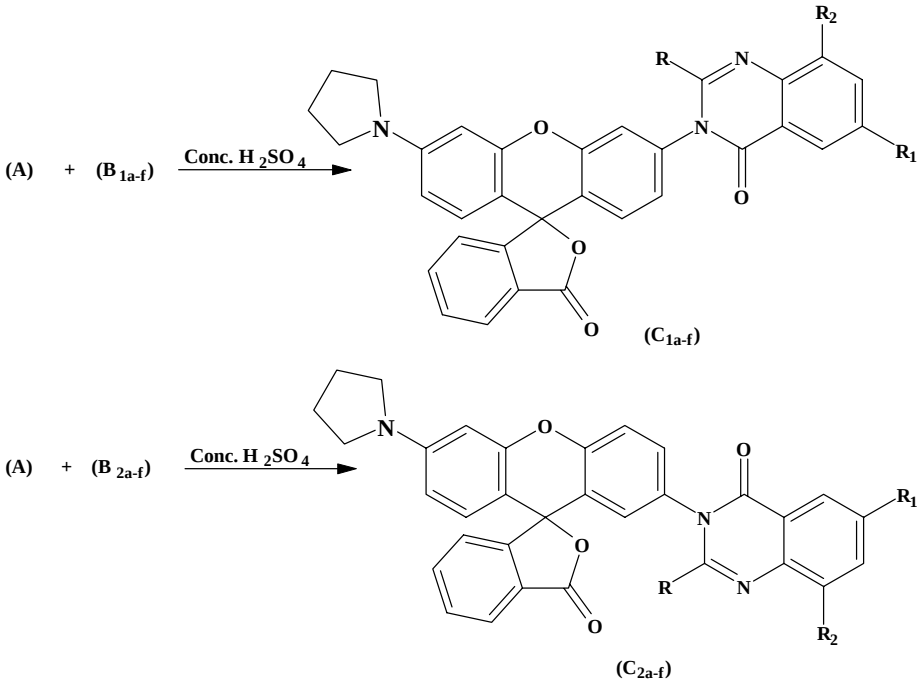

Scheme 2. Fluorans **C_{1a-f}** and **C_{2a-f}**.

6-Bromo-3-(3-oxo-6'-N-*pyrrolidinylspiro[isobenzofuran-1(3*H*),9'-[9*H*]xanthen]-3'-yl]-2-phenyl-4(3*H*)-quinazolinone* (**C_{1d}**): Anal. calcd. for $C_{38}H_{26}BrN_3O_4$: C, 68.27; H, 3.92; N, 6.28. Found: C, 68.42; H, 3.89; N, 6.42. IR (KBr, cm^{-1}): 1760 (C=O group of lactone ring); 1670 (C=O group of quinazolinone); 1600 (C=N); 1332 (C−N stretching of phenyl pyrrolidine); 545 (C−Br). ^{1}H-NMR ($CDCl_3$, δ, ppm): 7.0–8.3 (*m*, 18H, ArH), 3.2 (*t*, 4H, NCH_2CH_2), 1.9 (*m*, 4H, NCH_2CH_2).

6,8-Dibromo-2-methyl-3-(3-oxo-6'-N-*pyrrolidinylspiro[isobenzofuran-1(3*H*),-9'-[9*H*]xanthen]-3'-yl]-4(3*H*)-quinazolinone* (**C$_{1e}$**): Anal. calcd. for $C_{33}H_{23}Br_2N_3O_4$: C, 57.83; H, 3.38; N, 6.13. Found: C, 57.62; H, 3.12; N, 6.34. IR (KBr, cm^{-1}): 3010, 2880, 1445, 1350 ($ArCH_3$); 1765 (C=O group of lactone ring); 1650 (C=O group of quinazolinone); 1594 (C=N); 1310 (C−N stretching of phenyl pyrrolidine); 532 (C−Br). ^{1}H-NMR ($CDCl_3$, δ, ppm): 6.9–7.4 (*m*, 12H, ArH), 3.2 (*t*, 4H, NCH_2CH_2), 2.2 (*s*, 3H, $ArCH_3$), 1.9 (*m*, 4H, NCH_2CH_2).

6,8-Dibromo-3-(3-oxo-6'-N-*pyrrolidinylspiro[isobenzofuran-1(3*H*),9'-[9*H*]xanthen]-3'-yl]-2-phenyl-4(3*H*)-quinazolinone* (**C$_{1f}$**): Anal. calcd. for $C_{38}H_{25}Br_2N_3O_4$: C, 61.06; H, 3.37; N, 5.62. Found: C, 61.27; H, 3.28; N, 5.71. IR (KBr, cm^{-1}): 1775 (C=O group of lactone ring); 1650 (C=O group of quinazolinone); 1595 (C=N); 1320 (C−N stretching of phenyl pyrrolidine); 587 (C−Br). ^{1}H-NMR: ($CDCl_3$, δ, ppm): 7.0–7.3 (*m*, 17H, ArH), 3.2 (*t*, 4H, NCH_2CH_2), 1.9 (*m*, 4H, NCH_2CH_2).

2-Methyl-3-(3-oxo-6'-N-*pyrrolidinylspiro[isobenzofuran-1(3*H*),9'-[9*H*]xanthen--2'-yl]-4(3*H*)-quinazolinone* (**C$_{2a}$**): Anal. calcd. for $C_{33}H_{25}N_3O_4$: C, 75.12; H, 4.77; N, 7.96. Found: C, 75.37; H, 4.84; N, 7.84. IR (KBr, cm^{-1}): 3052, 2880, 1472, 1362 ($ArCH_3$); 1760 (C=O group of lactone ring); 1680 (C=O group of quinazolinone); 1590 (C=N); 1330 (C−N stretching of phenyl pyrrolidine). ^{1}H-NMR ($CDCl_3$, δ, ppm): 7.0–8.1 (*m*, 14H, ArH), 3.2 (*t*, 4H, NCH_2CH_2), 2.2 (*s*, 3H, $ArCH_3$), 1.9 (*m*, 4H, NCH_2CH_2).

3-(3-oxo-6'-N-*pyrrolidinylspiro[isobenzofuran-1(3*H*),9'-[9*H*]xanthen]-2'-yl]--4(3*H*)-quinazolinone* (**C$_{2b}$**): Anal. calcd. for $C_{38}H_{27}N_3O_4$: C, 77.40; H, 4.61; N, 7.12. Found: C, 77.58; H, 4.23; N, 7.29. IR (KBr, cm^{-1}): 1760 (C=O group of lactone ring); 1660 (C=O group of quinazolinone); 1600 (C=N); 1333 (C−N stretching of phenyl pyrrolidine). ^{1}H-NMR ($CDCl_3$, δ, ppm): 7.5–8.3 (*m*, 19H, ArH), 3.2 (*t*, 4H, NCH_2CH_2), 1.9 (*m*, 4H, NCH_2CH_2).

6-Bromo-2-methyl-3-(3-oxo-6'-N-*pyrrolidinylspiro[isobenzofuran-1(3*H*),9'--[9*H*]xanthen]-2'-yl]-4(3*H*)-quinazolinone* (**C$_{2c}$**): Anal. calcd. for $C_{33}H_{24}BrN_3O_4$: C, 65.35; H, 3.98; N, 6.92. Found: C, 65.69; H, 3.76; N, 6.84. IR (KBr, cm^{-1}): 3060, 2852, 1492, 1362 ($ArCH_3$); 1755 (C=O group of lactone ring); 1650 (C=O group of quinazolinone); 1600 (C=N); 1325 (C−N stretching of phenyl pyrrolidine); 590 (C−Br). ^{1}H-NMR ($CDCl_3$, δ, ppm): 6.5–8.2 (*m*, 13H, ArH), 3.2 (*t*, 4H, NCH_2CH_2), 2.17 (*s*, 3H, $ArCH_3$), 1.9 (*m*, 4H, NCH_2CH_2).

6-Bromo-3-(3-oxo-6'-N-*pyrrolidinylspiro[isobenzofuran-1(3*H*),9'-[9*H*]xanthen]-2'-yl]-2-phenyl-4(3*H*)-quinazolinone* (**C$_{2d}$**): Anal. calcd. for $C_{38}H_{26}BrN_3O_4$: C, 68.27; H, 3.92; N, 6.28. Found: C, 68.32; H, 3.88; N, 6.47. IR (KBr, cm^{-1}): 1765 (C=O group of lactone ring); 1660 (C=O group of quinazolinone); 1595 (C=N); 1325 (C−N stretching of phenyl pyrrolidine); 582 (C−Br). ^{1}H-NMR ($CDCl_3$, δ, ppm): 6.9–8.3 (*m*, 18H, ArH), 3.2 (*t*, 4H, NCH_2CH_2), 1.9 (*m*, 4H, NCH_2CH_2).

6,8-Dibromo-2-methyl-3-(3-oxo-6'-N-*pyrrolidinylspiro[isobenzofuran-1(3*H*),-9'-[9*H*]xanthen]-2'-yl]-4(3*H*)-quinazolinone* (**C$_{2e}$**): Anal. calcd. for $C_{33}H_{23}Br_2N_3O_4$:

C, 57.83; H, 3.38; N, 6.13. Found: 57.71; H, 3.14; N, 6.24. IR (KBr, cm^{-1}): 3045, 2895, 1425, 1350 ($ArCH_3$); 1770 (C=O group of lactone ring); 1645 (C=O group of quinazolinone); 1590 (C=N); 1310 (C−N stretching of phenyl pyrrolidine); 562 (C−Br). ^{1}H-NMR ($CDCl_3$, δ, ppm): 7.3–8.1 (*m*, 12H, ArH), 3.3 (*t*, 4H, NCH_2CH_2), 2.2 (*s*, 3H, $ArCH_3$), 1.9 (*m*, 4H, NCH_2CH_2).

6,8-Dibromo-3-(3-oxo-6'-N-*pyrrolidinylspiro[isobenzofuran-1(3*H*),9'-[9*H*]xanthen]-3'-yl]-2-phenyl-4(3*H*)-quinazolinone* (**C_{2f}**): Anal. calcd. for $C_{38}H_{25}Br_2N_3O_4$: C, 61.06; H, 3.37; N, 5.62. Found: C, 61.37; H, 3.59; N, 5.79. IR (KBr, cm^{-1}): 1765 (C=O group of lactone ring); 1670 (C=O group of quinazolinone); 1600 (C=N); 1320 (C−N stretching of phenyl pyrrolidine); 555 (C−Br). ^{1}H-NMR ($CDCl_3$, δ, ppm): 6.3–8.1 (*m*, 17H, ArH), 3.2 (*t*, 4H, NCH_2CH_2), 1.9 (*m*, 4H, NCH_2CH_2).

TABLE I. Physical data of fluorans **C_{1a-f}** and **C_{2a-f}**

Comp. No.	Compound C			Yield, %	M. p., °C	λ_{max} / nm		Colour on silica gel
	R	R_1	R_2			In 95 % acetic acid	In chloroform	
C_{1a}	CH_3	H	H	67	268	528, 369, 275	267	Purple
C_{1b}	C_6H_5	H	H	62	223	535, 318, 281	284	Purple
C_{1c}	CH_3	Br	H	60	250	532, 316, 284	280	Purple
C_{1d}	C_6H_5	Br	H	63	294	547, 316, 289	290	Purple
C_{1e}	CH_3	Br	Br	58	262	500, 379, 273	273	Purple
C_{1f}	C_6H_5	Br	Br	69	208	530, 367, 276	252	Purple
C_{2a}	CH_3	H	H	66	234	536, 380, 278	252	Purple
C_{2b}	C_6H_5	H	H	62	182	546, 378, 282	249	Purple
C_{2c}	CH_3	Br	H	61	225	549, 366, 279	247	Purple
C_{2d}	C_6H_5	Br	H	68	252	534, 355, 280	249	Purple
C_{2e}	CH_3	Br	Br	60	308	502, 365, 280	249	Purple
C_{2f}	C_6H_5	Br	Br	68	321	532, 372, 280	254	Purple

The IR spectra of all the synthesised fluoran compounds showed the disappearance of the characteristic absorption band of the OH group of quinazolinone and the appearance of C–N stretching of the phenyl pyrrolidine group and also appearance of the C=O group of the lactone ring at 1745−1790 cm^{-1} and at 1640−1700 cm^{-1} for the C=O group of quinazolinone and other characteristic absorption bands for the rest of the molecules.

Absorption spectra (λ_{max}) of the compounds in chloroform and 95 % acetic acid showed a single peak in chloroform due to the lactone ring and three peaks in 95 % acetic acid due to the quinone, zwitterion and lactone forms.[15,16]

CONCLUSIONS

The chromogenic fluoran compounds of the present investigation are soluble in organic solvent without colouration and show spontaneous colour formation in aqueous solution and acidic colour-activating substances.

И З В О Д

ДОБИЈАЊЕ И КАРАКТЕРИЗАЦИЈА ФЛУОРАНА СУПСТИТУИСАНИХ ХЕТЕРОЦИКЛИМА

SACHIN V. PATEL, MANISH P. PATEL и RANJAN G. PATEL

Department of Chemistry, Sardar Patel University, Vallabh Vidyanagar–388 120, Gujarat, India

Нова једињења флуорана уз супституцију киназолиноном добијена су реакцијом кето киселине, 2'-карбокси-2-хидрокси-4-*N*-пиролидинил бензофенона и различитих деривата киназолинона у присуству концентроване сумпорне киселине. Добијена једињења флуорана окарактерисана су спектроскопским методама (IR, ^{1}H-NMR и UV-vis спектроскопијом) и елементалном анализом. Једињењења флуорана су безбојна или слабо обојена, док у додиру са електрон-акцептор једињењима постају обојена.

(Примљено 5. септембра 2005, ревидирано 1. фебруара 2006)

REFERENCES

1. R.Muthyalal, *Chemistry and Applications of Leuco dyes*, Plenum Press, New York, 1997, p.159
2. S. Spatz, US 3,989,716 [*C.A.***86**/1977 44769n]
3. A. Takashi, K. Kohichi, K. Makoto, M. Makoto, I. Hiroshi (Sumitomo Chemical Co., Ltd.), JP 73 00,168 [*C.A.***80**/1974 28468j]
4. L. F. Dixon, (Holliday Dyes & Chemical Ltd.), GB 2,097,013 [*C.A.***98**/1983 73839p]
5. P. Theodor, R. Rolf, S. Ernst (Farbwerke Hoechst A.–G.), Ger.Offen. 2,036,817 [*C.A.***76**/1972 155606v]
6. Yamamoto Synthetic Chemical Co. Ltd., Brit. 1,336,955 [*C.A.***80**/1974 122413j]
7. N. Sakai, Jpn. Kokai Tokkyo Koho, JP 2004 91,769 [*C.A.***140**/2004 272003x]
8. M. Ito, Jpn. Kokai Tokkyo Koho, JP 2004 136, 477. [*C.A.***140**/2004 397413n]
9. N. Nakasuji, T. Kataoka, H. Inagaki, S. Nakashima (Pilot Ink Co., Ltd.), U.S. 4,028,118 (1977)
10. Y. Shibahashi, N. Nakasuji, T. Kataoka, H. Inagaki, U.S. 4,425,161 (1984)
11. V. G. Atkinson (Carrs Paper Ltd.), US 6071852 (2000)
12. G. Robert, P. Jean C. (Ciba–Geigy A.G.), U.S. 4,007,195 [*C.A.***86**/1977 173071c]
13. R. G. Patel, M. P.Patel, R. G. Patel, *J. Serb. Chem. Soc.* **69** (2004) 327
14. S. V. Patel, M. P. Patel, R. G. Patel, *J. Iran Chem. Soc.* **2** (2005) 220
15. A. V. Despande, E. B. Namdas, *J. Photochem. Photobiol., A* **110** (1997) 177
16. S. Kimura, T. Kodayashi, S. Ishige, Fuji Photo Film Co. Ltd., Japan, JP 71 12,312 (1968).

Journal of the Serbian Chemical Society
JSCS@tmf.bg.ac.yu • www.shd.org.yu/JSCS

J. Serb. Chem. Soc. 72 (11) 1045–1051 (2007) UDC **Cotinus coggygria*:665.52/.54+615.281/.282(497.11)
JSCS–3638 *Original scientific paper*

Chemical composition, antibacterial and antifungal activity of the essential oils of *Cotinus coggygria* from Serbia

MIROSLAV NOVAKOVIĆ[1#], IVAN VUČKOVIĆ[1#], PEĐA JANAĆKOVIĆ[2], MARINA SOKOVIĆ[3], ANKA FILIPOVIĆ[4], VELE TEŠEVIĆ[5#] and SLOBODAN MILOSAVLJEVIĆ[5#*]

[1]Institute for Chemistry, Technology and Metallurgy, Njegoševa 12, 11000 Belgrade, [2]Faculty of Biology, Studentski trg 16, 11001 Belgrade, [3]Institute for Biological Research "Siniša Stanković", Bulevar Despota Stefana 142, 11000 Belgrade, [4]Institute of Public Health, Bulevar Despota Stefana 54a, 11000 Belgrade and [5]Faculty of Chemistry, Studentski trg 16, 11001 Belgrade, Serbia

(Received 19 December 2006, revised 6 July 2007)

Abstract: Essential oils from leaves with young branches of *Cotinus coggygria* Scop. from two localities in Serbia (Deliblatska peščara and Zemun), obtained by hydrodistillation, were analysed by GC–MS. Thirty-one component were identified from both oils and among them monoterpenic hydrocarbons were the dominant class (87.4 and 93.1 %). The dominant constituent in both essential oils was limonene (47.0 and 39.2 %). Both oils were also tested for antibacterial and antifungal activities. In comparison to streptomycin, both oils showed slightly higher activity (against most Gram-positive bacteria) in the disc diffusion method and slightly lower activity when the microdilution method was employed. They also exhibited antifungal potential higher than that of the commercial fungicide bifonazole.

Keywords: *Cotinus coggygria*, essential oil composition, antibacterial activity, antifungal potential.

INTRODUCTION

Cotinus is a small genus of the family Anacardiaceae with two species: *Cotinus coggygria* Scop., Eurasian smoketree, and *Cotinus obovatus* Raf., American smoketree.[1] The flora of Serbia comprises two varieties of *C. coggygria*: var. *laevis* and var. *arenaria*. *C. coggygria* is a deciduous, polygamous shrub or little tree up to 7 m tall. It has a wide distribution from southern Europe, the Mediterranean, Moldova, and the Caucasus to central China and the Himalayas. It is frequent and locally common in some parts of Serbia, especially on limestone and sedimentary rocks and in the forests of black hornbeam and black pine.[2] The Serbian local names for this plant are "rujevina" and "ruj", which indicate the dark red colour of the leaves in autumn. In the folk medicine of various countries, the leaves are used as antiseptic, anti-inflammatory, antimicrobial, anti-haemorrhagic,

Serbian Chemical Society member.
* Corresponding author. E-mail: smilo@chem.bg.ac.yu
doi: 10.2298/JSC0711045N

wound-healing and against diarrhoea.[3] The leaves and the hardwood are used for the dyeing of leather, wool and silk into a yellowish colour.[2] Extracts of *C. coggygria* from the USA showed *in vitro* anti-oxidant activity.[4] The leaves and young branches are utilized for the production of essential oil with a terpenic odour for use in perfumery.[5] The antibacterial and antifungal activity of the essential oils of *C. coggygria* have hitherto not been significantly investigated. The essential oil of *C. coggygria* from Hungary inhibited the growth of bacteria (especially Gram-positive strains) and some fungi.[6]

Previous studies of the volatiles from *C. coggygria* included essential oils from Turkey, Bulgaria, Hungary and Greece.[3,5–7] In the oils from Turkey, the main constituents were limonene 48.5 %, (*Z*)-*β*-ocimene 27.9 % and (*E*)-*β*-ocimene 9.7 %.[3] In the oils from Bulgaria, the main components were *α*-pinene 44.0 %, limonene 20.0 %, *β*-pinene 11.4 %.[5] In the oils from Hungary, the main constituents were limonene 30.0–40.0 %, *α*-pinene 24.4–34.3 %, *β*-pinene 7.6–20.2 %, Δ^3-carene 4.6–11.0 % and *α*-terpinolene 3.3–10.6 %.[6] In the oils from Greece, the main components were different in different samples: in the first oil, the main constituents were limonene 67.4 %, *α*-pinene 14.7 % and terpinolene 8.6 %; in the second, myrcene 32.0 %, sabinene 18.0 % and *α*-pinene 15.9 %; in the third oil, main components were sabinene 24.2 %, myrcene 14.0 %, limonene 10.9 % and terpin-4-ol 10.9 %.[7]

In this work, the analyses of two essential oils, both obtained from the leaves with young twigs of wild-growing *C. coggygria* from two localities in Serbia, as well as the antifungal and antibacterial activity of the oils are reported.

EXPERIMENTAL

Plant material. The plant material was collected in June 2005 in Serbia at two localities: Deliblatska peščara (Deliblato Sand) and Zemun.

Isolation of the essential oils. The fresh leaves and twigs were cut up together into small pieces and subjected to hydrodistillation for 2 h using a Clevenger apparatus to obtain the essential oils, having a characteristic terpene-like smell, in yields of 0.23 % (w/w) for the essential oil from Deliblatska peščara and 0.20 % (w/w) for the essential oil from Zemun.

Analysis of the essential oils. The oils were analyzed by GC–FID and GC–MS. The GC analysis was carried out on a gas chromatograph HP 5890 Series II (Hewlett–Packard, USA) fitted with an FID (300 °C), split/splitless injector (250 °C) and an HP-5MS column (30 m×0.25 mm×0.25 μm film thickness). The temperature program was 50–285 °C at a rate of 4.3 °C min^{-1} and the carrier gas was helium (1 ml min^{-1}) measured at 210 °C.

Gas chromatographic–mass spectrometric analysis (GC–MS) was performed using an Agilent 6890 gas chromatograph (Agilent, USA) coupled with an Agilent 5973 Network mass selective detector (MSD) (Agilent, USA), operating in the positive ion electron impact (EI) mode. The separation was achieved using an Agilent 19091S-433 HP-5MS fused silica capillary column, 30 m×0.25 mm i.d., 0.25 μm film thickness. The GC oven temperature was programmed from 60 to 285 °C at a rate of 4.3 °C min^{-1}. Helium was used as the carrier gas, the inlet pressure was 25 kPa, the linear velocity was 1 ml min^{-1} at 210 °C. The injector temperature was 250 °C, and the injection mode splitless. MS scan conditions: source temperature, 200 °C; interface temperature, 250 °C; *E* energy, 70 eV; mass scan range, 40–350 amu (atomic mass units).

Identification of components. A library search and mass spectral deconvolution and extraction were performed using NIST AMDIS (Automated Mass Spectral Deconvolution and Identification

System) software version 2.4 using retention index (*RI*) calibration data analysis parameters with a "strong" level and 7 % penalty for compounds without a *RI*. The retention indices were experimentally determined using the standard method[6] involving retention times of *n*-alkanes, injected after the essential oil under the same chromatographic conditions. The search was performed using our own library, containing 4951 spectra.

Antibacterial activity. The tests were performed against the following bacteria: *Bacillus cereus* (isolated from food), *Bacillus subtilis* (ATCC 10707), *Escherichia coli* (ATCC 35218), *Micrococcus flavus* (ATCC 10240), *Micrococcus luteus* (ATCC 9341), *Proteus mirabilis* (isolated from food), *Salmonella typhimurium* (ATCC 13311), *Staphylococcus aureus* (ATCC 6538), *Staphylococcus epidermidis* (ATCC 12228) and *Staphylococcus faecalis* (ATCC 25922).

Disc diffusion test. Oils were investigated by disc diffusion using 4 mm filter discs. Bacterial species were cultured overnight at 28 °C in LB (Luria broth) medium. The bacterial suspension containing 10^5 cell/ml was added to the top agar and then dissolved in Petri dishes with solid Muller–Hinton medium. Filter discs with 5 µl of essential oil and another one with 5 µl of streptomycin solution (stock solution in DMSO, concentration of 1 mg ml^{-1}) per disc were placed on the agar plates. After 24 h of incubation at the appropriate temperature, the diameter of the growth inhibition zones was measured.[8] Streptomycin (Sigma P 7794, USA) was used as a positive control.

The minimum inhibitory and minimum bactericidal concentrations, *MIC* and *MBC*, respectively, were determined using 96-well microtitre plates. Series of different concentrations of the tested oils (within the range of 1.25–5.00 µl/ml) were prepared by dissolving in LB medium inoculated with bacterial suspension in saline solution, with a cell concentration of 10^5 cell/ml. The microplates were incubated for 24 h at 28 °C. The lowest concentrations without visible growth (under a binocular microscope) were defined as the concentrations that completely inhibited bacterial growth (*MIC*s). The minimum bactericidal concentrations (*MBC*s) were determined by serial subcultivation of 2 µl into microtitre plates containing 100 µl of broth per well and further incubation for 72 h. The lowest concentration that killed the bacteria was defined as the *MBC*, indicating 99.5 % killing of the original inoculums. The optical density of each well was measured at a wavelength of 655 nm by Microplate manager 4.0 (Bio-Rad Laboratories) and compared with the blank and positive control. Commercial antibiotic, streptomycin (stock solution in DMSO, concentration of 1 mg ml^{-1}) was used as the positive control.[9]

Antifungal activity. In order to investigate the antifungal activity of the essential oils of *C. coggygria*, a modified microdilution technique was used.[10] The fungal spores were washed from the surface of agar plates with sterile 0.85 % saline containing 0.1 % Tween 80 (v/v). The spore suspension was adjusted with sterile saline to a concentration of approximately 1.0×10^5 in a final volume of 100 µl. The tests were performed against the following fungal species: *Aspergillus niger* (ATCC 6275), *Aspergillus ochraceus* (ATCC 12066), *Aspergillus versicolor* (ATCC 11730), *Aspergillus flavus* (ATCC 9170), *Aspergillus fumigatus* (isolated from animals), *Penicillium ochrochloron* (ATCC 9112), *Penicillium funiculosum* (ATCC 10509), *Trichoderma viride* (IAM 5061), *Candida albicans* (clinical isolate) and *Trichophyton mentagrophytes* (clinical isolate). The commercial fungicide bifonazole (Srbolek, Serbia) concentration of 1 % (w/v) was used as the positive control.

The minimum inhibitory concentrations (*MIC*s) determination was performed by the dilution technique using 96-well microtitre plates. The tested essential oils were dissolved in broth MA (Malt agar) medium; the final concentration range was 1.25–20.00 µl/ml. The microplates were incubated for 72 h at 28 °C. The lowest concentration without visible growth (under a binocular microscope) was defined as the concentration which completely inhibited fungal growth (*MIC*), while those that killed the fungi were the minimal fungicidal concentrations (*MFC*). The optical density of each well was measured at a wavelength of 655 nm by Microplate manager 4.0 (Bio-Rad Laboratories, USA) and compared with the blank and the positive control.

RESULTS AND DISCUSSION

The yields of the oils of both samples of *C. coggygria*, calculated per weight of fresh plant material (leaves and branches), were 0.23 % (w/w) for oil from Deliblatska peščara and 0.20 % (w/w) for oil from Zemun. 21 and 22 Components were identified in each of the oils from Deliblatska Peščara and Zemun, respectively. Both oils showed very similar chemical composition with monoterpenic hydrocarbons dominating (87.4 and 93.1 %, respectively) The major components, *i.e.*, limonene (47.0 and 39.2 %), (*Z*)-*β*-ocimene (16.4 and 26.3 %), *α*-pinene (8.2 and 8.4 %), (*E*)-*β*-ocimene (4.6 and 9.0 %) and terpinolene (6.8 and 5.3 %) were the same in both oils (Table I). Limonene was also the main constituent of the essential oils of *C. coggygria* from Turkey,[3] Hungary[6] and Greece (Mt Pilio).[7] The essential oil from Bulgaria contained *α*-pinene (44 %) as the main component and a high percentage of limonene (20 %).[5] High percentage of (*Z*)- and (*E*)-*β*-ocimenes (21 and 35.3 %), present in a similar ratio (*Z*:*E ca*. 3:1) to that observed in the oil of Turkish origin,[3] is another characteristic of these oils.

TABLE I. Composition of the studied *C. coggygria* essential oils

Components	*RRI*[a]	Deliblatska peščara[b]	Zemun[c]
(*Z*)-3-Hexenal	800	0.4	–
(*E*)-2-Hexenal	854	7.6	1.2
Tricyclene	926	t	–
α-Pinene	939	8.2	8.8
α-Fenchene	951	t	–
Camphene	953	–	1.0
β-Pinene	980	2.1	2.1
β-Myrcene	991	1.5	1.4
α-Phellandrene	1005	0.4	–
(*Z*)-Hex-3-en-1-ol acetate	1007	t	–
Δ^3-Carene	1011	–	t
Limonene	1031	47.0	39.2
(*Z*)-*β*-Ocimene	1040	16.4	26.3
(*E*)-*β*-Ocimene	1050	4.6	9.0
γ-Terpinene	1062	t	t
Terpinolene	1088	6.8	5.3
p-Cymenene	1089	t	–
Linalool	1098	t	–
Alloocimene	1129	0.4	1.4
α-Terpineol	1189	t	t
Bornyl acetate	1285	–	t
β-Caryophyllene	1418	1.1	2.5
α-Humulene	1454	–	t

TABLE I. Continued

Components	*RRI*	Deliblatska peščara	Zemun
γ-Muurolene	1477	0.8	t
Germacrene D	1480	–	0.5
Bicyclogermacrene	1494	–	–
γ-Cadinene	1513	–	t
δ-Cadinene	1524	0.4	0.7
Caryophyllene oxide	1581	–	t
α-Cadinol	1653	–	t
Total		97.3	99.4

[a]*RRI*, relative retention indices calculated against C_x–C_y *n*-alkanes under the same GC conditions; [b]oil yield 0.23 % (w/w); [c]oil yield 0.20 % (w/w); t – concentration less than 0.4 %

The antibacterial activity obtained by the disc diffusion method is presented in Table II. The essential oil from Deliblatska peščara showed inhibition zones from 6–23 mm. The highest zones were obtained against the *Staphylococcus* and *Micrococcus* species, while the lowest activity was against *Proteus mirabilis*. Inhibition zones of 6–28 mm were obtained for the oil from Zemun, with slightly higher activity against *Staphylococcus* species than of the oil from Deliblatska peščara. Both oils exhibited the same actitivity against *Micrococcus* species, while *Staphylococcus* and *Micrococcus* species showed higher sensitivity than other bacteria species. According to these tests, both oils showed higher antibacterial activity than streptomycin used as the positive control, except in the case of *P. mirabilis*.

TABLE II. Diameters of the inhibition zones (mm) in the disc diffusion method of determining the antibacterial activity of the studied *C. coggygria* essential oils (5 µl/disc)

Bacteria	Deliblatska peščara	Zemun	Streptomycin[a]
Bacillus cereus	15	18	10
Bacillus subtilis	15	17	10
Escherichia coli	9	10	10
Micrococcus flavus	22	23	22
Micrococcus luteus	20	20	20
Proteus mirabilis	6	6	8
Salmonella typhimurium	9	11	12
Staphylococcus aureus	23	28	15
Staphylococcus epidermidis	19	25	12
Staphylococcus faecalis	23	27	14

[a]Positive control, streptomycin, concentration 1 mg ml^{-1} (in DMSO)

The results of antibacterial activity (*MIC* and *MBC*) are presented in Table III. The oil from Deliblatska peščara showed lower antibacterial activity in this test with bacteriostatic activity in the concentration range 2.5–5.0 µl/ml, while bactericidal concentrations were in the range of 2.5–10.0 µl/ml. The essential oil from

Zemun showed activity with *MIC* and *MBC* values ranging from 1.25–5.0 µl/ml. *P. mirabilis* showed a higher resistance than other bacteria in this test, while *Salmonella typhymurium*, the *Bacillus* species and *Escherichia coli* showed higher sensitivity to the tested oils. The commercial antibiotic, streptomycin, showed slightly better antibacterial activity than the two essential oils.

TABLE III. Antimicrobial activity expressed as minimum inhibitory (*MIC*) and minimum bactericidal concentrations (*MBC*), in µl/ml, of the studied *C. coggygria* essential oils, determined by the microdilution method

Bacteria	Deliblatska peščara		Zemun		Streptomycin[a]	
	MIC	*MBC*	*MIC*	*MBC*	*MIC*[b]	*MBC*[b]
Bacillus cereus	2.5	2.5	1.25	1.25	0.25	0.5
Bacillus subtilis	2.5	2.5	1.25	1.25	0.25	0.5
Escherichia coli	5.0	5.0	1.25	1.25	0.5	1.0
Micrococcus flavus	2.5	2.5	2.5	2.5	1.0	2.0
Micrococcus luteus	2.5	2.5	2.5	2.5	1.0	2.0
Proteus mirabilis	5.0	10.0	2.5	5.0	1.0	1.0
Salmonella typhimurium	2.5	2.5	1.25	1.25	0.25	0.5
Staphylococcus aureus	2.5	2.5	1.25	2.5	1.0	2.0
Staphylococcus epidermidis	2.5	2.5	2.5	2.5	1.0	2.0
Staphylococcus faecalis	2.5	2.5	1.25	2.5	1.0	2.0

[a]Positive control, streptomycin concentration 1 mg ml^{-1} (in DMSO); [b]in µg ml^{-1}

The antifungal activity of the essential oils is presented in Table IV. It can be noticed that the oil from Deliblatska peščara showed antifungal activity with *MIC* values of 5.0–40.0 µl/ml and *MFC* values of 10.0–40.0 µl/ml. The antifungal activity of the oil from Zemun was even better with *MIC* values between 1.25–10.0 µl/ml and *MFC* values of 2.5–20.0 µl/ml. *Trichoderma viride* showed higher resistance to both oils, while *Candida albicans* and *Trichophyton mentagrophytes* were more sensitive than the other fungi. The commercial fungicide, bifonazole, used as the positive control showed activity with higher *MIC* and *MFC* values than the essential oils.

TABLE IV. Minimum inhibitory (*MIC*) and minimum fungicidal concentrations (*MFC*), in µl/ml, of the studied *C. coggygria* essential oils, determined by the microdilution method

Micromycetes	Deliblatska peščara		Zemun		Bifonazole[a]	
	MIC	*MFC*	*MIC*	*MFC*	*MIC*	*MFC*
Aspergillus niger	10.0	10.0	2.5	5.0	20.0	20.0
Aspergillus ochraceus	10.0	10.0	2.5	5.0	20.0	20.0
Aspergillus versicolor	5.0	10.0	2.5	5.0	20.0	20.0
Aspergillus flavus	10.0	20.0	5.0	10.0	20.0	20.0
Aspergillus fumigatus	10.0	20.0	5.0	10.0	40.0	40.0
Penicillium ochrochloron	20.0	20.0	5.0	10.0	40.0	80.0
Penicillium funiculosum	20.0	20.0	5.0	10.0	40.0	80.0

TABLE IV. Continued

Micromycetes	Deliblatska peščara		Zemun		Bifonazole	
	MIC	*MFC*	*MIC*	*MFC*	*MIC*	*MFC*
Trichoderma viride	40.0	40.0	10.0	20.0	80.0	80.0
Candida albicans	5.0	10.0	1.25	2.5	20.0	20.0
Trichophyton mentagrophytes	5.0	10.0	1.25	2.5	20.0	20.0

[a]Positive control, commercial preparation containing 1 % (w/v) of bifonazole in ethanol.

Acknowledgement: The authors are grateful to the Ministry of Science of Serbia (Project 142053) for financial support.

И З В О Д

ХЕМИЈСКИ САСТАВ, АНТИБАКТЕРИЈСКА И АНТИФУНГАЛНА АКТИВНОСТ ЕТАРСКИХ УЉА БИЉНЕ ВРСТЕ *Cotinus coggygria* ИЗ СРБИЈЕ

МИРОСЛАВ НОВАКОВИЋ[1], ИВАН ВУЧКОВИЋ[1], ПЕЂА ЈАНАЋКОВИЋ[2], МАРИНА СОКОВИЋ[3], АНКА ФИЛИПОВИЋ[4], ВЕЛЕ ТЕШЕВИЋ[5] и СЛОБОДАН МИЛОСАВЉЕВИЋ[5]

[1]Институт за хемију, технологију и металургију, Његошева 12, 11000 Београд, [2]Биолошки факултет, Студентски трг 16, 11001 Београд, [3]Институт за биолошка истраживања "Синиша Станковић", Булевар Деспота Стефана 142, 11000 Београд, [4]Градски Завод за заштиту здравља, Булевар Деспота Стефана 54а, 11000 Београд и [5]Хемијски факултет, Студентски трг 16, 11001 Београд

Применом GC–MS методе идентификована је укупно 31 компонента у оба етарска уља изолована дестилацијом воденом паром из лишћа и младих гранчица биљне врсте *Cotinus coggygria* Scop. са два локалитета у Србији (Делиблатска пешчара и Земун). Такође је испитана антибактеријска и антифунгална активност оба узорка. У оба уља најзаступљенији су били монотерпенски угљоводоници (87,4 и 93,1 %), међу којима је доминантна компонента лимонен (47,0 и 39,2 %). Антибактеријска активност је одређена дифузионом и микродилуционом методом, а антифунгална активност модификованом микродилуционом методом. Према дуфузионој методи, оба уља су показала нешто боље антибактеријско дејство (првенствено на грам-позитивне бактерије) него стрептомицин, док је на основу микродилуционе методе њихова активност била нешто слабија. У поређењу са бифоназолом, оба тестирана уља су показала нешто боље антифунгално дејство.

(Примљено 19. децембра 2006, ревидирано 6. јула 2007)

REFERENCES

1. http://en.Wikipedia.org./wiki/Cotinus (May 10, 2006)
2. M. Gajić, in *Flora of Serbia V*, M. Josifović, Ed., SANU, Belgrade 1973, p. 57
3. B. Demirci, F. Demirci, K. H. C. Baser, *Flavour Fragr. J.* **18** (2003) 43
4. H. E. Westenburg, K. J. Lee, S. K. Lee, *J. Nat. Prod.* **63** (2000) 1696
5. E. T. Tsankova, A. S. Dyulgerov, B. K. Milenkov, *J. Essent. Oil Res.* **5** (1993) 205
6. I. Hethelyi, J. Domokos, E. Lemberkovics, G. Verzar–Petri, *Herba Hung.* **25** (1986) 135
7. O. Tzakou, I. Bazos, A. Yannitsaros, *Flavour Fragr. J.* **20** (2005) 531.
8. H. Van Den Dool, P. D. Kratz, *J. Chromatogr.* **11** (1963) 4637
9. R. Verpoorte, T. A. Van Beek, P. H. A. M. Thomassen, J. Andeweil, A. Baerhim Svendsen, *Ethnopharmacol.* **8** (1983) 2878
10. H. Hanel, W. Raether, *Mycoses* **31** (1988) 148
11. K. D. Daouk, M. S. Dagher, J. E. Sattout, *J. Food Prot.* **58** (1995) 1147.

Journal of the Serbian Chemical Society
JSCS@tmf.bg.ac.yu • www.shd.org.yu/JSCS

J. Serb. Chem. Soc. 72 (11) 1053–1062 (2007) UDC 546.56'47+547.979.7:535.371:581.171
JSCS–3639 *Original scientific paper*

Different possibilities for the formation of complexes of copper and zinc with chlorophyll inside photosynthetic organelles: chloroplasts and thylakoids

JELENA ZVEZDANOVIĆ, DEJAN MARKOVIĆ* and GORAN NIKOLIĆ

Faculty of Technology, 16000 Leskovac, Serbia

(Received 8 September 2006, revised 21 March 2007)

Abstract: The possibility of the formation of copper and zinc complexes with chlorophyll in photosynthetic organelles (chloroplasts) and suborganelles (thylakoids) was studied. The visible and fluorescence spectra obtained from chloroplasts and thylakoids in the presence of the two metals confirmed complex formation in the case of copper, while such possibility appears to be very minor in the case of zinc. The reason for this distinction lies in the different type of complexes which chlorophyll forms with the two metals: only "central" or "substitution" copper–chlorophyll complexes may be formed inside the two isolated entities, while the formation of a possible zinc–chlorophyll "peripheral" type of complex is prevented for steric reasons. The latter fact is of high biological relevance, since both complexes may cause an irreversible impairment and damage of photosynthetic function.

Keywords: chlorophyll, copper, zinc, fluorescence, chloroplasts, thylakoids.

INTRODUCTION

Chlorophyll (Chl), the major photosynthesis pigment, in chemical terms is a chlorin, a dihydroporphyrin derivative containing an isocyclic cyclopentanone ring (fused to a pyrrole ring between C-13 and C-15 positions), where central metal Mg atom coordinates four symmetric pyrrole rings (Fig. 1). The major function of chlorophyll in photosynthesis is related to light collection and light conversion processes. Significant progress has been made in understanding of the *in vitro* properties of Chl and this contributed to a better understanding of the role of Chl in photosynthesis on the molecular level.[1,2]

Plants easily absorb many toxic heavy metals.[3,4] Once absorbed, they penetrate to plant tissues (including leaves) and at higher concentrations, they may inhibit photosynthesis.[5–7] Heavy metals can replace the relatively weakly bound central magnesium atom (Mg) of chlorophyll, to form heavy metal complexes (Chl––HMS).[8–10] The Chl–HMS complexes may cause an impairment of photosynthetic function, which can have fatal consequences.[11] The detailed consequences of this substitution for higher plants and green algae have been discussed by Küpper *et al*.[8,12,13]

* Corresponding author: E-mail: markovic57@info-net.co.yu
doi: 10.2298/JSC0711053Z

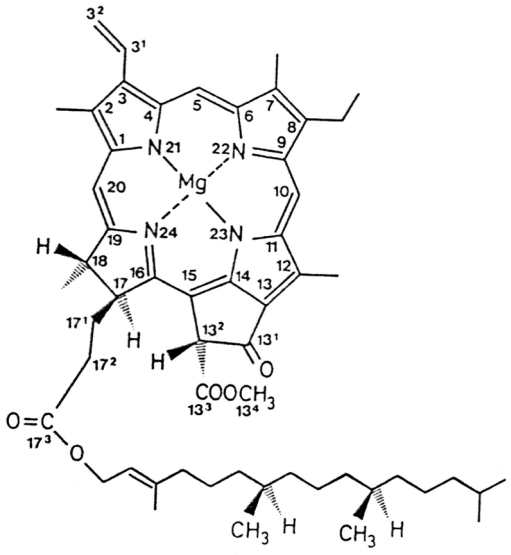

Fig. 1. Structure of chlorophyll *a*, with numerated C-positions.

The general reactions of Chl with heavy metals *in vitro*[11] and *in vivo*[14,15] have already been reported. Early *in vivo* studies of Chl–HMS formation in higher plants and green algae[8,12] showed that this reaction was strongly dependent on the light intensity: in the dark, the majority of antenna Chls are accessible for Chl–HMS formation[13] ("shade reaction"), while under high light conditions, only a small fraction of antenna Chls undergoes it ("sun reaction").[8,11,12] Chl–HMS complexes can be prepared by heating Chls with metal salts in acid or organic solutions.[16] Also, acidification of Chl solutions with hydrochloric acid followed by the addition of a heavy metals solution leads to the formation of Chl–HMS.[7,8,16–18] Küpper performed experiments *in vitro* by adding solutions of heavy metals to 96 % ethanolic grass extracts.[8]

Chl–HMS shows a spectroscopic behavior different to that of Chl itself,[8,17–21] qualitatively (shift of the characteristic band maxima), as well as quantitatively (different intensities of the corresponding bands). For example, Cu–Chl formation is followed by a hypsochromic ("blue") shift of the long wavelength ("red") absorption band,[8,12,17,18] with significantly lower coefficient of absorption value compared to Chl itself.[17] A not so expressed "blue" shift of the "red" Chl band was observed for Zn–Chl.[19,22]

In this work, the possible formation of Chl–HMS complexes in isolated photosynthetic organelles, chloroplasts and their sub-units, thylakoids, with two chosen heavy metals, zinc and copper, was studied. In lower concentrations, copper is an essential micronutrient for higher plants and algae and it is even a constituent of the primary electron-donor of photosystem I, the Cu–protein, plastocyanin.[23] However, high external Cu concentrations (and those of Zn as well) – like the ones in this work – may produce many damaging effects. Zinc may be inclu-

ded in the degradation of chloroplasts stromal proteins.[24] Copper may affect all kinds of photosynthetic activities, such as electron-transport and ATP production,[25–28] or oxygen evolution.[29]

The complexes Cu–Chl and Zn–Chl were examined in this study by visible and fluorescence spectroscopy.

EXPERIMENTAL

The Chl–HMS formation may occur under low light ("shade reaction") and under high light conditions ("sun reaction").[13] Since just a minority of antenna chlorophylls (*in vivo*) is accessible to Chl–HMS formation under high light conditions,[13] the experimental part of this work was performed under shade conditions as much as possible.

Isolation of intact chloroplasts

Intact chloroplasts from spinach were prepared using a described procedure.[30] Healthy, intact spinach leaves floating in a basin of water were exposed to bright light for 30 min, before removing the midribs. The plant material (50 g) was immersed in 200 cm^3 of grinding medium, which had previously been brought to a consistency of melting snow. The grinding was done in a couple of seconds. The suspension was then squeezed through two layers of muslin and filtered through 8 layers of muslin and a layer of cotton-wool. The chloroplasts were quickly separated from the supernatant by centrifugation in four tubes at 4000 rpm for 100 s. The supernatant was decanted and the pellet, resuspended in about 80 cm^3 of grinding medium, was recentrifuged in two tubes at 4000 rpm for 100 s.

A low cation medium was employed as the grinding and resuspending medium.[31,32] It contained 12.035 g of sorbitol, 2 cm^3 of 1 M KCl, 0.8 cm^3 of 0.25 M EDTA, 95 cm^3 of water and 2.383 g of Hepes (4-(2-hydroxyethyl)-1-piperazine ethanesulphonic acid) buffer, pH 7.8. The grinding medium was prepared daily by mixing about 6 cm^3 of the low cation medium with 18 g sorbitol and 276 cm^3 of water.

The clean, final pellet of chloroplasts was resuspended in 0.5–1.0 cm^3 of resuspending medium, containing 5 cm^3 of the low-cation medium, 0.02 cm^3 of 1 M $MgCl_2$, 0.02 cm^3 of 1 M $MnCl_2$, 0.1 g of serum albumin and 5 cm^3 of water.

The chlorophyll content (Chl*a* – Chl*b*) in the suspension of chloroplasts was calculated as reported (2.2×10^{-3} M).[33]

Content of intact chloroplasts in the suspension of chloroplasts

The content was calculated by comparing the reduction of $K_3Fe(CN)_6$ in a suspension of intact chloroplasts and broken chloroplasts (spectrophotometrically). The mixture contained 10×10^{-3} cm^3 of chloroplasts suspension, 1 cm^3 of the low-cation medium, 1 cm^3 of water, 20×10^{-3} cm^3 of 1 M $MgCl_2$, and 40×10^{-3} cm^3 of a solution containing 164 mg of $K_3Fe(CN)_6$ dissolved in 1 cm^3 of water. The absorbance of the mixture was measured at 420 nm (following a 1 min exposure to bright light) and then upon the subsequent addition of 10×10^{-3} cm^3 of 1 M NH_4Cl. The same procedure was also applied to broken chloroplasts (the chloroplasts were broken by hard mixing in an excess of water). Calculated content of intact chloroplasts was 65 %.

Incubation of chloroplasts and thylakoids with zinc and copper

The reaction mixture containing 1.5 cm^3 of the low-cation medium, 20×10^{-3} cm^3 of chloroplasts or thylakoids suspension, 1.25 cm^3 of water and 0.25 cm^3 of 0.05 M aqueous solution of $ZnSO_4$ or $CuSO_4$ was prepared. After the incubation period (t_{inc} = 3 h – 7 d), the copper or zinc complexes with chlorophyll from the incubated chloroplasts or thylakoids were extracted by adding acetone (4 cm^3), and then cyclohexane (5 cm^3) in 2 cm^3 of the reaction mixture. The acetone releases the chlorophyll from the incubated chloroplasts and thylakoids (making them "disorganized") and increases their solubility in the cyclohexane phase, in which the complex formation is stopped.[8]

Finally, the Vis spectra of the complexes were recorded in cyclohexane using the Vis spectrophotometric method for *in vitro* conditions.[22]

Vis spectroscopy

The Vis spectra of "disorganized" Cu–Chl and Zn–Chl complexes (obtained from the incubated chloroplasts and thylakoids) were recorded on a Varian Cary-100 spectrophotometer in the wavelength range of 350 to 750 nm with a constant concentration of ions (Cu^{2+} or Zn^{2+}), after different t_{inc} periods.

Fluorescence spectroscopy

The fluorescence spectra of the chloroplasts and thylakoids in the resuspension medium were recorded on a Fluorolog Jobin Yvon Horiba spectrofluorimeter. The excitation wavelength was 430 nm.

RESULTS

Before the addition of any metal ions to the chloroplasts and thylakoids, a control experiment was performed in order to assign all possible absorption changes in the absorption of Chl to factors other than the formation of the complexes. The control was performed over a period of one week. A hardly detectable change occurred just at the end of this period (not shown). This means that changes in the Vis spectra of "disorganized chlorophylls" and the fluorescent spectra of treated chloroplasts and thylakoids occurring in a period of less than one week, shown in Figs. 2–4 could be assigned only to the formation of the complexes.

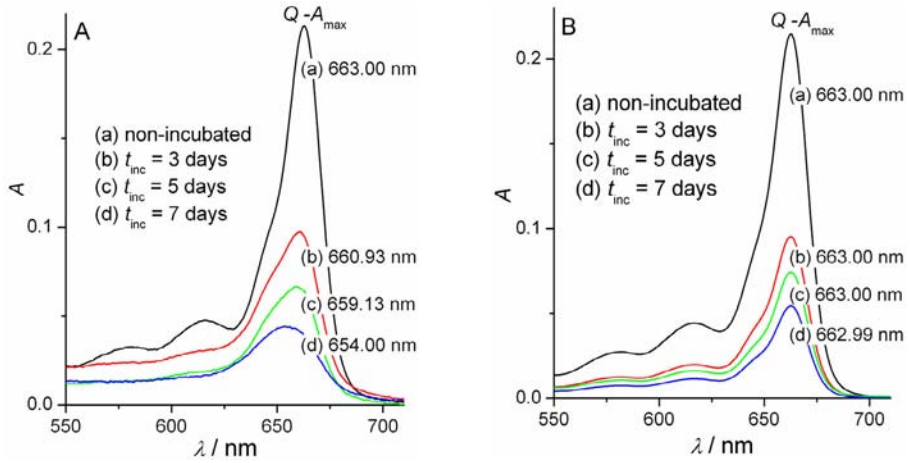

Fig. 2. Vis spectra of "disorganized chlorophylls" obtained from isolated intact chloroplasts (65 %) incubated for two time periods ($t_{inc.}$) with (A) copper and (B) zinc. The Chl concentration in the chloroplasts was Chl_{a+b} = 0.015 mmol dm^{-3}, while the two concentrations ratio was $n(Cu^{2+},Zn^{2+})/n(Chl_{a+b})$ = 3000:1.

The Vis spectra of "disorganized chlorophylls" obtained from chloroplasts incubated with zinc and copper ions for several different periods of time are shown in Figs. 2A and 2B, respectively. The spectra of "disorganized chlorophylls" obtained from non-incubated chloroplasts serve as blanks. The *Q* or "red band" is an exclusive ("diagnostic") characteristic of chlorophyll and its derivatives,[2,34,35]

thus eventual changes in its intensity or position should be attributed only to Chl and not to any other pigment (such as for Soret or the *B* ("blue")-band, where accessory pigments, carotenoids, can make a significant contribution).

Fluorescence spectra obtained from isolated photosynthetic organelles, chloroplasts, and sub-organelles, thylakoids, incubated with copper ions for two different periods of time, are shown in Figs. 3a and 3b, respectively. The fluorescence of non-incubated chloroplasts again plays the role of the "blank". While the position of the fluorescence maximum (F_{max}) barely shows any change during the incubation, the intensity of the F_{max} shows a huge drop (> 75 %).

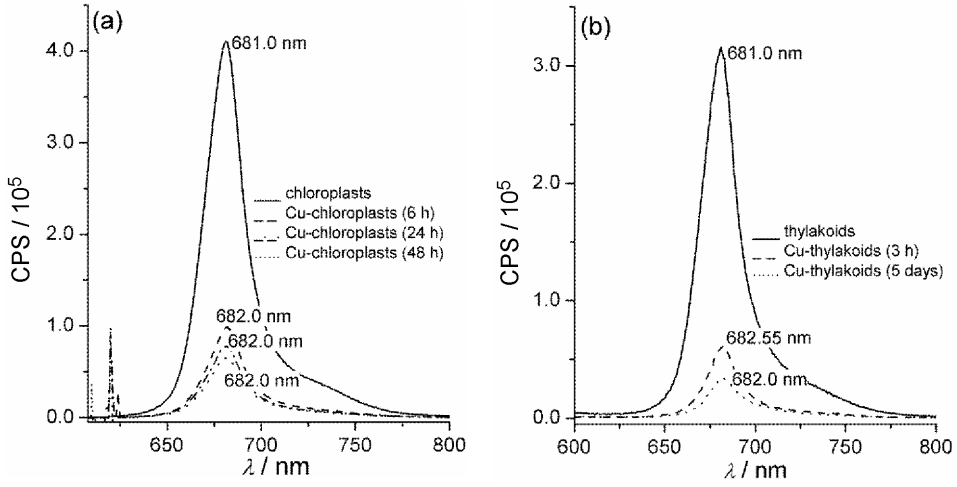

Fig. 3. The chlorophyll *Q*-band fluorescence spectra of (a) chloroplasts, and (b) thylakoids in the resuspended medium in the presence of copper for two different time periods following the beginning of the formation of the complexes (t_{inc}). Clearly, a very similar type of change can be seen. The fluorescence (cps – counts per second) from non-incubated chloroplasts served as the blank.

The completely opposite behavior was observed with the chloroplasts and thylakoids incubated with Zn^{2+} ions (Figs. 4a and 4b, respectively), *i.e.*, the intensity of F_{max} of the chloroplasts did not change significantly even after 2 days of incubation (Fig. 4a), or even a certain rise was evidenced after 5 days of incubation of the thylakoids (Fig. 4b).

DISCUSSION

Vis spectra

The Vis spectra of isolated chloroplasts incubated with copper, and then converted into disorganized chlorophylls, clearly proved the formation of the Cu complex. The hypsochromic ("blue") shift of 9 nm after 7 days of incubation (followed by a hypochromic effect, fall of the intensity) is clearly visible (Fig. 2A). The same effect was detected with the isolated thylakoids (shown in the Appendix). The results shown in Fig. 2A were obtained with an about 10 times higher con-

centration of Cu^{2+} ions, compared to that used for recording the fluorescent spectra; an additional experiment performed with a comparable Cu^{2+} concentration also expressed a "blue" shift (a concentration effect, in addition to the hypsochromic effect, shown in Appendix), although two times smaller than the one shown in Fig. 2A. On the other hand, isolated chloroplasts incubated with zinc, and then also converted in disorganized chlorophylls, did not prove the formation of a Zn complex (Fig. 2B), at least not one of the same type as the one formed with Cu, since a hypsochromic shift was hardly visible. This is in good agreement with the results found in a study of isolated Chl fractions,[22] where a clear and significant hypsochromic effect (also followed by a hypochromic effect, proving the instability of complexes) was found for the Chl fractions incubated with copper, confirming "central" complex formation (in which the central Mg atom of chlorophyll was replaced by copper); at the same time, the "peripheral" complex (6-membered chelate cycle fused at the periphery of the Chl structure) was not clearly confirmed in the case of Cu–Chl, but was in the case of Zn–Chl.[22]

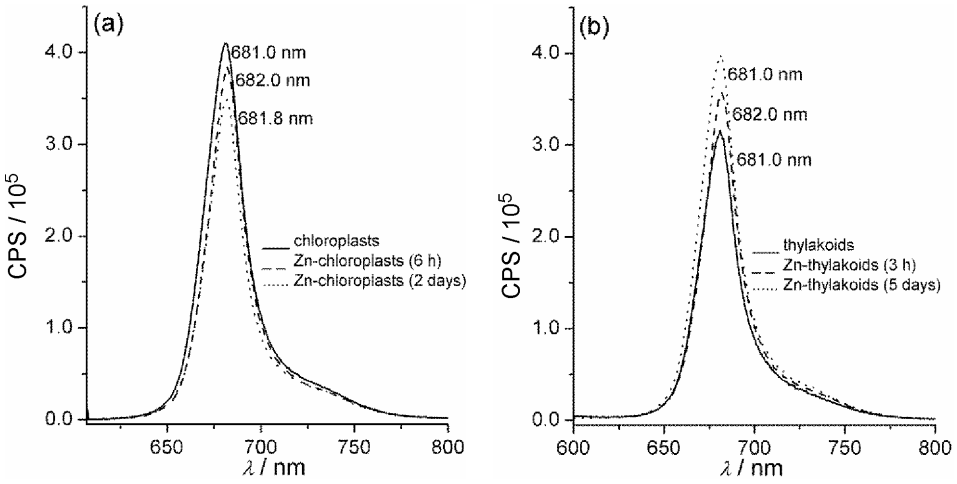

Fig. 4. The chlorophyll *Q*-band fluorescence spectra of (a) chloroplasts, and (b) thylakoids in the resuspended medium in the presence of zinc for two different time periods following the beginning of the formation of the complexes (t_{inc}). Clearly, while a very similar type of change can be seen (a–b), the behavior is quite the opposite compared to that shown in Figs. 3a and 3b (copper effect). The fluorescence (cps – counts per second) from non-incubated chloroplasts served as the blank.

Fluorescence spectra

Bearing in mind that Chl fluorescence represents an intrinsic probe of photosynthesis,[36] it was reasonable to expect another proof for Chl–HMS formation from fluorescence spectra (*in vitro*). Generally, it is well known that Chl–HMS formation leads to a decrease of the intensity of the fluorescence emission, indicating the formation of an unstable first excitation state, which relaxes to a greater extent thermally.[13] Considering that chlorophyll fluorescence emission and ki-

netics *in vivo* are influenced by toxic heavy metals, including copper and zinc,[12,37] and bearing in mind the high complexity of the involved isolated photosynthetic organelles and sub-organelles, it is to be expected that the fluorescent spectra of chloroplasts and thylakoids would also be affected by the action of toxic metals. This is clearly seen with copper through a rough observation of the magnitude of the change in ΔF_{max} obtained with chloroplasts and thylakoids, compared to non-incubated chloroplasts and thylakoids (Figs. 3a and 3b) (F_{max} of Chl fluorescence in chloroplasts and thylakoids was red-shifted, to 681 nm, compared to isolated Chls due to the aggregation of the Chl molecules in the antennas).[2] The fluorescence emission was greatly suppressed in Cu-treated chloroplasts and thylakoids: the organization of the antennas of the photosystems favors the formation of non-fluorescent "central complexes", even after 3 h (thylakoids – Fig. 3b) or 6 h (chloroplasts – Fig. 3a). Prolongation of the incubation period (t_{inc}) up to 2 days (chloroplasts – Fig. 3a) or to 5 days (thylakoids – Fig. 3b) did not change the situation very much, even the almost negligible "red shift" of F_{max} (681 nm for non-incubated chloroplasts and thylakoids *vs.* 682 nm for the complex) remains the same. This remarkable decrease of fluorescence intensity (>75 %) induced by the action of copper is in accordance with copper-induced suppression of fluorescence induction in spinach chloroplasts,[6] or the induction kinetics in isolated thylakoids.[38] It is also necessary to note that the great similarity of the fluorescence spectra obtained from the chloroplasts and thylakoids (Figs. 3a and 3b) proves a predominance of the Cu–Chl interaction inside the photosynthetic antennas compared to the potential Cu interactions with the stromal lipo-protein matrix of the chloroplasts.

On the other hand, the fluorescence spectra of the chloroplasts and thylakoids exposed to the action of Zn^{2+} exhibited the completely opposite behavior (Figs. 4a and 4b). The magnitude of F_{max} decreased just a little after 6 h, and another few percents after 48 h, compared to the non-incubated chloroplasts (Fig. 4a). On the other hand the magnitude of the change in F_{max} for the thylakoids was of a higher magnitude but in the opposite direction (more than 20 % after 5 days, Fig. 4b). There is no clear explanation for this distinction, although Zn–Chl complexes have been reported to fluoresce at least as much as Chl itself in benzene and diethyl ether.[39] However, Zn–Chl can not replace Chl in higher plants and green algae – comparable systems to chloroplasts and thylakoids – because its "blue-shifted" absorbance detected in solutions[39] could reduce the spectral overlap of fluorescence/absorbance bands required for excitation transfer to the reaction centers of the photosynthetic apparatus of plants.[13] Therefore, in both cases – chloroplasts and thylakoids – there is not an extremely large drop in the Chl fluorescence intensity, as is the case with copper (Figs. 3a and 3b). A possible explanation could come from a nature of aggregated antennas structures. Chl molecules inside photosynthetic antennas are aggregated most probably through (C-131) =

= O···Mg interaction and this could potentially be the key factor preventing the formation of Zn–Chl "peripheral" complexes,[22] rather than a possible interaction with the stromal lipo-protein matrix (otherwise copper would react in a similar manner); the formation of "central" complexes in the case of zinc is certainly excluded.

Finally, the question is how much this *in vitro* behavior of the Chl–HMS complexes can mimic the expected *in vivo* situation, where plants and algae absorb copper and zinc from the surrounding environment, permitting the penetration within photosynthetic apparatus and the formation of Zn– and Cu–Chl complexes within it. One of the main limiting factors is the sensitivity of chlorophyll: Chl can undergo "light" and "dark" reactions. The first ones are mostly photo-oxidation reactions involving the chlorin structures, resulting in different porphyrin modifications.[40] The other ones involve the periphery of the chlorin structure but do not change the chlorin nucleus.[16] While the first ones can be prevented by simply keeping chlorophyll in the dark, the second ones can not be avoided and potentially, they can influence chelate formation.[22] The peripheral chelate formation is especially sensitive to oxidation reaction at the C-13[2] position (the allomerization reaction – see Fig. 1) yielding several derivatives incapable of enolization at the isocyclic ring.[16] Structures of the allomer products may exclude any possibility for the chelate formation ("peripheral complexes"). Generally, allomerization products are less abundant in fresh spinach samples than in the older ones; in the latter case, prolonged senescence may lead to chlorophyll breakdown and the appearance of monopyrrolic compounds.[41]

However, from a biological point of view, the formation of either type of complex, "central" or "peripheral", has pathological consequences on the functioning of chloroplasts and thylakoids, ranging from irreversible impairment (in the "light phase") to complete breakdown of photosynthesis, a fatal end for the plants.[8,11] The two complexes are selectively connected to particular steps in this pathological process. Thus while "central" complexes are generally related to primary photosynthesis photochemistry,[13] "peripheral" complexes certainly affect the process of photon transfer inside the photosynthesis antennas, by widening the gap in the spectral overlapping between neighboring Chl molecules.[12]

CONCLUSIONS

Of the studied metals, only copper forms complexes with Chl inside the photosynthetic antennas of isolated chloroplasts and thylakoids. The complexes are of "central" or "substitution" type. Zinc cannot form this type of complex and the other, "peripheral" type of Zn–Chl complex is not possible in chloroplasts and thylakoids for steric reasons.

APPENDIX

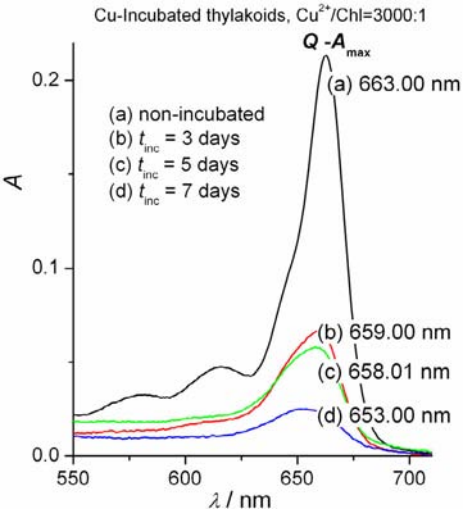

Incubation of isolated thylakoids by Cu^{2+} ions: the effect on A_{max} position of disorganized chlorophylls' *Q* ("red") band. The Cu^{2+}/Chl ratio the same as for Fig. 2A (3000:1).

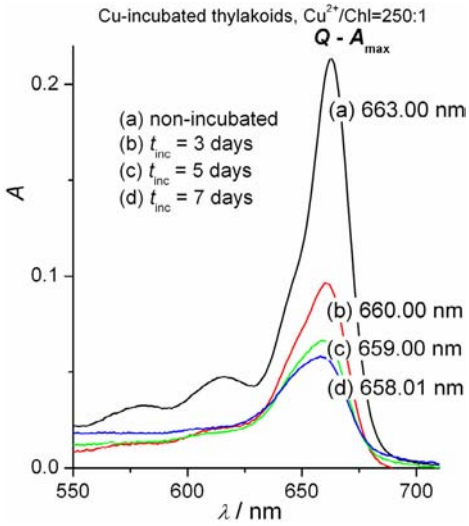

Incubation of isolated thylakoids by Cu^{2+} ions: the effect on A_{max} position of disorganized chlorophylls' *Q* ("red") band. The Cu^{2+}/Chl ratio is an order of magnitude smaller (250:1) than the one for Fig. 2A.

И З В О Д

РАЗЛИЧИТЕ МОГУЋНОСТИ ЗА ФОРМИРАЊЕ КОМПЛЕКСА БАКРА И ЦИНКА СА ХЛОРОФИЛОМ У ФОТОСИНТЕТИЧНИМ ОРГАНЕЛАМА: ХЛОРОПЛАСТИМА И ТИЛАКОИДИМА

ЈЕЛЕНА ЗВЕЗДАНОВИЋ, ДЕЈАН МАРКОВИЋ и ГОРАН НИКОЛИЋ

Технолошки факултет, 16000 Лесковац

У овом раду су испитиване могућности за формирање комплекса бакра и цинка са хлорофилом у фотосинтетичним органелама (хлоропластима) и суб-органелама (тилакоидима). Флуоресцентни спектри добијени из хлоропласта и тилакоида у присуству два метала потврдили су формирање комплекса у случају бакра, док је у случају цинка та могућност минорна. Разлог за овакву различитост је у различитим типовима комплекса које хлорофил формира са ова два метала: само "централни" или "супституциони" бакар–хлорофилни комплекси могу бити формирани унутар два изолована ентитета, док је формирање цинк–хлорофилног "периферног" типа комплекса спречено из стерних разлога. Последња чињеница је од велике биолошке важности пошто оба типа комплекса могу проузроковати неповратну дисфункцију и оштећење фотосинтетичког процеса.

(Примљено 8. септембра 2006, ревидирано 21. марта 2007)

REFERENCES

1. H. Scheer, in *Chlorophylls*, H. Scheer, Ed., CRC Press, Boca Raton, 1991, p. 1
2. H. Scheer, in *Light-Harvesting Antennas in Photosynthesis*, B. R. Green, W. W. Parson, Eds., Kluwer Academic Publishers, Dordrecht, Netherlands, 2003, p. 29

3. H. Küpper, E. Lombi, F. J. Zhao, G. Wieshammer, S. P. McGrath, *J. Exp. Botany* **52** (2001) 2291
4. H. Küpper, E. Lombi, F. J. Zhao, S. P. McGrath, *Planta* **212** (2000) 75
5. C. Jegerchöld, J. B. Arellano, W. P. Schröder, P. J. M. Kan, M. Baron, S. Styring, *Biochemistry* **34** (1995) 12747
6. B. D. Hsu, J.Y. Lee, *Plant Physiol.* **87** (1988) 116
7. G. Samson , J. C. Morissette, R. Popović, *Photochem. Photobiol.* **48** (1988) 329
8. H. Küpper, F. Küpper, M. Spiller, *J. Exp. Botany* **47** (1996) 259
9. L. F. De Filippis, C. K. Pallaghy, *Z. Pflanzenphysiol.* **78** (1976) 314
10. L. F. De Filippis, *Z. Pflanzenphysiol.* **93** (1979) 129
11. H. Küpper, I. Šetlik, M. Spiller, F. C. Küpper, O. Prášil, *J. Phycol.* **48** (2002) 429
12. H. Kupper, F. Kupper, M. Spiller *Photosynth. Res.* **58** (1998) 123
13. H. Kupper, F. Kupper, M. Spiller, *in Advances in Photosynthesis: Chlorophylls and Bacteryophylls; Biochemistry, Biophysics, Functions and Applications*, B. Grimm, R. Porra, W. Rudigger, H. Scheer, Eds., Springer, Dordrecht, Netherlands, 2006, p. 67
14. H. Clijsters, F. Van Assche, *Photosynth. Res.* **7** (1985) 31
15. C. M. Luna, C. A. González, V. S. Trippi, *Plant Cell Physiol.* **35** (1994) 5
16. P. H. Hynninen, in *Chlorophylls*, H. Scheer, Ed., CRC Press, Boca Raton, 1991, p. 145
17. R. C. White, I. D. Jones, E. Gibbs, L. S. Butler, *J. Agr. Food Chem.* **25** (1977) 143
18. I. D. Jones, R. C. White, E. Gibbs, C. D. Denard, *J. Agr. Food Chem.* **16** (1968) 80
19. L. J. Boucher, J. J. Katz, *J. Am. Chem. Soc.* **89** (1967) 4703
20. H. Scheer, J. J. Katz, *J. Am. Chem. Soc.* **100** (1978) 561
21. H. Scheer, J. J. Katz, *J. Am. Chem. Soc.* **97** (1975) 3273
22. J. Petrović, G. Nikolić, D. Marković, *J. Serb. Chem. Soc.* **71** (2006) 501
23. M. Baron, J. B. Arellano, J. L. Gorge, *Physiol. Plant.* **94** (1995) 174
24. S. Roulin, U. Feller, *Planta* **205** (1998) 297
25. I. Yruela, G. Montoya, R. Picorel, *Photosynth. Res.* **33** (1992) 227
26. J. L. Stauber, T. M. Florence, *Mar. Biol.* **94** (1987) 511
27. M. Renganathan, S. Bose, *Photosynth. Res.* **23** (1990) 95
28. J. A. Raven, M. C. W. Evans, R. E. Korb, *Photosynth. Res.* **60** (1999) 111
29. M. Uchimura, A. Rival, A. Nato, R. Sandeaux, J. Sandeaux, J. C. Baccou, *J. Appl. Phycol.* **12** (2000) 15
30. Z. G. Cerović, M. Plesničar, *Biochem. J.* **223** (1984) 543
31. D. A. Walker, Z. G. Cerović, S. P. Robinson, *Methods Enzymol.* **148** (1987) 145
32. C. A. Price, J. C. Cushman, L. R. Mendiola–Morgenthaler, E. M. Reardon, *Methods Enzymol.* **148** (1987) 157
33. H. K. Lichtenthaler, *Methods Enzymol.* **148** (1987) 350
34. A. J. Hoff, J. Amesz, in *Chlorophylls*, H. Scheer, Ed., CRC Press, Boca Raton, 1991, p. 724
35. L. K. Hanson, in *Chlorophylls*, H. Scheer, Ed., CRC Press, Boca Raton, 1991, p. 994
36. K. K. Karukstis, in *Chlorophylls*, H. Scheer, Ed., CRC Press, Boca Raton, 1991, p. 770
37. M. Ciscato, J. Vangronsveld, R. Valcke, *Z. Naturforsch.* **54c** (1999) 735
38. N. Boucher, R. Carpentier, *Photosynth. Res.* **59** (1999) 167
39. M. Kobayashi, M. Akiyama, H. Kano, H. Kise, in *Advances in Photosynthesis: Chlorophylls and Bacteryophylls; Biochenistry, Biophysics, Functions and Applications*, B. Grimm, R. Porra, W. Rudigger, H. Scheer, Eds., Springer, Dordrecht, Netherlands, 2006, p. 79
40. H. Scheer, in *CRC Handbook of Organic Photochemistry and Photobiology*, W. M. Horspool, P–S. Song, Eds., CRC Press, Boca Raton, 1994, p. 1402
41. S. B. Brown, J. D. Houghton, G. A. F. Henry, in *Chlorophylls*, H. Scheer, Ed., CRC Press, Boca Raton, 1991, p. 465.

Journal of the Serbian Chemical Society
JSCS@tmf.bg.ac.yu • www.shd.org.yu/JSCS

J. Serb. Chem. Soc. 72 (11) 1063–1067 (2007)
JSCS–3640

UDC 547.77+519.85:548.1.023
Original scientific paper

Computing PI and Szeged indices of multiple phenylenes and cyclic hexagonal–square chain consisting of mutually isomorphic hexagonal chains

H. YOUSEFI–AZARI[1]*, J. YAZDANI[1], A. BAHRAMI[1] and A. R. ASHRAFI[2]

[1]*School of Mathematics, Statistics and Computer Science, University of Tehran, Tehran,* [2]*Department of Mathematics, Faculty of Science,University of Kashan, Kashan 87317–51167, Iran*

(Received 28 June, revised 19 December 2006)

Abstract: PI and Szeged indices are two of the most important topological indices defined in chemistry. In this study, the PI and Szeged indices of linear [*n*]-phenylenes and a cyclic hexagonal-square chain consisting of *n* mutually isomorphic hexagonal chains were computed. The PI and Szeged indices of a multiple phenylene, which is the 2-dimensional case of a phenylenic nanotube and nanotorus, were determined.

Keywords: PI index, Szeged index, linear [*n*]-phenylenes, multiple phenylenes nanotube.

INTRODUCTION

Let G be a simple molecular graph without directed and multiple edges and without loops, the vertex and edge-sets of which are represented by $V(G)$ and $E(G)$, respectively. A topological index of a graph G is a numeric quantity related to G. The oldest topological index is the Wiener index. Numerous of its chemical applications have been reported and its mathematical properties are well understood.[1–4]

Khadikar and co-authors[5–9] defined a new topological index and named it the Padmakar–Ivan index. Here Padmakar comes from Padmakar Khadikar, and Ivan from Ivan Gutman. They abbreviated this new topological index as PI. This newly proposed topological index does not coincide with the Wiener index for acyclic molecules. It is defined as $PI(G) = \Sigma_{e\in G}[n_{eu}(e|G) + n_{ev}(e|G)]$, where $n_u(e|G)$ is the number of edges of G lying closer to u than to v and $n_v(e|G)$ is the number of edges of G lying closer to v than to u.

The Szeged index is another topological index which was introduced by Ivan Gutman.[10–13] To define the Szeged index of a graph G, it is assumed that $e = uv$ is an edge connecting the vertices u and v. Suppose $N_u(e|G)$ is the number of vertices of G lying closer to u and $N_v(e|G)$ is the number of vertices of G lying closer to v. Edges equidistance from u and v are not taken into account. Then the

* Corresponding author. E-mail: hyousefi@ut.ac.ir
doi: 10.2998/JSC0711063Y

Szeged index of the graph G is defined as: $Sz(G) = \sum_{e = uv \in E(G)} N_u(e|G)N_v(e|G)$, see also Ref. 14.

The PI and Szeged indices of some hexagonal graphs containing nanotubes and nanotorus have been computed.[15–19] In this study, this work is continued with the computation of the PI and Szeged indices of some other important classes of chemical graphs. The notation is standard and mainly taken from the literature.[20,21]

RESULTS AND DISCUSSION

PI index of multiple phenylenes and cyclic hexagonal–square chains

In this section, the PI index of linear [n]-phenylenes, multiple phenylenes and a cyclic hexagonal–square chain consisting of n mutually isomorphic hexagonal chains are computed.[22,23] To do this, suppose that G is a graph, $e = uv \in E(G)$ and $N(e) = |E| - [n_{eu}(e|G) + n_{ev}(e|G)]$. Then $PI(G) = |E|^2 - \Sigma_{e \in E} N(e)$. Therefore, for computing the PI index of G, it is sufficient to calculate $N(e)$ for every $e \in E$.

Consider the molecular graph of a linear [n]-phenylene, Fig. 1. Then $|E(T)| = 6h + 2(h–1) = 8h – 2$ and, hence, $PI(T) = 64h^2 – 32h + 4 – \Sigma_{e \in E} N(e)$. To calculate $N(e)$, three cases are considered, *i.e.*, that e is vertical, horizontal or oblique. If e is horizontal or oblique, then $N(e) = 2$ and for vertical edges, one has $N(e) = 2h$. Thus, $PI(T) = 60h^2 – 44h + 8$.

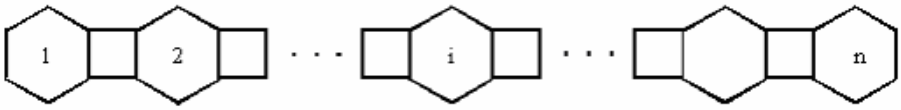

Fig. 1. The molecular graph of a linear [n]-phenylene.

Suppose $X_{m,n}$ is the chemical graph of a multiple phenylene, Fig. 2. Applying our method for computing $PI(X_{m,n})$, suppose $\alpha = \text{Min}\{m,n\}$. It is clear that $|E(X_{m,n})| = 2m(3n–1)$ and, hence, one obtains:

$$\sum_{e \in E(X_{m,n})} N(e) = \sum_{e \text{ is horizontal}} N(e) + \sum_{e \text{ is oblique}} N(e) + \sum_{e \text{ is vertical}} N(e) =$$

$$= 2\left\{ \sum_{i=0}^{\alpha-2} 2(2+2i)^2 + 4\alpha^2(|m-n|+1) \right\} + 4m^2(n-1) + 4n^2m = \frac{8}{3}\alpha + 8\alpha^2 + \frac{16}{3}\alpha^3 +$$

$$+ 16\alpha^2|m-n| + 4m^2n - 4m^2 + 4n^2m$$

Therefore, $PI(X_{m,n}) = 36m^2n^2 – 28m^2n + 8m^2 – 8/3\alpha – 8\alpha^2 – 16/3\alpha^3 – 16\alpha^2|m–n| – 4n^2m$.

Let $C_{m,n}$ denote the molecular graph of a cyclic hexagonal-square chain consisting of n mutually isomorphic hexagonal chains H_1, H_2,…, H_n, cyclically concatenated by circuits α_i of length 4, in which the H_is are chains containing m hexagons, Fig. 3. Some exact formulas for the algebraic structure count (ASC) of the linear [n]-phenylene, Fig. 1, the multiple phenylenes, Fig. 2 and the molecu-

lar graph of $C_{m,n}$, Fig. 3 were computed.[20,21] At the end of this section, PI($C_{m,n}$) is computed.

Obviously, $|E(C_{m,n})| = n(5m+3)$. Hence, one obtains:

$$\mathrm{PI}(C_{m,n}) = n^2(5m+3)^2 - \sum_{e\in E(C_{m,n})} N(e) = n^2(5m+3)^2 - \sum_{e \text{ is horizontal}} N(e) +$$

$$+ \sum_{e \text{ is oblique}} N(e) + \sum_{e \text{ is vertical}} N(e) = 25m^2n^2 + 9n^2 + 30mn^2 - 33n - nm^2 - 66mn.$$

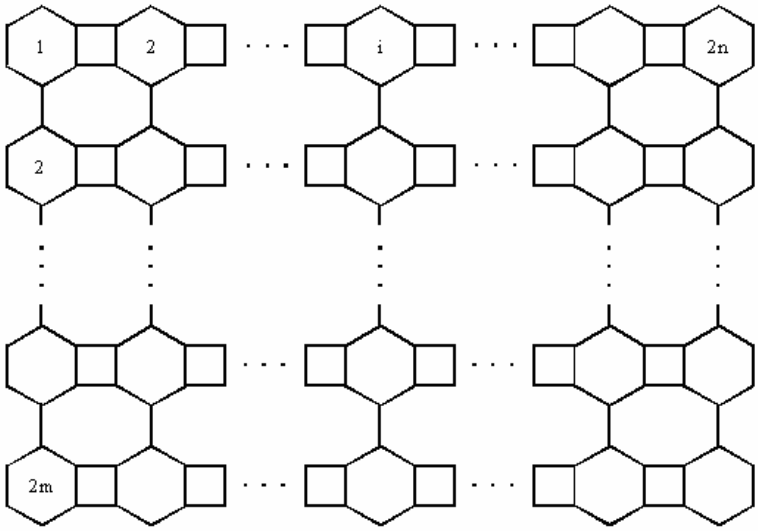

Fig. 2. The molecular graph of a multiple phenylene.

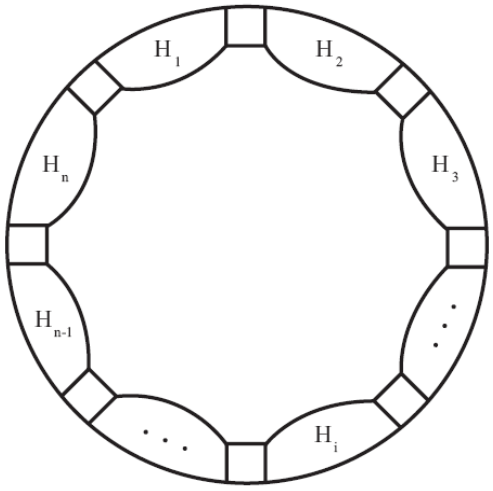

Fig. 3. The molecular graph of a cyclic hexagonal-square chain $C_{m,n}$.

Szeged index of multiple phenylenes and cyclic hexagonal-square chains

In the literature, there is a paper by Diudea in which the Szeged index is tested in QSPR.[24] In this paper, the use of the Szeged index and several other

distance-based indices on the correlation with the boiling points of 45 cycloalkanes were examined. Moreover, Khadikar *et al*.[25] described various applications of the Szeged index for modeling physicochemical properties, as well as the physiological activities of organic compounds acting as drugs or possessing pharmacological activity. The authors of this paper reviewed 175 papers published on the subject of the Szeged index. This shows that the subject of the Szeged index is growing more and more in chemistry, physics and also biology.

In this section, the Szeged index of the linear [n]-phenylene $X_{1,n}$, the multiple phenylene $X_{m,n}$ and $C_{m,n}$ were computed. First it should be noticed that $v_1 = |V(X_{1,n})| = 6n$, $v_2 = |V(X_{m,n})| = 6mn$ and $v_3 = |V(C_{m,n})| = 4mn+2n$. The Szeged index of $X_{1,n}$ was first calculated. To do this, it was assumed that A, B and C to be the set of all vertical, oblique and horizontal edges, respectively. Then one obtains:

$$\mathrm{Sz}(X_{1,n}) = \sum_{e\in E} N_u(e)N_v(e) = \sum_{e\in A} N_u(e)N_v(e) + \sum_{e\in B} N_u(e)N_v(e) + \sum_{e\in C} N_u(e)N_v(e) =$$

$$= \sum_{i=0}^{n-1} 2\{(3+6i)(6n-6i-3)\} + 18n^3 + \sum_{i=1}^{n-1}(12i) = 30n^3 + 6n^2$$

Then the Szeged index of a multiple phenylene $X_{m,n}$ was calculated. Similarly,

$$\mathrm{Sz}(X_{m,n}) = \sum_{e\in E} N_u(e)N_v(e) = \sum_{e\in A} N_u(e)N_v(e) + \sum_{e\in B} N_u(e)N_v(e) + \sum_{e\in C} N_u(e)N_v(e) =$$

$$= \sum_{i=1}^{n-1} \{(6mi)(6nm-6mi)(2m)\} + \sum_{i=1}^{2m-1}\{(3ni)(6nm-6ni)(2n)\} + \sum_{e\in B} N_u(e)N_v(e).$$

To compute the last summation, it was supposed that $U = \sum_{e\in B} N_u(e)N_v(e)$ and two separate cases were considered, as follows:

Case 1: $m \neq n$. In this case one obtains:

$$U = \sum_{i=1}^{|m-n|-1}\{(2\beta)(S_\beta + (6\beta-3)i))(6mn - S_\beta - (6\beta-3)i\},$$

where $S_i = 3+9+15+\ldots+(6i-3)$ and $\beta = \min(m,n)$. Hence, the Szeged index of $X_{m,n}$ is equal to $9\beta^2nm-18n+9mn\beta+18mn\beta^3+3/2\beta^2-15/2\beta^4-9\beta^5-3\beta^6+72n^2+72n^3m-$ $-36mn^2+36mn^4-72n^4-36n^3-18n^5$.

Case 2: $m = n$. In this case one has $U = 2n(S_n+6n-3)(6nm-S_n-6n+3)$ and hence the Szeged index of $X_{m,n}$ is equal to $6n^6+27n^5+3/2n^4-72n^3+147/2n^2-18n$.

In the end of this section, the Szeged index of $C_{m,n}$ is computed. Obviously, $v_3 = |V(C_{m,n})| = 2n(2m+1)$. If A, B and C are set as before, then

$$\mathrm{Sz}(C_{m,n}) = \sum_{e\in E} N_u(e)N_v(e) = \sum_{e\in A} N_u(e)N_v(e) + \sum_{e\in B} N_u(e)N_v(e) +$$

$$\sum_{e\in C} N_u(e)N_v(e) = n(m+1)(2m+1)(v_3)(2m-1) + 2n(v_3/2)(v_3/2) +$$

$$+ 4mn(v_3/2)(v_3/2) = 16m^2n^2 + 8m^3n^2 - 4nm^2 + 10mn^2 - 5mn + 2n^2 - n +$$

$$+ 24m^2n^3 + 16m^3n^3 + 12mn^3 + 2n^3.$$

И З В О Д

ИЗРАЧУНАВАЊЕ PI И SZEGED ИНДЕКСА ВИШЕСТРУКИХ ФЕНИЛЕНА И ЦИКЛИЧНОГ ХЕКСАГОНАЛНО–КВАДРАТНОГ ЛАНЦА САЧИЊЕНОГ ОД МЕЂУСОБНО ИЗОМОРФНИХ ХЕКСАГОНАЛНИХ ЛАНАЦА

H. YOUSEFI–AZARI[1], J. YAZDANI[1], A. BAHRAMI[1] и A. R. ASHRAFI[2]

[1]*School of Mathematics, Statistics and Computer Science, University of Tehran, Tehran,* [2]*Department of Mathematics, Faculty of Science,University of Kashan, Kashan 87317–51167, Iran*

PI и Szeged индекси су два најважнија тополошка индекса дефинисана у хемији. У овом раду су израчунати PI и Szeged индекси линеарних [*n*]-фенилена и цикличног хексагонално–квадратног ланца сачињеног од *n* међусобно изоморфних хексагоналних ланаца. Одређени су PI и Szeged индекси вишеструког фенилена, као дводимензионог облика фениленских наноцеви и нанопрстена.

(Примљено 28. јуна, ревидирано 19. децембра 2006)

REFERENCES

1. H. Wiener, *J. Am. Chem. Soc*. **69** (1947) 17
2. R. Todeschini, V. Consonni, *Handbook of Molecular Descriptors*, Wiley, Weinheim, 2000
3. D. E. Needham, I. C. Wei, P. G. Seybold, *J. Am. Chem. Soc*. **110** (1988) 4186
4. G. Rucker, C. Rucker, *J. Chem. Inf. Comput. Sci*. **39** (1999) 788
5. P. V. Khadikar, *Nat. Acad. Sci. Lett*. **23** (2000) 113
6. P. V. Khadikar, P. P. Kale, N. V. Deshpande, S. Karmarkar, V. K. Agrawal, J. *Math. Chem*. **29** (2001) 143
7. P. V. Khadikar, S. Karmarkar, *J. Chem. Inf. Comput. Sci*. **41** (2001) 934
8. P. V. Khadikar, S. Karmarkar, R. G. Varma, *Acta Chim. Slov*. **49** (2002) 755
9. P. E. John, P. V. Khadikar, J. Singh, *J. Math. Chem*. **42** (2007) 37
10. I. Gutman, *Graph Theory Notes of NY* **27** (1994) 9
11. A. Das, G. Domotor, I. Gutman, S. Joshi, S. Karmarkar, D. Khaddar, T. Khaddar, P. V. Khadikar, L. Popovic, N. S. Sapre, N. Sapre, A. Shirhatti, *J. Serb. Chem. Soc*. **62** (1997) 235
12. O. M. Minailiuc, G. Katona, M. V. Diudea, M. Strunje, A. Graovac, I. Gutman, *Croat. Chem. Acta* **71** (1998) 473
13. M. V. Diudea, I. Gutman, *Croat. Chem. Acta* **71** (1998) 21
14. S. Karmarkar, S. Karmarkar, S. Joshi, A. Das, P. V. Khadikar, *J. Serb. Chem. Soc*. **62** (1997) 227
15. H. Yousefi–Azari, B. Manoochehrian, A. R. Ashrafi, *Curr. Appl. Phys*. (2007), doi:10.1016/j.cap.2007.04.024
16. A. R. Ashrafi, A. Loghman, *MATCH Commun. Math. Comput. Chem*. **55** (2006) 447
17. A. R. Ashrafi, A. Loghman, *J. Comput. Theor. Nanosci*. **3** (2006) 378
18. A.R. Ashrafi, F. Rezaei, *MATCH Commun. Math. Comput. Chem*. **57** (2007) 243
19. H. Yousefi–Azari, A. R. Ashrafi, A. Bahrami, J. Yazdani, *Asian J. Chem*. **20** (2008) 15
20. P. J. Cameron, *Combinatorics: Topics, Techniques, Algorithms*, Cambridge University Press, Cambridge, 1994
21. N. Trinajstic, *Chemical Graph Theory*, CRC Press7, Boca Raton, FL, 1992
22. O. Bodroža–Pantic, R. Doroslovacki, *J. Math. Chem*. **35** (2004) 139
23. I. Gutman, *Z. Naturforsch*. **A39** (1984) 794
24. M. Diudea, *J. Chem. Inf. Comput. Sci*. **37** (1997) 300
25. P. V. Khadikar, S. Karmarkar, V. K. Agrawal, J. Singh, A. Shrivastava, I. Lukovits, M. V. Diudea, *Lett. Drug. Des. Discov*. **2** (2005) 606.

Journal of the Serbian Chemical Society
JSCS@tmf.bg.ac.yu • www.shd.org.yu/JSCS

J. Serb. Chem. Soc. 72 (11) 1069–1074 (2007) UDC 546.713'723'763.004.10:54–71–034:542.913
JSCS–3641 *Original scientific paper*

Trivalent metal ion directed synthesis and characterization of macrocyclic complexes

DHARAM PAL SINGH* and RAMESH KUMAR

Department of Chemistry, National Institute of Technology, Kurukshetra-136 119, India

(Received 22 January, revised 15 June 2007)

Abstract: A novel series of complexes of the type $[M(TML)X]X_2$, where TML is a tetradentate macrocyclic ligand, M = Cr(III), Mn(III) or Fe(III), X = Cl^-, CH_3COO^- or NO_3^-, were synthesized by template condensation of dibenzoyl and thiocarbohydrazide in the presence of trivalent metal salts in a methanolic medium. The complexes were characterized with the help of elemental analyses, conductance measurements, molecular weight determination, magnetic measurements, electronic, NMR, infrared and far infrared spectral studies. The electronic spectra together with the magnetic moments suggest five coordinate square pyramidal geometry for these complexes. The molar conductance indicates them to be 1:2 electrolytes.

Keywords: macrocyclic complexes, dibenzoyl, trivalent metal salts, thiocarbohydrazide, template synthesis.

INTRODUCTION

The field of coordination chemistry of macrocyclic complexes has undergone spectacular growth during the past few decades. This enormous growth is due to the synthesis of a large number and variety of synthetic macrocycles, which behave as coordinating agents for metal ions.[1,2] Template reactions have been widely used as the synthetic routes for macrocyclic complexes.[3–5] Nitrogen containing macrocycles have a strong tendency to form stable complexes with transition metals.[6] A number of nitrogen donor macrocyclic derivatives have long been used in analytical, industrial and medical applications.[7] Macrocyclic transition metal complexes have been regarded as being better model compounds for metalloporphyrins and metallocorrins.[8–11] Some macrocyclic complexes have been reported to exhibit antibacterial and antifungal activities.[12,13] In a previous paper, divalent metal macrocyclic complexes derived from thiocarbohydrazide and dibenzoyl were reported.[13] In the present paper, the trivalent chromium, manganese and iron complexes derived from thiocarbohydrazide and dibenzoil are discussed.

* Author for correspondence.
doi: 10.2298/JSC0711069S

EXPERIMENTAL

All the complexes described in this paper were obtained by template synthesis. To a stirring MeOH solution (≈ 50 cm^3) of thiocarbohydrazide (10 mmol) was added trivalent chromium, manganese or iron salt (5 mmol) dissolved in the minimum quantity of MeOH (20 cm^3). The resulting solution was refluxed for 0.5 h. Subsequently, dibenzoyl (10 mmol) dissolved in ≈ 20 cm^3 MeOH was added to the refluxing mixture and the refluxing was continued for 6−8 h. The mixture was concentrated to half its volume and kept in a desiccator for two days. The complexes were then filtered, washed with MeOH, Me_2CO and Et_2O and dried *in vacuo*; yield ≈ 45 %. The complexes are soluble in DMF and DMSO but are insoluble in other common organic solvents and water. They were thermally stable up to ≈ 225–250 °C and then decomposed.

Analytical and physical measurements

The microanalysis of C, H, and N were recorded using an Elementar Vario EL III (Carlo Erba 1108) at CDRI, Lucknow. The metal percentage was determined by the EDTA titration method. The molecular weight was determined cryoscopically. The magnetic susceptibility measurements were performed on a Vibrating Sample Magnetometer (PAR 155) at IIT Roorkee. The electronic spectra were recorded on a Perkin–Elmer spectrophotometer. The IR spectra were recorded on a Beckman infrared spectrophotometer in the range 4000–667 cm^{-1} as KBr pellets. The NMR spectra were recorded on a Bruker NMR spectrometer (300 MHz). The conductivity was measured on a digital conductivity meter (HPG System, G-3001).

RESULTS AND DISCUSSION

Several attempts to isolate the free macrocyclic ligand were unsuccessful. The template synthesis of the complexes may be shown by the following scheme:

$$2SC(NHNH_2)_2 + 2(C_6H_5CO)_2 + MX_3 \xrightarrow{\text{MeOH, 6–8 h}} [M(TML)X]X_2$$

where M = Cr(III), Mn(III) or Fe(III), X = Cl^-, CH_3COO^- or NO_3^- and TML = tetradentate macrocyclic ligand.

The analytical data of the metal chelates are given in Table I, which shows that the chelates may be represented by the formula: $[M(C_{30}H_{24}N_8S_2)X]X_2$. The measurements of the molar conductance in DMSO show that these chelates are 1:2 electrolytes (conductance 150−180 Ω^{-1} cm^2 mol^{-1}).[14] The test for anions was positive before decomposing and after decomposing, the chelates showed their presence outside and inside of the coordination sphere.

The presence of a single medium band in the region ≈ 3250−3300 cm^{-1} in the complexes may be assigned to N–H stretch.[15,16] It was noted that a pair of bands corresponding to ν(NH_2) at 3245 cm^{-1} and 3309 cm^{-1} are present in the spectrum of the thiocarbohydrazide but are absent in the infrared spectra of all the complexes. Furthermore, the disappearance of the absorption band near 1700 cm^{-1} due to ν(C=O) and the appearance of an absorption band near 1595−1615 cm^{-1} indicates the formation of a macrocyclic Schiff's base.[17] The lower values of ν(C=N) may be explained on the basis of a drift of the lone pair density of the azomethine nitrogen towards the metal atom,[18,19] indicating that coordination occurs through the nitrogen of the C=N groups. Another set of medium intensity bands in the region ≈ 1490−1580 cm^{-1} are attributed to ν(C=C) of phenyl groups

and the bands at ≈ 840−880 cm^{-1} to C–H out of plane bending of phenyl groups. The band near 780 cm^{-1} in thiocarbohydrazide may be assigned as being due to free ν(C=S). This band is also present in the spectra of all the complexes, which indicates that sulphur is not coordinating to the metal atom.[20,21] The absence of bands near 2550 cm^{-1} (characteristic of a thiol group) rules out the possibility of thione–thiol tautomerism.[21] The C–N stretch occurs in the range 1300−1000 cm^{-1}.

TABLE I. Analytical data of the trivalent chromium, manganese and iron complexes derived from thiocarbohydrazide and dibenzoyl

Complexes	M	C	H	N	Colour	M_r g mol^{-1}
$[Cr(C_{30}H_{24}N_8S_2)Cl]Cl_2$	7.16 (7.23)	49.87 (50.06)	3.27 (3.33)	15.34 (15.57)	Greenish brown	719
$[Cr(C_{30}H_{24}N_8S_2)(NO_3)](NO_3)_2$	6.43 (6.51)	45.08 (45.11)	2.97 (3.00)	19.20 (19.29)	Light brown	798
$[Cr(C_{30}H_{24}N_8S_2)(OAc)](OAc)_2$	6.47 (6.59)	54.56 (54.75)	4.09 (4.18)	14.15 (14.19)	Yellowish brown	789
$[Mn(C_{30}H_{24}N_8S_2)Cl]Cl_2$	7.68 (7.61)	49.67 (49.86)	3.19 (3.32)	15.37 (15.51)	Dark brown	722
$[Mn(C_{30}H_{24}N_8S_2)(OAc)](OAc)_2$	6.89 (6.94)	54.23 (54.54)	4.06 (4.16)	14.12 (14.14)	Blackish brown	792
$[Fe(C_{30}H_{24}N_8S_2)Cl]Cl_2$	7.68 (7.74)	49.67 (49.79)	3.19 (3.31)	15.37 (15.49)	Orange red	723
$[Fe(C_{30}H_{24}N_8S_2)(NO_3)](NO_3)_2$	6.89 (6.98)	44.79 (44.88)	2.78 (2.99)	19.11 (19.20)	Reddish brown	802
$[Fe(C_{30}H_{24}N_8S_2)(OAc)](OAc)_2$	6.92 (7.06)	54.43 (54.47)	4.11 (4.16)	14.05 (14.12)	Dark brown	793

The far IR spectra show bands in the region ≈ 420−470 cm^{-1} corresponding to ν(M−N) vibrations.[22−24] The presence of bands in the spectra of all the complexes in the 420−470 cm^{-1} region originate from (M−N) azomethine vibrational modes and gives some indication about the coordination of azomethine nitrogens.[25] The bands present at 290−310 cm^{-1} may be assigned to ν(M−Cl) vibrations.[22] The characteristic bands due to ν(M−S) are not present in the far IR spectra, which again rules out the possibility of coordination through sulphur atom.

The ^{1}H-NMR spectra of the complexes show peaks at 7.08−7.78 ppm (multiplets), corresponding to aromatic ring protons.[26] The singlet at 11.7−12.1 ppm may be assigned to −NH protons.[27]

The magnetic moment of the chromium complexes was in the range from 4.12 to 4.46 μ_B. The electronic spectra of the chromium complexes show bands at ≈ 9000−9300 cm^{-1}, 13000−13300 cm^{-1}, 17450−18300 cm^{-1}, 27400−27800 cm^{-1} and 34800 cm^{-1}. However, these spectral bands cannot be interpreted in terms of four or six coordinated environment around the metal atom. In turn, the spectra are consistent with that of five coordinated Cr(III) complexes, the structures of which

have been confirmed from X-ray measurements.[28] Thus, bearing in mind the analytical data and electrolytic nature of these complexes, a five coordinated square pyramidal geometry can be assumed for these complexes. Thus, assuming the symmetry C_{4V} for these complexes,[29] the various spectral bands can be assigned as: $^4B_1 \rightarrow {}^4E^a$, $^4B_1 \rightarrow {}^4B_2$, $^4B_1 \rightarrow {}^4A_2$ and $^4B_1 \rightarrow {}^4E^b$.

The magnetic moment of the manganese complexes lay in the range from 4.85 to 4.92 μ_B. The manganese complexes show bands in their electronic spectra which lay in the range 22200−12570 cm^{-1}, 16000−18900 cm^{-1} and 35400−35700 cm^{-1}. The higher energy band at 35400−35700 cm^{-1} may be assigned to charge transfer transitions. The spectra resemble those reported for five coordinate square pyramidal manganese porphyrins.[25,29] This idea is further supported by the presence of the broad ligand field band at 20400 cm^{-1}, diagnostic of C_{4V} symmetry, and thus the various bands may be assigned as follows: $^5B_1 \rightarrow {}^5A_1$, $^5B_1 \rightarrow {}^5B_2$, and $^5B_1 \rightarrow {}^5E$, respectively. The band assignment in single electron transition may be made as: $d_{z^2} \rightarrow d_{x^2-y^2}$, $d_{xy} \rightarrow d_{x^2-y^2}$ and d_{xy}, $d_{yz} \rightarrow d_{x^2-y^2}$, respectively, in order of increasing energy. However, the complexes do not have an idealized C_{4V} symmetry.

The magnetic moment of the iron complexes lay in the range from 5.78 to 5.94 μ_B. The iron (III) complexes show bands in their electronic spectra in the range 9830−9980 cm^{-1}, 15500−15580 cm^{-1} and 27500−27700 cm^{-1} and these bands do not suggest an octahedral or tetrahedral geometry around the metal atom. The spectral bands are consistent with the range of spectral bands reported for five coordinate square pyramidal iron(III) complexes.[30] Assuming C_{4V} symmetry for these complexes, the various bands can be assigned as: $d_{xy} \rightarrow d_{xz}$, d_{yz} and $d_{xy} \rightarrow d_{z^2}$. Any attempt to make an accurate assignment is difficult due to the interactions of the metal–ligand π-bond systems lifting the degeneracy of the d_{xz} and d_{yz} pair.

Based on all the above-given results, the proposed structure of the complexes described in this paper is as shown in Fig. 1.

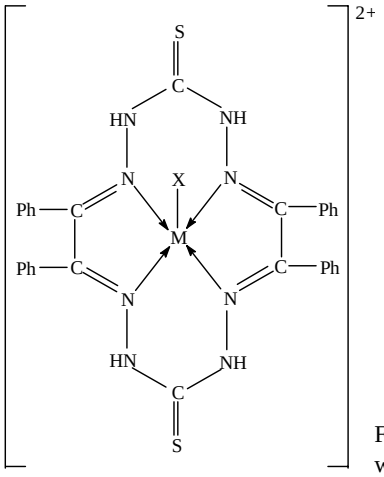

Fig. 1. The proposed structure of the $[M(C_{30}H_{24}N_8S_2)X]^{2+}$, where M(III) = Cr, Mn or Fe and X = Cl^-, NO_3^- or $CH3COO^-$.

Acknowledgements: D.P. Singh thanks the University Grants Commission, New Delhi for financial support in the form of a Major Research Project (MRP-F.12-62/2003) and Ramesh Kumar for the award of a Project Fellow under the above project. Thanks are also due to the authorities of N.I.T., Kurukshetra, for providing the necessary facilities.

ИЗВОД

УСМЕРЕНА СИНТЕЗА И КАРАКТЕРИЗАЦИЈА МАКРОЦИКЛИЧНИХ КОМПЛЕКСА ТРОВАЛЕНТНИХ МЕТАЛНИХ ЈОНА

DHARAM PAL SINGH и RAMESH KUMAR

Department of Chemistry, National Institute of Technology, Kurukshetra–136 119, India

Нова серија комплекса типа $[M(TML)X]X_2$, где је TML тетрадентантни макроциклични лиганд, M = Cr(III), Mn(III) или Fe(III) и X = Cl^-, CH_3COO^- или NO_3^-, синтентисана је темплатном кондензацијом дибензоила и тиокарбохидразида у метанолу, у присуству тровалентних соли метала. Комплекси су окарактерисани елементалном анализом, мерењем проводљивости, одређивањем молекулске масе, магнетним мерењима и електронским, NMR, инфрацрвеним и далеким инфрацрвеним спектралним испитивањима. Електронски спектри и вредности магнетних момената комплекса указују на њихову квадратну пирамидалну структуру са координационим бројем пет. Моларна проводљивост указује на то да су комплекси 1:2 електролити.

(Примљено 22. јануара, ревидирано 15. јуна 2007)

REFERENCES

1. a) Y. Gok, H. Kantekin, *Polyhedron* **16** (1997) 2413; b) M. Fernandez, R. Basitida, A. Macias, L. Valencia, P. Lourido, *Polyhedron* **25** (2006) 783
2. L. F. Lindoy, *The Chemistry of Macrocyclic Ligand Complexes*, Cambridge University Press, Cambridge, 1989
3. R. N. Prasad, N. Gupta, *J. Serb. Chem. Soc.* **68** (2003) 455
4. M. S. Niasari, F. Davar, *Inorg. Chem. Commun.* **9** (2006) 175
5. M. S. Niasari, H. Najafian, *Polyhedron* **22** (2003) 2633
6. R. N. Prasad, S. Gupta, *J. Serb. Chem. Soc.* **67** (2002) 523
7. W. Ma, Y. Tian, S. Zhang, J. Wu, *Transition Met. Chem.* **31** (2006) 97
8. D. P. Singh, N. Shoshodia, B. P. Yadav, V. B. Rana, *Polyhedron* **16** (1997) 2229
9. K. H. Reddy, M. R. Reddy, K. M. Raju, *Polyhedron* **16** (1997) 2673
10. S. Chandra, L. K. Gupta, *J. Indian Chem. Soc.* **82** (2005) 454
11. A. Chaudhary, R. V. Singh, *Indian J. Chem.* **43A** (2004) 2529
12. A. Chaudhary, N. Bansal, A. Gajraj, R.V. Singh, *J. Inorg. Biochem.* **96** (2003) 393
13. D. P. Singh, R. Kumar, P. Tyagi, *Transition Met. Chem.* **31** (2006) 970
14. R. Kumar, R. Singh, *Turk. J. Chem.* **30** (2006) 77
15. M. Shakir, O. S. M. Nasman, S. P. Varkey, *Polyhedron* **15** (1996) 309
16. G. A. Bain, D. X. West, J. Krejci, J. V. Martinez, S. H. Ortega, R. A. Toscano, *Polyhedron* **16** (1997) 855
17. J. R. Anacona, E. Bastardo, *Transition Met. Chem.* **24** (1999) 478
18. S. Chandra, S. D. Sharma, *Transition Met. Chem.* **27** (2002) 732
19. C. Lodeiro, R. Basitida, E. Bertolo, A. Macias, R. Rodriguez, *Transition Met. Chem.* **28** (2003) 388
20. O. V. Mikhailov, M. R. Kazymova, T. A. Shumilova, S. S. Solovieva, *Transition Met. Chem.* **29** (2004) 732
21. S. Chandra, S. Thakur, *Transition Met. Chem.* **29** (2004) 925

22. a) M. Shakir, K. S. Islam, A. K. Mohamed, N. Jahan, *Transition Met. Chem.* **22** (1997) 189; b) T. A. Khan, S. S. Hasan, S. P. Varkey, M. A. Rather, N. Jahan, M. Shakir, *Transition Met. Chem.* **22** (1997) 4
23. T. A. Khan, M. Shagufta, *Transition Met. Chem.* **24** (1999) 669
24. A. K. Singh, A. Panwar, R. Singh, S. Beniwal, *Transition Met. Chem.* **28**(2003) 160
25. V. B. Rana, D. P. Singh, P. Singh, M. P. Teotia, *Transition Met. Chem.* **7** (1982) 174
26. R. N. Prasad, M. Agrawal, M. Sharma, *J. Serb. Chem. Soc.* **67** (2002) 229
27. A. D. Naik, S. M. Annigeri, U. B. Gangadharmath, V. K. Revankar, V. B. Mahale, *J. Inclusion Phenom. Macrocyclic Chem.* **43** (2002) 291
28. J. S. Wood, *Prog. Inorg. Chem.* **16** (1972) 227
29. D. P. Singh, V. B. Rana, *Polyhedron* **14** (1995) 2901
30. A. B. P. Lever, *Inorganic Electronic Spectroscopy*, Elsevier, Amsterdam, 1968.

Journal of the Serbian Chemical Society
JSCS@tmf.bg.ac.yu • www.shd.org.yu/JSCS

J. Serb. Chem. Soc. 72 (11) 1075–1084 (2007) UDC 546.742'562'472:542.9+547.571+547.551:543.422.25
JSCS–3642 *Original scientific paper*

Metal complexes of Schiff's bases derived from 3-(arylazo)-2,4--pentanediones with 2-aminophenol and 2-aminothiophenol

K. KRISHNANKUTTY[1]*, P. SAYUDEVI[2] and MUHAMMED BASHEER UMMATHUR[3]

[1]*Department of Chemistry, University of Calicut, Kerala–673635,* [2]*Department of Chemistry, NSS College, Manjeri, Kerala–676122 and* [3]*Department of Chemistry, Unity Women's College, Manjeri, Kerala–676122, India*

(Received 8 February 2007)

Abstract: Phenylazo- and thiazolylazo-2,4-pentanediones on reaction with 2-aminophenol and 2-aminothiophenol yielded a new series of polydentate Schiff's base ligands. The structure and tautomeric nature of these compounds and their metal complexes were established on the basis of their IR, ^{1}H-NMR and mass spectral data. The spectral and analytical data revealed the condensation of both carbonyl groups of 3-(2-thiazolylazo)-2,4-pentanedione with 2-aminophenol to form an N_2O_2 tetradentate ligand. Details on the formation of its [ML] complexes with Ni(II), Cu(II) and Zn(II) and the nature of their bonding are discussed based on analytical, IR, ^{1}H-NMR and mass spectral data.

Keywords: 3-(arylazo)-2,4-pentanediones, Schiff's bases, metal complexes, IR spectra, ^{1}H-NMR spectra, mass spectra.

INTRODUCTION

Design and synthesis of polydentate Schiff's bases and their metal complexes having novel structural features and unusual physico–chemical properties have considerable importance in biological processes and constitute an active area of research in modern coordination chemistry.[1] In this context Schiff's bases of 1,3--diketones have been extensively studied.[2] However little attention has been paid to Schiff's bases derived from arylazo derivatives of 1,3-diketones in which two nitrogen donor sites are additionally present. Besides having wide application as yellow dyes and pigments,[3] arylazo-1,3-diketones have been widely used as intermediates in the preparation of a large number of biologically important heterocyclic compounds and as precursors of potential anti-diabetic drugs.[4] As part of our investigation on arylazo derivatives of 1,3-diketones,[5,6] the synthesis and characterization of four Schiff's bases from phenylazo- and thiazolylazo- derivatives of acetylacetone and aromatic amines are reported. Typical metal complexes of these ligand systems were also studied.

* Corresponding author. E-mail: mbummathur@rediffmail.com
doi: 10.2298/JSC0711075K

EXPERIMENTAL

Methods and instruments

Carbon, hydrogen and nitrogen percentages were determined by micro analyses (Heraeus Elemental analyzer) and the metal contents by AAS (Perkin Elmer 2380). The electronic spectra of the compounds were recorded in methanol solution (10^{-4} M) on a 1601 Shimadzu UV–Vis spectrophotometer; the IR spectra (KBr discs) on a 8101 Shimadzu FTIR spectrophotometer; the ^{1}H-NMR spectra ($CDCl_3$ or DMSO-d_6) on a Varian 300 NMR spectrometer; the ESR spectra (X-band) at 77 K using a Varian E 112 ESR spectrometer and the mass spectra on a Jeol/SX-102 mass spectrometer (FAB using argon and *meta*-nitrobenzyl alcohol as the matrix). The molar conductance of the complexes was determined in DMF at 28±1 °C using a solution of about 10^{-3} M concentration. The magnetic susceptibilities were determined at room temperature on a Guoy-type magnetic balance.

Synthesis of Schiff's bases derived from 3-(phenylazo)acetylacetone

The phenylazo derivative of acetylacetone was prepared as previously reported.[5] Condensation of the compound with 2-aminophenol and 2-aminothiophenol yielded the Schiff's bases H_2pap and H_2pat, respectively. The synthetic details are given below.

Synthesis of H_2pap

An ethanolic solution of 2-aminophenol (1.09 g, 0.01 mol, 20 ml) was added to an ethanolic solution of 3-(phenylazo)acetylacetone (2.04 g, 0.01 mol, 20 ml). The mixture was refluxed on a boiling water bath for ≈ 5 h and kept over night. The solution was then poured into hot water (≈ 70 °C) under vigorous stirring. The precipitated compound was filtered, washed with hot water and recrystallized twice from hot methanol to obtain the chromatographically (tlc) pure compound.

Synthesis of H_2pat

An ethanolic solution of 2-aminothiophenol (1.25 g, 0.01 mol, 20 ml) was added to an ethanolic solution of 3-(phenylazo)acetylacetone (2.04 g, 0.01 mol, 20 ml). The mixture was refluxed on a boiling water bath for ≈ 4 h and then the volume was reduced. After cooling to room temperature, the precipitated compound was filtered, washed with an excess water and recrystallized from hot methanol to obtain the chromatographically (tlc) pure compound.

Synthesis of Schiff's bases derived from 3-(2-thiazolylazo)acetylacetone

Thiazolylazo derivative of acetylacetone was prepared as reported.[7] Condensation of the compound with 2-aminophenol and 2-aminothiophenol yielded the Schiff's bases H_2tap and H_2tat. Synthetic details are given below.

Synthesis of H_2tap

An ethanolic solution of 2-aminophenol (1.09 g, 0.01 mol, 20 ml) was added to an ethanolic solution of 3-(2-thiazolylazo)acetylacetone (2.11 g, 0.01 mol, 20 ml) and refluxed on a boiling water bath for ≈ 8 h. The volume was reduced and the mixture poured onto crushed ice under vigorous stirring. The formed precipitate was filtered and recrystallized twice from hot methanol to obtain the chromatographically (tlc) pure compound.

Synthesis of H_2tat

To an ethanolic solution of 3-(2-thiazolylazo)acetylacetone (2.11 g, 0.01 mol, 20 ml) was added dropwise an ethanolic solution of 2-aminothiophenol (1.25 g, 0.01 mol, 20 ml). The solution was stirred for ≈ 9 h in a closed flask, whereby the temperature was maintained between 50 and 55 °C. The formed crystalline product was filtered and recrystallized from hot methanol to obtain the chromatographically (tlc) pure compound.

Synthesis of metal complexes of H_2pap, H_2pat, H_2tap and H_2tat

A concentrated aqueous solution of metal(II) acetate (0.001 mol, 15 ml) was added to an ethanolic solution of the ligand (0.001 mol, 20 ml) and the mixture was refluxed for ≈ 4 h on a boiling

water bath. The solution was kept overnight. The precipitated complex was filtered, washed with water, then with methanol, recrystallized from hot ethanol and dried under vacuum.

RESULTS AND DISCUSSION

The analytical, IR, ^{1}H-NMR and mass spectral data (Tables I and II) of the reaction products of 3-(arylazo)acetylacetone with the aromatic amines suggest that the condensation occurred in a 1:1 ratio, except for 3-(2-thiazolylazo)acetylacetone with 2-aminophenol where a 1:2 condensation product was formed. The analytical data (Table III), together with the non-electrolytic nature in DMF (specific conductance < 10 Ω^{-1}cm^{-1}; 10^{-3} M solution) suggest 1:1 metal ligand stoichiometry of the complexes. The Ni(II) and Zn(II) chelates are diamagnetic while the Cu(II) complexes showed a normal paramagnetic moment. The IR, ^{1}H-NMR and mass spectral data of the Schiff's bases, H_2pap, H_2pat and H_2tat, are in conformity with Fig. 1 and their complexes with Fig. 2. The analytical (Table V) and spectral data of H_2tap are in agreement with Fig. 3 and of its complexes with Fig. 4. These data of the compounds are discussed separately.

TABLE I. Analytical, IR and ^{1}H-NMR spectral data of H_2pap, H_2pat and H_2tat

Compound	M.p. °C	Yield %	Found (Calcd.), %			ν / cm^{-1}			δ / ppm		
			C	H	N	C=O	C=N	C=C	NH	OH/SH	CH_3
H_2pap $C_{17}H_{17}N_3O_2$	72	76	69.00 (69.15)	5.64 (5.76)	14.20 (14.24)	1678	1624, 1618	1591, 1588, 1584, 1580	14.45 (1H)	10.80 (1H)	2.32 (3H), 2.58 (3H)
H_2pat $C_{17}H_{17}N_3SO$	62	70	65.42 (65.60)	5.44 (5.47)	13.43 (13.50)	1672	1622, 1612	1598, 1592, 1586, 1582	14.20 (1H)	6.20 (1H)	2.36 (3H), 2.68 (3H)
H_2tat $C_{13}H_{14}N_4S_2O$	130	74	50.84 (50.98)	4.52 (4.58)	18.33 (18.30)	1670	1630, 1618, 1612	1596, 1590, 1586, 1580	13.25 (1H)	5.85 (1H)	2.38 (3H), 2.72 (3H)

TABLE II. Mass spectral data of H_2pap, H_2pat, H_2tat and their Cu(II) complexes

Compound	*m/z*
H_2pap	295, 252, 218, 203, 202, 175, 160, 125, 93, 92, 77
H_2pat	311, 268, 248, 234, 219, 202, 191,176, 125, 109, 92, 77
H_2tat	306, 263, 229, 222, 215, 207, 197, 186, 154, 109, 99, 91, 84, 77
[Cu(pap)(H_2O)]	376, 374, 333, 331, 299, 297, 282, 280, 252, 218, 202, 160, 92, 77
[Cu(pat)(H_2O)]	392, 390, 349, 347, 377, 375, 315, 313, 299, 268, 248, 219, 191, 176, 109, 92, 77
[Cu(tat)(H_2O)]	387, 385, 344, 342, 308, 303, 301, 294, 276, 260, 258, 229, 222, 207, 154, 109, 91, 84

Characterization of H_2pap, H_2pat, H_2tat and their metal complexes

Infrared spectra. The IR spectra of H_2pap, H_2pat and H_2tat show strong bands at ≈ 1670 cm^{-1} and ≈ 1625 cm^{-1} due to ν(C=O) and ν(C=N) vibrations, respecti-

vely.[8] The thiazole C=N of H_2tat is observed at 1612 cm^{-1}. The ν(C=C) vibrations of the aromatic rings are observed as several medium intensity bands in the 1580−1600 cm^{-1} region (Table I).[9] The broad band observed in the 2500−3500 cm^{-1} region is due to the intramolecularly hydrogen-bonded N–H proton. A slightly broadened medium intensity band which appeared at ≈ 2425 cm^{-1} in the spectra of H_2pat and H_2tat can be assigned to ν(S–H).

TABLE III. Physical and analytical data of the metal complexes of H_2pap, H_2pat and H_2tat

Complex	Yield %	M.p. °C	Found (Calcd.), %			
			C	H	N	M
[Ni(pap)(H_2O)], $C_{17}H_{17}N_3NiO_3$	70	298	55.34 (55.18)	4.76 (4.60)	11.58 (11.36)	15.96 (15.88)
[Ni(pat)(H_2O)], $C_{17}H_{17}N_3NiSO_2$	65	286	53.00 (52.90)	4.40 (4.41)	10.72 (10.89)	15.36 (15.22)
[Ni(tat)(H_2O)], $C_{13}H_{14}N_4NiS_2O_2$	72	293	44.00 (40.98)	3.71 (3.68)	14.80 (14.71)	15.58 (15.42)
[Cu(pap)(H_2O)], $C_{17}H_{17}CuN_3O_3$	76	296	54.56 (54.47)	4.66 (4.54)	11.37 (11.21)	16.80 (16.96)
[Cu(pat)(H_2O)], $C_{17}H_{17}CuN_3SO_2$	74	288	52.12 (52.24)	4.30 (4.35)	10.60 (10.75)	16.32 (16.27)
[Cu(tat)(H_2O)], $C_{13}H_{14}CuN_4S_2O_2$	68	284	40.45 (40.46)	3.70 (3.63)	14.42 (14.53)	16.50 (16.48)
[Zn(pap)(H_2O)], $C_{17}H_{17}N_3O_3Zn$	72	244	54.30 (54.20)	4.66 (4.52)	11.28 (11.16)	17.59 (17.37)
[Zn(pat)(H_2O)], $C_{17}H_{17}N_3SO_2Zn$	74	258	52.01 (51.99)	4.22 (4.33)	10.81 (10.70)	16.44 (16.66)
[Zn(tat)(H_2O)], $C_{13}H_{14}N_4S_2O_2Zn$	76	220	40.44 (40.27)	3.72 (3.61)	14.44 (14.46)	16.95 (16.88)

The acetyl carbonyl band of the ligand at ≈ 1670 cm^{-1} remained almost unaffected in the spectra of all the complexes, indicating its non-involvement in the bonding with the metal ion. The bands at ≈ 1625 cm^{-1}, due to ν(C=N), shifted to a lower wave number and appeared as a new broad band at ≈ 1600 cm^{-1} in the spectra of all the complexes.[10] The thiazole ν(C=N) of H_2tat was only marginally affected, indicating the non-involvement of the thiazole nitrogen in the coordination. That the intramolecularly hydrogen–bonded O–H/S–H and N–H protons are replaced by the metal ion is confirmed by the disappearance of the broad free ligand band in the region 2500−3500 cm^{-1}. Instead, several medium intensity bands assignable to various aliphatic and aromatic ν(C−H) vibrations appeared in this region. The spectra of all the complexes show additional medium intensity bands in the 420−450 cm^{-1} and 520−550 cm^{-1} regions, presumably due to ν(M–O) and ν(M–N) vibrations.[11] That the complexes contain coordinated water molecule is clearly indicated by the presence of a band at 3500 cm^{-1} in the spectra. Thus, the observed IR spectra strongly suggest that the phenolic O–H/thiol sulphur, the imi-

no nitrogen and the hydrazone nitrogen are involved in coordination with the metal ion. Important bands which appeared in the spectra of the complexes are given in Table IV.

TABLE IV. IR spectral data (cm^{-1}) of the metal complexes of H_2pap, H_2pat and H_2tat

Complex	ν(C=O)	ν(C=N)	ν(C=C)	ν(M–O)	ν(M–N)
[Ni(pap)(H_2O)]	1672	1601	1592, 1585	428, 437	532, 540
[Ni(pat)(H_2O)]	1670	1602	1595, 1590	428, 438	522, 540
[Ni(tat)(H_2O)]	1669	1604, 1610	1592, 1588	422, 442	532, 542
[Cu(pap)(H_2O)]	1675	1603	1592, 1582	422, 440	530, 542
[Cu(pat)(H_2O)]	1668	1598	1594, 1590	420, 438	528, 536
[Cu(tat)(H_2O)]	1668	1601, 1612	1597, 1591	418, 430	528, 546
[Zn(pap)(H_2O)]	1676	1604	1595, 1590	420, 432	522, 535
[Zn(pat)(H_2O)]	1670	1597	1590, 1585	422, 432	530, 540
[Zn(tat)(H_2O)]	1668	1600, 1611	1587, 1582	430, 446	520, 542

^{1}H-NMR spectra. The ^{1}H-NMR spectra of H_2pap, H_2pat and H_2tat show a low field one proton singlet at $\delta = 14$ ppm due to the intramolecularly hydrogen-bonded hydrazone N–H proton.[6,12] The O–H and S–H proton signals are observed at $\delta = 10.8$ ppm and $\delta \approx 6$ ppm, respectively (Table I). The methyl proton signals are observed as two singlets at $\delta \approx 2.3$ (3H) and 2.6 (3H) ppm. The absence of any signal due to the methine proton supports the hydrazone form of the compound. The aryl protons appeared in the δ range 6.8−7.8 ppm as a complex multiplet. In the ^{1}H-NMR spectra of the diamagnetic Ni(II) and Zn(II) complexes, the low field signals due to the N–H and O–H/S–H protons disappeared, indicating that these protons are replaced by the metal ion.[5] The methyl and aryl proton signals are slightly low field shifted and the integrated intensities of these signals agree well with the formulation of the complexes.

Mass spectra. The mass spectra of the compounds show an intense molecular ion peak. Peaks due to the elimination of CH_3CO, ArNH, C_6H_5O/C_6H_5S, C_6H_5/thiazole, *etc*., from the molecular ion are present in the spectra.[5,13] The FAB mass spectra of the Cu(II) complexes showed molecular ion peaks corresponding to [CuL(H_2O)] stoichiometry. Peaks due to the elimination of CH_3CO, ArNH, C_6H_5O/C_6H_5S, *etc*., from P^+ also appeared in the spectra. The spectra of all the chelates contain a number of fragments containing copper in the natural 3:1 abundance of ^{63}Cu and ^{65}Cu isotopes (Table II).

Electronic spectra. The UV spectra of the compounds show two broad bands with maxima at ≈ 380 nm and ≈ 250 nm due to the various n→π* and π→π* transitions. In the complexes, these absorption maxima shifted appreciably to lower wave numbers. The Cu(II) complexes showed a broad visible band, λ_{max} at ≈ 15,000 cm^{-1}. This, together with the measured μ_{eff} values (≈ 1.72 μ_B) suggests square-planar geometry.[14] The observed diamagnetism and broad medium-intensity

band at ≈ 17,600 cm^{-1} in the spectra of the Ni(II) chelates suggest their square-planar geometry.

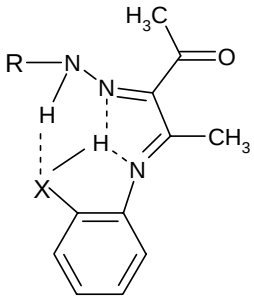

Compound	R	X
H_2pap	Phenyl	O
H_2pat	Phenyl	S
H_2tat	2-Thiazolyl	S

Fig. 1. Structure of H_2pap, H_2pat and H_2tat.

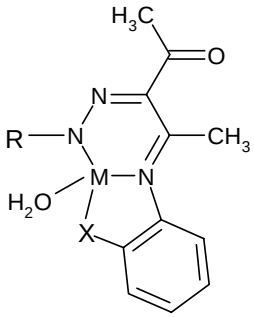

M = Ni(II), Cu(II), Zn(II).

Fig. 2. Structure of metal complexes of H_2pap, H_2pat and H_2tat.

Characterization of H_2tap and its metal complexes

Infrared spectra. That both the carbonyl groups of 3-(2-thiazolylazo)acetylacetone are involved in the Schiff's base condensation with 2-aminophenol is clearly indicated in the IR spectrum of H_2tap. Thus, the spectrum of the compound in the region 1600−1800 cm^{-1} showed no band assignable to a free acetyl carbonyl. However, the spectrum displayed three medium intensity bands at 1605 cm^{-1}, 1615 cm^{-1} and 1625 cm^{-1}, assignable, respectively, to the stretching of the hydrazone C=N, CH_3–C=N and the thiazole ring C=N. The broad band observed in the 2500−3800 cm^{-1} region suggest the involvement of the OH function in strong hydrogen bonding with the C=N group. In the IR spectra of all the complexes, the ν(C=N) bands are shifted appreciably to low wave numbers, indicating the involvement of these groups in bonding with the metal ion. The thiazole ν(C=N) is only marginally affected, indicating the non-involvement of the thiazole nitrogen in coordination. The bending mode of the hydrazone N–H remained almost unaffected in the spectra of complexes, indicating its non-involvement in complexation. The broad free ligand band in the region 2500−3800 cm^{-1} almost vanished in the spectra of complexes and instead several weak and medium intensity bands appeared in this region, assignable to ν(N–H) and various ν(C–H) vi-

brations. That the imino nitrogens and the phenolic oxygens are involved in complexation with the metal ion is clearly evident from the appearance of new medium intensity bands at ≈ 425 cm^{-1} and ≈ 530 cm^{-1}, assignable to ν(M–O) and ν(M–N) in the spectra.[11] Important bands that appeared in the spectra are given in Table V.

^{1}H-NMR spectra. The ^{1}H-NMR spectrum of the compound displayed a slightly broadened, two proton signal at δ = 12.18 ppm and a one proton signal at δ = 13.5 ppm, due to intramolecularly hydrogen bonded phenolic groups and the hydrazone N–H proton, respectively.[5,6] The spectrum of the compound also displayed two three proton signals at δ = 2.35 ppm and δ = 2.58 ppm due to two methyl groups. The aryl proton signals are observed in the δ 6.68−7.90 region. In the ^{1}H-NMR spectra of the diamagnetic Ni(II) and Zn(II) complexes, the signals due to the phenolic proton of the free ligand disappeared, while the hydrazone proton signal remained almost unaltered, indicating that only the phenolic hydrogens are replaced by metal ion and the hydrazone N–H proton remained as such.

Table V. Analytical, IR and ^{1}H-NMR spectral data of H_2tap and its metal complexes

Compound	M.p.	Yield	Found (Calcd.), %				ν / cm^{-1}			δ / ppm		
	°C	%	C	H	N	M	C=N	M–O	M–N	NH	OH	CH_3
H_2tap	125	60	58.74	5.08	18.68	–	1625,	–	–	13.50	12.18	2.35
$C_{18}H_{19}N_5SO_2$			(58.54)	(5.15)	(18.97)		1615,			(1H)	(2H)	(3H),
							1605					2.58
												(3H)
[Ni(tap)]	298	76	50.94	3.92	16.23	13.94	1622	432,	550,	13.46	–	2.33
$C_{18}H_{17}N_5NiSO_2$			(50.74)	(3.99)	(16.44)	(13.79)	1602	420	538	(1H)		(3H),
							1560					2.56
												(3H)
[Cu(tap)]	290	72	50.20	3.85	16.18	14.82	1620	422,	555,	–	–	–
$C_{18}H_{17}CuN_5SO_2$			(50.17)	(3.95)	(16.26)	(14.76)	1600	415	540			
							1565					
[Zn(tap)]	224	68	50.00	3.83	16.14	15.00	1622	428,	545,	13.48	–	2.34
$C_{18}H_{17}N_5SO_2Zn$			(49.96)	(3.93)	(16.19)	(15.12)	1600	418	530	(1H)		(3H),
							1570					2.59
												(3H)

Mass spectra. The formation of the compound is well confirmed from the presence of an intense P^+ peak at *m*/*z* 369 in its mass spectrum. Fragments corresponding to the elimination of C_3H_2NS, $C_3H_3N_2$, $C_3H_3N_3S$ and C_6H_5O from the parent ion were present in the spectrum (Table VI). The mass spectrum of the Cu(II) complex clearly shows the presence of a molecular ion peak. Other important peaks appearing in the spectrum are due to the elimination of thiazole, tz–NH, *etc*., from the molecular ion (Table VI).

TABLE VI. Mass spectral data of H_2tap and its Cu(II) complex

Compound	*m*/*z*
H_2tap	369, 302, 285, 276, 270, 256, 113, 99, 93, 84, 77
[Cu(tap)]	432, 430, 348, 346, 366, 364, 339, 337, 331, 319, 317, 303, 285, 256, 113, 93, 84

Electronic spectra. The UV spectrum of the compound show two broad bands with maxima at 370 nm and 245 nm due to n→π* and π→π* transitions. In the complexes these absorption maxima shifted appreciably to lower wave numbers. The Cu(II) complex showed a broad visible band, λ_{max} at 15,000 cm^{-1}. This, together with the measured μ_{eff} value (1.74 μ_B) suggests square-planar geometry.[14] The observed diamagnetism and broad medium-intensity band at 17,500 cm^{-1} in the spectrum of the Ni(II) chelate suggest its square-planar geometry.

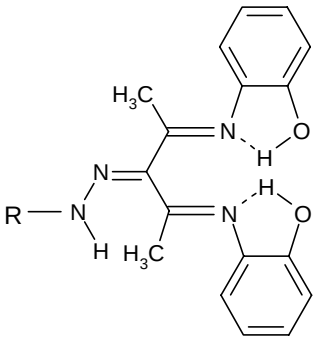

R = 2-Thiazolyl

Fig. 3. Structure of H_2tap.

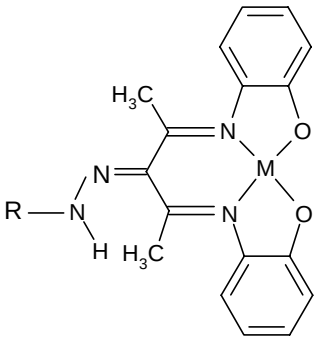

M = Ni(II), Cu(II), Zn(II)

Fig. 4. Structure of the metal complexes of H_2tap.

ESR Spectra. The ESR spectra of the Cu(II) complexes were recorded at 77 K in DMF solution. The spectra gave four well-resolved peaks due to the hyperfine interaction of copper (Table VII), indicating considerable covalent character[15] for the metal–ligand bonds. The observed *A* values indicate that the odd electron density is less on [Cu(tap)] compared to the other three chelates. Hence the delocalization of the metal d-electrons is greater in [Cu(tap)] compared to the other three complexes.

TABLE VII. ESR parameters of the Cu(II) complexes in DMF at 77 K

Complex	$g_{\|}$	$g_{\perp}$	$A_{\|}\times10^{-4}$ / cm^{-1}	$A_{\perp}\times10^{-4}$ / cm^{-1}
[Cu(pap)(H_2O)]	2.172	2.052	210	25
[Cu(pat)(H_2O)]	2.171	2.075	202	26
[Cu(tat)(H_2O)]	2.182	2.068	198	28
[Cu(tap)]	2.160	2.065	183	38

CONCLUSIONS

Four new polydentate Schiff base ligands have been prepared by the condensation of 3-(phenylazo)- and 3-(2-thiazolylazo)-2,4-pentanediones with 2-aminophenol and 2-aminothiophenol. Analytical, IR, ^{1}H-NMR and mass spectral data revealed a 1:2 product (H_2tap) with 3-(2-thiazolylazo)-2,4-pentanedione and 2-aminophenol in which both carbonyl groups of the dione are involved in the Schiff base formation. In all other cases, 1:1 condensation products (H_2pap, H_2pat and H_2tat) are formed. The analytical, physical and spectral data of the [ML] com-

plexes of Ni(II), Cu(II) and Zn(II) showed dibasic tetradentate N_2O_2 coordination involving the azomethine nitrogens and the phenolic oxygens of H_2tap. All the other ligands functioned as dibasic tridentates where the imine and hydrazone nitrogens and the O–H/S–H groups are coordinated in their 1:1 metal chelates.

ИЗВОД

МЕТАЛНИ КОМПЛЕКСИ ШИФОВИХ БАЗА ДОБИЈЕНИ У РЕАКЦИЈИ 3-(АРИЛАЗО)-2,4-ПЕНТАНДИОНА СА 2-АМИНОФЕНОЛОМ И 2-АМИНОТИОФЕНОЛОМ

K. KRISHNANKUTTY[1], P. SAYUDEVI[2] и MUHAMMED BASHEER UMMATHUR[3]

[1]Department of Chemistry, University of Calicut, Kerala–673635, [2]Department of Chemistry, NSS College, Manjeri, Kerala–676122 и [3]Department of Chemistry,Unity Women's College, Manjeri, Kerala–676122, India

Фенилазо- и тиазолилазо-2,4-пентандиони у реакцији са 2-аминофенолом и 2-аминотиофенолом дају нову серију полидентатних лиганда који су Шифове базе. Структура и таутомерна природа ових једињења и њихових комплекса установљена је на основу њихових IR, ^{1}H-NMR и масених спектара. Спектрални и аналитички подаци указују на то да се N_2O_2 тетрадентатни лиганди формирају кондензацијом обе карбонилне групе 3-(2-тиазолилазо)-2,4-пентандиона са 2-аминофенолом. Детаљи око формирања [ML] комплекса ових лиганда са Ni(II), Cu(II) and Zn(II), као и природа везе, дискутовани су на основу аналитичких, IR, ^{1}H-NMR и масених спектралних података.

(Примљено 8. фебруара 2007)

REFERENCES

1. a) K. Sharma, A. Srivastava, S. Srivastava, *J. Serb. Chem. Soc.* **71** (2006) 917; b) V. E. Kuzmin, A. G. Artemenko, R. N. Lozytska, A. S. Fedtchouk, V. P. Lozitsky, E. N. Muratov, A. K. Mescheriakov, *SAR QSAR Environ. Res.* **16** (2005) 219; c) D. Kumar, A. Syamal, A. K. Singh, *Indian J. Chem*. **42A** (2003) 280
2. a) P. D. Benny, J. L. Green, H. P. Engelbrecht, C. L. Barnes, S. S. Jurisson, *Inorg. Chem.* **44** (2005) 2381; b) T. D. Thangadurai, K. Natarajan, *Synth. React. Inorg. Met.-Org. Chem.* **31** (2001) 549
3. K. Venkataraman, *Chemistry of Synthetic Dyes*, Vol. 5, Academic Press, New York, 1977
4. a) H. J. Garg, C. Prakash, *J. Pharm. Sci*. **60** (1971) 323; b) H. J. Garg, C. Prakash, *J. Org. Chem.* **35** (1970) 1056
5. a) K. Krishnankutty, J. Michael, *J. Coord. Chem.* **22** (1991) 327; b) K. Krishnankutty, J. Michael, *J. Coord. Chem.* **24** (1993) 259; c) K. Krishnankutty, J. Michael, *J. Coord. Chem.* **70** (1993) 238
6. a) K. Krishnankutty, P. Ummer, *J. Indian Chem.* Soc. **65** (1988) 213; b) K. Krishnankutty, P. Ummer, *J. Indian Chem.* Soc. **66** (1989) 194; c) N. Thankarajan, K. Krishnankutty, *Indian J. Chem*. **23A** (1984) 401
7. K. Krishnankutty, D. K. Babu, *J. Indian Chem. Soc.* **73** (1996) 379
8. P. Gilli, V. Bertolasi, V. Ferretti, G. Gilli, *J. Am. Chem. Soc.* **122** (2000) 1405
9. L. J. Bellamy, *The Infrared Spectra of Complex Molecules*, Chapman and Hall, London, 1980
10. P. Viswanathamurthi, A. Geetha, R. Karvembu, K. Natarajan, *Indian J. Chem.* **44A1** (2005) 90
11. K. Nakamoto, *Infrared Spectra and Raman Spectra of Inorganic and Coordination Compounds*, Wiley, New York, 1997
12. D. C. Nonhebel, A. Mitchell, *Tetrahedron* **35** (1979) 2013

13. H. Budzikiewicz, C. Djerassi, D. H. Williams, *Mass Spectrometry of Organic Compounds*, Holden Day, San Francisco, 1967
14. K. C. Joshi, V. N. Pathak, *Coord. Chem. Rev.* **22** (1977) 37
15. a) H. R. Gersmann, G. D. Swalen, *J. Chem. Phys.* **36** (1962) 3221; b) A. H. Maki, B. R. Mc Garvey, *J. Chem. Phys.* **29** (1958) 31.

Journal of the Serbian Chemical Society
JSCS@tmf.bg.ac.yu • www.shd.org.yu/JSCS

J. Serb. Chem. Soc. 72 (11) 1085–1094 (2007)
JSCS–3643

UDC 547.835+547.963.32:543.552
Original scientific paper

Linear sweep polarographic determination of nucleic acids using acridine orange as a bioprobe

WEI SUN*, NA ZHAO, XIANLONG YUAN and KUI JIAO

College of Chemistry and Molecular Engineering, Qingdao University of Science and Technology, Qingdao 266042, P. R. China

(Received 7 November 2006, revbised 2 April 2007)

Abstract: The interaction of acridine orange (AO) with double-stranded (ds) DNA in aqueous solution was investigated by linear sweep polarography (LSP) on a dropping mercury working electrode (DME). In pH 2.5 Britton–Robinson (B–R) buffer solution, AO had a sensitive linear sweep polarographic reductive peak at –0.89 V (*vs*. SCE), which could be greatly inhibited by the addition of dsDNA, with a positive shift of the peak potential. Based on the decrease of the reductive peak current, a new quantitative electrochemical determination method for dsDNA was developed with a linear range of 2.0−20.0 mg l^{-1} and the linear regression equation: ΔI_p" (nA) = 111.90 C (mg l^{-1})+125.32 (n = 9, γ = 0.997). The influences of commonly co-existing substances, such as metal ions, amino acid, *etc*., on the determination were also investigated. The method is sensitive, rapid and simple with good selectivity. The new proposed method was further applied to the detection of RNA and three synthetic samples containing dsDNA with satisfactory results. The binding number and the equilibrium constant between dsDNA and AO were calculated by an electrochemical method.

Keywords: acridine orange, nucleic acids, linear sweep polarography, electroanalysis.

INTRODUCTION

The electrochemistry of DNA was first discovered by Paleček *et al*. in the 1960s. DNA can produce redox signals at a mercury electrode and other solid electrodes, such as a metals, carbon and carbon nanotube modified electrodes.[1–3] Some reviews have reported recent progress in the electrochemistry of DNA, electrochemical DNA biosensors, *etc*.[4–7] The signals obtained from the working electrode were related to structural or conformational changes, hybridization and damage of DNA. The interaction of DNA with small molecules can result in the formation of DNA–molecule biocomplexes and have a large influence on the properties of DNA.[8] Many analytical methods, such as spectrophotometry,[9] fluorometry,[10] light scattering,[11] *etc*., were also proposed for the detection of nucleic

* Corresponding author. E-mail: sunwei@qust.edu.cn
doi: 10.2298/JSC0711085S

acids based on the interaction of DNA with organic dyes. Compared with these methods, electrochemical methods have some advantages, such as cheaper and smaller devices, a wider linear range and lower detection limit.[12] The explanation of the mechanism of the interaction of DNA with small molecules can further approach action mechanisms in cells or elucidate the binding process of drugs with DNA. Recently, the interaction of toxic chemicals and drugs with DNA was widely studied by an electrochemical method. Wang *et al*.[13] established an electrochemical equation for examining the interaction of irreversible redox compounds with DNA. The electrochemical behavior of Hoechst 33258 and its interaction with DNA was investigated using cyclic voltammetry and other electrochemical techniques. The results showed that Hoechst 33258 binds tightly to the minor groove of DNA and covers four base pairs. Jiao *et al*. used some organic dyes, such as Toluidine Blue[14] and Malachite Green[15] for the detection of dsDNA based on the formation of electroinactive complexes after the mixture of dsDNA with dye in solution. Bard *et al*. reported the interaction of metal chelates of tris(1,10-phenanthroline)cobalt(III) with DNA in an aqueous medium by cyclic voltammetry and established a redox current equation for the intercalator–DNA complex. The result showed that after the addition of DNA, the change of the voltammetric responses of the reaction solution were caused by changes of the diffusion coefficient of the DNA complex.[16–17] Paleček *et al*. studied the interaction between the anti-cancer drug mitomycin C and DNA by cyclic voltammetry on a hanging mercury drop electrode, which resulted in a decrease of the voltammetric current of the nucleic acid activated mitomycin C and a guanine oxidation signal.[18]

The interactions of the cationic dye acridine orange (AO, molecular structure shown in Fig. 1) with nucleic acids, such as dsDNA and RNA, have been carefully investigated by different methods.[19–21] For example, AO has been used as a sensitive fluorescence probe for DNA. Bi *et al*.[22] studied the interaction of flavonoids, such as quercetin, kaempferide and luteolin, with fish sperm dsDNA using AO as a fluorescence probe to distinguish the variation of spectroscopic characteristics. Cao *et al*.[23] applied the fluorescence energy transfer between AO and safranine T for the determination of DNA. Gherghi *et al*.[24] studied the interaction of AO and ethidium bromide (EB) with DNA in solution by alternating current voltammetry on a hanging mercury drop electrode based on the changes of the direct electrochemical responses of DNA at −1.20 V.

In this study, the linear sweep polarographic method was employed to investigate the interaction of AO with dsDNA. It was found that the addition of dsDNA into AO solution greatly decreased the reductive peak current of AO with a positive shift of the peak potential, which are typical characteristic of the intercalation model of small molecules with DNA. By monitoring the electrochemical behavior of AO before and after the addition of dsDNA, the electrochemical parameters were calculated and compared. The decrease of reductive peak current

was further used to establish a sensitive detection method for microamounts of nucleic acids.

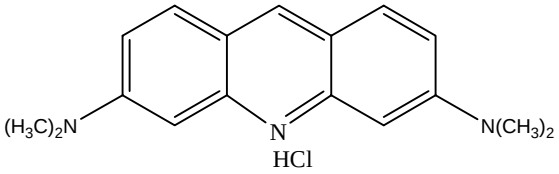

Fig.1. The molecular structure of acridine orange (AO).

EXPERIMENTAL

Instruments

A JP-303 polarographic analyzer (Chengdu Instrumental Factory, China) was used for polarographic detection with a drop mercury electrode (DME) as the working electrode, a saturated calomel electrode (SCE) as the reference electrode and a platinum wire as the auxiliary electrode. A DS model 2004 electrochemical analyzer (Shandong Dongsheng Electronic Instrument, China) was used for the cyclic voltammetric experiments with a DS-991 hanging mercury drop electrode (HMDE) as the working electrode, a saturated calomel reference electrode (SCE) and a platinum wire auxiliary electrode. All the measurements were carried out at a temperature of 25±1 °C, except when otherwise stated. The UV–Vis absorption spectra were recorded on a Cary 50 probe spectrophotometer (Varian, Australia). A pHs-3C pH meter (Shanghai Leici Instrumental Factory, China) was used for pH measurements.

Chemicals

Double-stranded (ds) calf thymus DNA was obtained from Beijing Jinke Biochemical Company and used without further purification. A 1.0 g l^{-1} stock solution of dsDNA was prepared by dissolving the DNA in doubly distilled water and stored at 4 °C. The purity of the dsDNA was determined by the absorbance value of A_{260}/A_{280} = 1.85, which indicated that it was free of protein. The concentration of dsDNA was determined by measuring the absorbance at 260 nm. RNA was obtained from Sinopharm Chemical Reagent Co. Ltd, and the preparation procedure was the same as that of ds DNA. 1.0×10^{-3} mol l^{-1} acridine orange (AO, Shanghai Chemical Reagent Company) was prepared by directly dissolving 0.04380 g AO in water and diluting to 100 ml. A series of 0.2 mol l^{-1} Britton–Robinson (B–R) buffer solution was used to control the acidity of the interaction solution and also used as the supporting electrolyte for the electrochemical measurements. All the employed chemicals were of analytical reagents grade and doubly distilled water was used throughout the experiments.

Procedure

In a 10 ml flask, the interaction solutions were prepared with 2.0 ml pH 2.5 B–R buffer solution, 4.0 ml of 1.0×10^{-4} mol l^{-1} AO solution and different amounts of dsDNA solution. The mixture was shaken homogeneously, stood at 25 °C for 20 min and then subjected to the electrochemical studies. The potential range was selected in the range from −0.7 to –1.0 V and the peak current of AO at −0.89 V (*vs*. SCE) was recorded.

RESULTS AND DISCUSSION

UV–Vis absorption spectra

The UV–Vis absorption spectra of AO and its mixture with dsDNA are shown in Fig. 2, from which it can be seen that AO exhibits an absorption maximum at 495 nm with a shoulder at 488 nm (curve 1). When dsDNA was added into the

AO solution, the absorbance maximum decreased and was red-shifted by about 4 nm (curve 2 and 3). According to Barton,[25] the hypochromism and red shift of the wavelength are typical characteristics of intercalation of small molecules with dsDNA. Hence, the changes of the UV–Vis absorption spectrum of AO in the presence of dsDNA indicate that intercalation had occurred in the mixed solution.

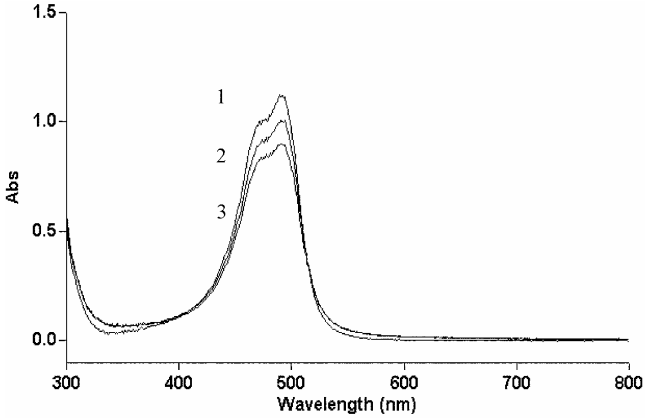

Fig. 2. The UV–Vis absorption spectra of AO and dsDNA in B–R buffer pH 2.5: 1) 4.0×10^{-5} mol l^{-1} AO; 2) 4.0×10^{-5} mol l^{-1} AO + 10.0 mg l^{-1} dsDNA and 3) 4.0×10^{-5} mol l^{-1} AO + 20.0 mg l^{-1} dsDNA.

Cyclic voltammogram of AO and its mixture with dsDNA

The cyclic voltammograms of AO and its mixture with dsDNA are shown in Fig. 3. AO had a reduction peak at −0.89 V (*vs*. SCE) (curve 1) and did not have any oxidation peak in the potential range from –0.7 to –1.0 V. These results indicated that AO participated in an irreversible electrode process on the mercury electrode. After the addition of dsDNA into the AO solution, the peak current decreased and the peak potential moved positively (curve 2), which are typical characteristics of intercalation of small molecules with dsDNA.[12]

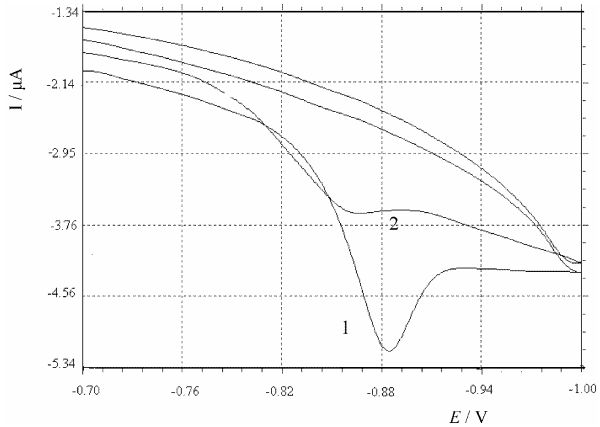

Fig. 3. Cyclic voltammogram of AO in B–R buffer pH 2.5: 1) 4.0×10^{-5} mol l^{-1} AO and 2) 4.0×10^{-5} mol l^{-1} AO + 10.0 mg l^{-1} dsDNA.

The peak current increased with increasing scan rate and the relationship of peak current and scan rate is shown in Fig. 4. Irrespective of the presence of

DNA, a good linear relationship of the peak current *vs*. the square root of scan rate ($v^{1/2}$) was obtained, indicating that the electrode process was completely controlled by the diffusion of the electroactive substances to the surface of the mercury electrode.

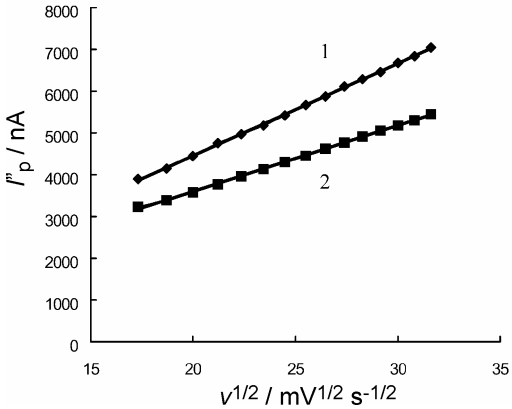

Fig. 4. The dependence of the peak current on the square root of the scan rate. Data taken from Fig. 3.

The electrochemical parameters of the reaction solution before and after the addition of dsDNA were calculated by the following equation for an irreversible electrode process:[12]

$$\ln I_p = -\frac{\alpha nF}{RT}(E_p - E_0) + \ln 0.227nFAk_s c_0^*$$

where α is the electron transfer coefficient, k_s the standard rate constant of the surface reaction, E_0 the formal potential, n the electron transfer number, A the surface area of a mercury drop and c_0^* the concentration of AO.

According to the above equation, αn and k_s can be determined from the slope and the intercept of the linear equation of $\ln I_p$ against (E_p–E_0). E_0 can be determined from the intercept of E_p *vs*. v plot by extrapolating the line to $v = 0$. By this method, the electrochemical parameters were calculated and the results are shown in Table I.

TABLE I. The electrochemical parameters of AO in the absence and in the presence of dsDNA

Parameter	AO	AO–dsDNA
E_0 / V	–0.975	–0.955
αn	0.504	0.253
k_s / s^{-1}	0.357	0.220

Comparing the two groups of the parameters, the values of αn and k_s in the absence and presence of dsDNA show distinct differences; hence the formed AO–dsDNA supramolecular complex was electroactive. In the mixed reaction solution, the diffusion coefficient of AO–dsDNA complex was decreased, which resulted in the decrease of the reduction peak currents.

Measurement of stoichiometry of dsDNA–mAO supramolecular complex

After the method proposed by Li,[26] it was assumed that AO and dsDNA produced a single complex of dsDNA–*m*AO. The binding number (*m*) and the equilibrium constant (β_s) between dsDNA and AO could be determined by the following method:

$$\text{dsDNA} + m\text{AO} \rightarrow \text{dsDNA}–m\text{AO} \quad (1)$$

The equilibrium constant of the reaction, β_s is:

$$\beta_s = \frac{[\text{dsDNA} - m\text{AO}]}{[\text{dsDNA}][\text{AO}]^m} \quad (2)$$

The following equations can be deduced:

$$\Delta I_{max} = kc_{dsDNA} \quad (3)$$

$$\Delta I = k[\text{dsDNA}–m\text{AO}] \quad (4)$$

$$[\text{dsDNA}] + [\text{dsDNA}–m\text{AO}] = c_{dsDNA} \quad (5)$$

Therefore:

$$\Delta I_{max}–\Delta I = k(c_{dsDNA}–[\text{dsDNA}–m\text{AO}]) = k[\text{dsDNA}] \quad (6)$$

Introducing Eqs. (1), (3) and (5) gives:

$$\log [\Delta I/(\Delta I_{max}–\Delta I)] = \log \beta_s + m\log [\text{AO}] \quad (7)$$

where ΔI is the difference between the peak current of the sample and blank, ΔI_{max} corresponds to the maximum value of the difference of the peak currents, c_{dsDNA}, [dsDNA–*m*AO], [dsDNA] corresponds to the total, bound and free concentration of dsDNA in the solution, respectively.

From Eq. (7), the relation of $\log [\Delta I/(\Delta I_{max}–\Delta I)]$ with $\log [\text{AO}]$ was calculated and plotted with the linear regression equation as $\log [\Delta I/(\Delta I_{max}–\Delta I)] = = 1.113\log [\text{AO}]+4.963$ ($n = 7$, $\gamma = 0.995$). From the intercept and the slope, a value of $m = 1$ and $\beta_s = 9.183\times10^4$ were deduced, which indicates that a stable 1:1 complex of dsDNA–AO was formed under the selected conditions.

Second-order derivative linear sweep voltammogram

In order to improve the detection sensitivity, second-order derivative linear sweep polarography was used for nucleic acids and their determination. A typical linear sweep voltammogram of the AO–dsDNA reaction system is shown in Fig. 5. Curve 1 is the voltammogram of B–R buffer, for which no redox response appeared. Curve 2 is the voltammogram of AO in B–R buffer solution and a sensitive linear sweep reduction peak at −0.89 V (*vs*. SCE) appeared, which was due to the electrode reduction of the pyridine group. After the addition of dsDNA into the AO solution, the peak current decreased greatly with a positive shift of the peak potential (curve 3 and 4), which indicates that dsDNA intercalation with AO could lead to decrease in the electrochemical response. With increasing amount

of added dsDNA, the greater was the decrease in the peak current, a fact which could be employed for the determination of dsDNA.

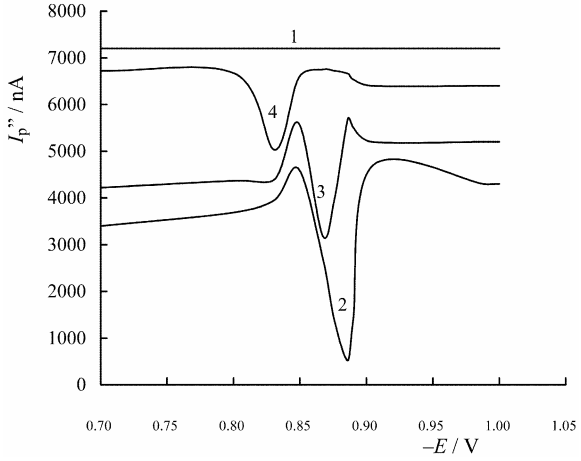

Fig.5. Second order derivative linear sweep voltammogram of 1) B–R buffer pH 2.5; 2) B–R buffer pH 2.5 + + 4.0×10^{-5} mol l^{-1} AO; 3) B–R buffer pH 2.5 + 4.0×10^{-5} mol l^{-1} AO + 10.0 mg l^{-1} dsDNA and 4) B–R buffer pH 2.5 + 4.0×10^{-5} mol l^{-1} AO + 15.0 mg l^{-1} dsDNA.

Optimal of reaction conditions

The influence of pH on the binding reaction was investigated and the results are shown in Fig. 6. The highest value of the difference of peak current was observed at pH 2.5, hence this pH was chosen for the assay. The amount of 0.2 mol l^{-1} B–R was varied and in the volume range 1.0 to 3.0 ml, the peak current remained constant, hence 2.0 ml of B–R buffer solution was selected.

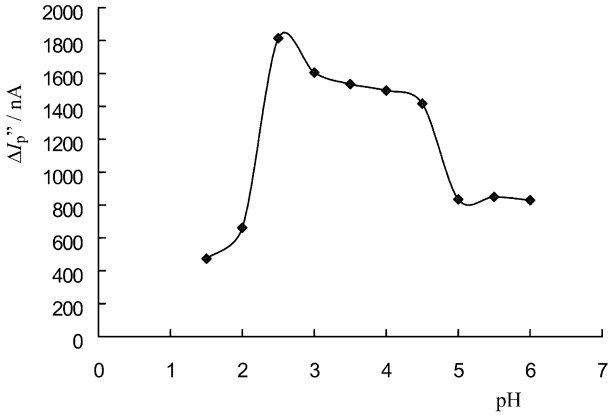

Fig.6. Influence of the pH of the B–R buffer solution on the binding reaction. The solution contained 3.0×10^{-5} mol l^{-1} AO + 10.0 mg l^{-1} dsDNA.

The concentration of AO on the binding reaction was examined by fixing the dsDNA concentration at 10.0 mg l^{-1}. As shown in Fig. 7, the peak current increased with increasing AO concentration and reached maximum at 4.0×10^{-5} mol l^{-1} AO. Hence, an AO concentration of 4.0×10^{-5} mol l^{-1} was used in this experiment.

The binding reaction occurred rapidly at 25 °C and reached equilibrium in about 20 min. The peak current remained constant for about 2 h and showed good stability.

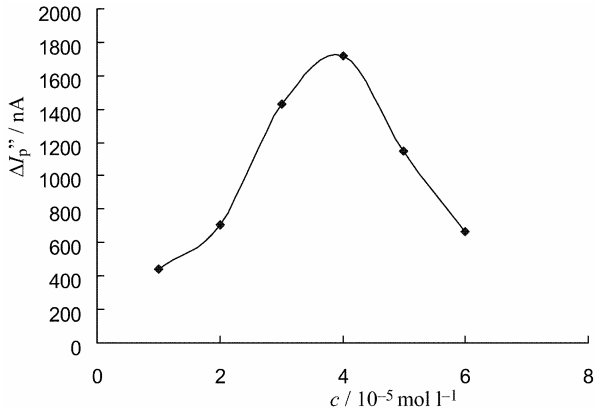

Fig.7. The influence of AO concentration on the current peak in B–R buffer pH 2.5 containing 10.0 mg l^{-1} dsDNA and different concentration of AO.

Optimal of detection conditions

The experimental conditions, such as dropping mercury standing time and the scan rate, on the peak currents were varied. With increasing the mercury drop standing time and the scan rate, the peak current increased correspondingly. The results were recorded at a standing time of 10 s and at a scan rate of 700 mV s^{-1}.

Calibration curves

Under the selected condition, the proposed electrochemical method was applied to the determination of dsDNA and RNA. The decrease of the peak current was proportional to the concentration of the nucleic acids and the analytical results are shown in Table II. It can be seen that this method had good sensitivity and a wide linear range.

TABLE II. Analytical parameters for different nucleic acids

Nucleic acid	Standard regression equation	Linear range mg l^{-1}	Detection limits mg l^{-1}	Regression coefficient (γ)
DNA	ΔI_p" (nA) = 111.90c (mg l^{-1})+125.32	2.0–20.0	0.051	0.997
RNA	ΔI_p" (nA)= 131.84c (mg l^{-1})+88.46	1.0–20.0	0.020	0.998

Influence of interferences

The influence of metal ions, amino acids, detergents, *etc*., on the determination of 10.0 mg l^{-1} dsDNA was investigated and the results are shown in Table III. It can be seen that some metal ions and amino acids interfered with this assay. However, the detergents had a great influence on the determination, which was due to the adsorption of the detergent on the surface of the mercury electrode.

Sample determinations

Three synthetic samples containing dsDNA and different coexisting substances were determined by the proposed method and the results are shown in Table IV. It can be seen that the results are satisfactory with the recovery in the range of 101.5−105.6 %.

TABLE III. Effect of co-existing substances on the determination of 10.0 mg l^{-1} DNA

Co-existing substance	Concentration mg l^{-1}	Relative error %	Co-existing substances	Concentration mol μl^{-1}	Relative error %
L-Arginine	2.0	–1.51	Mg^{2+}	2.0	3.43
L-Leucine	2.0	1.87	Ni^{2+}	2.0	0.72
L-Glutamine	2.0	–4.15	Pb^{2+}	2.0	–0.53
L-Cysteine	2.0	0.74	Cu^{2+}	2.0	1.81
L-Glycine	2.0	–1.87	CATB[a]	2.0	20.23
L-Threonine	2.0	3.00	SDS[b]	2.0	19.26
Citric acid	2.0	–1.70	β-CD[c]	2.0	11.11

[a]Cetyltrimethylammonium bromide; [b]sodiumdodecylsulfate; [c]*β*-cyclodextrin.

TABLE IV. Analytical results of dsDNA in synthetic samples (n = 5)

Sample	Foreign co-existing substances	Added mg l^{-1}	Found mg l^{-1}	Recovery %	*RSD* %
1.	L-Arginine, L-Tyrosine, Ni^{2+}, Zn^{2+}	10.0	10.15	101.5	5.46
2.	L-Arginine, L-Tyrosine, Fe^{3+}, Zn^{2+}	10.0	10.56	105.6	5.02
3.	L-Arginine, Urea, Ni^{2+}, Zn^{2+}	10.0	10.52	105.2	5.11

CONCLUSIONS

In this work the interaction of AO with dsDNA was studied by linear sweep polarography and the electrochemical parameters were calculated and compared. The results indicate that an electroactive complex was formed, which resulted in a decrease of the diffusion coefficient of the complex and a decrease of the reduction peak current. The positive movement of the reduction peak potential of the reaction system indicated that AO can intercalate with dsDNA. Based on the decrease of the peak current, a sensitive electrochemical method was developed for the determination of nucleic acids, such as dsDNA and RNA. The proposed method is sensitive, practicable, reproducible and applicable to the determination of synthetic samples.

Acknowledgements: This research received support from the National Nature Science Foundation of China (20405008, 20635020), the Natural Science Foundation of Qingdao City (04-2-JZ-114) and the Doctoral Foundation of QUST (0022125).

И З В О Д

ОДРЕЂИВАЊЕ НУКЛЕИНСКИХ КИСЕЛИНА ПОМОЋУ АКРИДИН–ОРАНЖ БИО-ПРОБЕ ПОЛАРОГРАФИЈОМ СА ЛИНЕАРНО ПРОМЕНЉИВИМ ПОТЕНЦИЈАЛОМ

WEI SUN, NA ZHAO, XIANLONG YUAN и KUI JIAO

College of Chemistry and Molecular Engineering, Qingdao University of Science and Technology, Qingdao 266042, P. R. China

Испитивана је интеракција акридин–оранжа (АО) и дуплекс-ДНК у воденом раствору, коришћењем поларографије са линеарно променљивим потенцијалом и капљуће живине електроде. У Britton–Robinson пуферском раствору, pH 2,5, АО показује редукциони струјни

врх на –0,89 V (према ЗКЕ) који се додатком дуплекс-ДНК значајно инхибира и помера ка позитивнијим потенцијалима. На основу смањења редукционог струјног врха развијена је нова квантитативна електрохемијска метода одређивања дуплекс-ДНК са опсегом линеарности 2,0–20,0 mg l^{-1} и једначином линеарне регресије: ΔI_p" (nA) = 111,90*C* (mg l^{-1})+125,32 (n = 9, γ = 0,997). Такође је испитиван утицај супстанци које су уобичајени пратиоци (јони метала, амино-киселине) на тачност методе. Метода је осетљива, брза, једноставна и одликује се добром селективношћу. Такође је примењена на детекцију РНК и на три синтетичка узорка који су садржали дуплекс-ДНК и у свим случајевима су резултати били задовољавајући. Електрохемијском методом је израчунат и број молекула АО везаних за дуплекс-ДНК као и одговарајућа константа равнотеже.

(Примљено 7. новембра 2006, ревидирано 2. априла 2007)

REFERENCES

1. E. Paleček, *Nature* **188** (1960) 656
2. D. W. Pang, M. Zhang, Z. L. Wang, *J. Electroanal. Chem*. **403** (1996) 183
3. S. A. M. J. Patricia, J. M. P. T. Arturo, *Anal. Bioanal. Chem.* **378** (2004) 104
4. E. Paleček, M. Fojta, *Anal. Chem.* **73** (2001) 75A
5. W. Joseph, *Electroanalysis* **17** (2005) 7
6. A. Erdem, M. Ozsoz, *Electroanalysis* **14** (2002) 965
7. G. Marrazza, I. Chianella, M. Mascini, *Biosens. Bioelectron.* **14** (1999) 43
8. M. Fojta, *Electroanalysis* **14** (2002) 1449
9. A. P. Abel, M. G. Weller, G. L. Duveneck, M. Ehrant, H. M. Widmer, *Anal. Chem.* **68** (1996) 2905
10. L. Jin, P. Yang, Q. S. Li, *Chem. Res. Chin. Univ.* **17** (1996) 1345
11. Y. F. Li, C. Z. Huang, M. Li, *Anal. Chim. Acta* **452** (2002) 285
12. M. T. Carter, M. Rodriguez, A. J. Bard, *J. Am. Chem. Soc.* **111** (1989) 8901
13. S. F. Wang, T. Z. Peng, F. Y. Catherine, *Electroanalysis* **14** (2002) 1648
14. K. Jiao, Q. J. Li, W. Sun, Z. J. Wang, *Electroanalysis* **17** (2005) 997
15. X. Hu, K. Jiao, W. Sun, J. Y. You, *Electroanalysis* **18** (2006) 613
16. M. T. Carter, A. J. Bard, *J. Am. Chem. Soc.* **109** (1987) 7528
17. R. Marisol, A. J. Bard, *Anal. Chem.* **62** (1990) 2658
18. D. Marin, P. Perez, C. Teijeiro, E. Paleček, *Biophys. Chem.* **75** (1998) 87
19. S. Nafisi, A. A. Saboury, N. Keramat, J. F. Neault, H. A. T. Riahi, *J. Mol. Struct*. **827** (2007) 35
20. X. L. Hou, M. Xu, L. X. Wu, J. C. Shen, *Colloid Surface B.* **41** (2005) 181
21. M. B. Lyles, I. L. Cameron, *Biophys. Chem.* **96** (2002) 53
22. S. Y. Bi, C. Y. Qiao, D. Q. Song, Y. Tian, D. J. Gao, Y. Sun, H. Q. Zhang, *Sensor Actuat. B.* **119** (2006) 199
23. Y. Cao, X. W. He, Z. Gao, L. Peng, *Talanta* **49** (1999) 377
24. I.Ch. Gherghi, S. T. Girousi, A. N. Voulgaropoulos, R. Tzimou–Tsitouridou, *Talanta* **61** (2003) 103
25. E. C. Long, J. K. Barton, *Acc. Chem. Res.* **23** (1990) 271
26. Q. Feng, N. Q. Li, Y. Y. Jiang, *Anal. Chim. Acta* **344** (1997) 97.

Journal of the Serbian Chemical Society
JSCS@tmf.bg.ac.yu • www.shd.org.yu/JSCS

J. Serb. Chem. Soc. 72 (11) 1095–1101 (2007) UDC 546.92'96+547.261+546.33–36:541.138.2
JSCS–3644 *Short communication*

SHORT COMMUNICATION

Kinetic study of methanol oxidation on Pt_2Ru_3/C catalyst in the alkaline media

A. V. TRIPKOVIĆ*#, K. DJ. POPOVIĆ# and J. D. LOVIĆ#

ICTM – Institute of Electrochemistry, University of Belgrade, Njegoševa 12, P.O. Box 473, 11000 Belgrade, Serbia

(Received 20 June, revised 6 August 2007)

Abstract: The electrochemical oxidation of methanol in NaOH solution was examined on a thin film Pt_2Ru_3/C electrode. The XRD pattern revealed that the Pt_2Ru_3 alloy consisted of a solid solution of Ru in Pt and a small amount of Ru or a solid solution of Pt in Ru. It was shown that in alkaline solution, the difference in activity between Pt/C and Pt_2Ru_3/C is significantly smaller than in acid solution. It is proposed that the reaction follows a quasi bifunctional mechanism. The kinetic parameters indicated that the chemical reaction between adsorbed CO_{ad} and OH_{ad} species could be the rate limiting step.

Keywords: platinum–ruthenium alloy, supported nanocatalyst; XRD analysis, methanol oxidation, alkaline solution.

INTRODUCTION

There is a general consensus at present that Pt/Ru offers the most promising results in methanol oxidation in acid solution. The catalytic effect has been observed using different Pt/Ru electrodes, including Pt/Ru alloys,[1–3] electrochemical and spontaneously deposited Ru on Pt[4–6] and carbon supported Pt/Ru.[7–10] When discussing the reason for the catalytic effect of the Pt–Ru surface in the reaction of methanol oxidation, the bifunctional mechanism is often invoked,[11] which suggest the joint activities of both metals. The Pt sites acting as adsorption and dehydrogenation centers produce various adsorbed carbonaceous species and the Ru sites adsorb oxygen-containing species at lower potentials than a pure Pt surface.

The bifunctional mechanism is related to low potentials (E < 0.5 V) and low temperatures (t < 60 °C), since at high potentials Pt dissociates water and at high temperatures Ru adsorbs methanol.[2,12]

There is lack of data dealing with methanol oxidation on PtRu catalyst in alkaline solution[10,13] although from a fundamental viewpoint, the study of the ki-

* Corresponding author. E-mail: amalija@tmf.bg.ac.yu
# Serbian Chemical Society member.
doi: 10.2298/JSC0711095T

netics of methanol oxidation in alkaline solution may provide some new insight into developing new catalysts.

In this work, the kinetics of methanol oxidation on a Pt_2Ru_3/C catalyst in alkaline solution was investigated and compared with a Pt/C catalyst.

EXPERIMENTAL

Electrode preparation

The platinum–ruthenium and platinum electrocatalysts supported on high area carbon (Pt_2Ru_3/C and Pt/C) with 54 wt % alloy and 47.5 wt % Pt (Tanaka Precious Metal Group) were applied to a glassy carbon substrate in the form of a thin film using the procedure described elsewhere.[9] The mass transfer resistance through the Nafion® film was negligible.[10]

Electrode characterization

The electrodes were characterized by X-ray diffraction analysis.

Electrochemical measurements

All electrochemical measurements were conducted at 22 ºC in a thermostated three-compartment electrochemical cell with a Pt spiral as the counter electrode and a saturated calomel electrode (SCE) as the reference electrode. The potentials refer to the reversible hydrogen electrode (RHE). The thin film rotating disk method was used.

All measurements were performed in a nitrogen purged sodium hydroxide solution. Methanol was added to the solution while holding the electrode potential at E = 0.05 V (RHE) for 3 min. The catalytic activity was measured either by recording the potentiodynamic polarization curves (sweep rate 50 mV s^{-1}) or quasi-steady state curves (sweep rate 1 mV s^{-1}).

RESULTS AND DISCUSSION

Electrode characterization

In the diffraction pattern of the Pt_2Ru_3/C catalyst (Fig. 1), two phases were found: a solid solution of ruthenium in platinum (fcc) and a phase associated with an overlapped peak at 43.7° and a weak peak at 58° assigned to the hexagonal phase of ruthenium or a solid solution of platinum in ruthenium (hcp). Pt–Ru fcc reflections in the Pt_2Ru_3/C pattern are systematically shifted towards higher angles in relation to the platinum peaks in the Pt/C pattern due to the incorporation of smaller ruthenium atoms into platinum crystal lattice. It was assumed in the calculations that the second phase is Ru hcp. The two structures, *i.e.*, Pt–Ru fcc and Ru hcp were refined using the Rietveld method. The presence of the carbon support was not taken into account. The crystallite sizes determined with the TOPAS program were 3.9 nm for Pt–Ru fcc and 2.8 nm for Ru hcp. The crystallite size determined using the Scherer method based on the (220) breadth was 3.5 nm for the Pt–Ru fcc phase.

Methanol oxidation on Pt_2Ru_3/C catalyst

The polarization curve for methanol oxidation on Pt_2Ru_3/C in alkaline media and the corresponding basic curve for Pt_2Ru_3/C are presented in Fig. 2.

According to the phase diagram[14] as well as the analysis of the XRD spectra, the Pt_2Ru_3/C catalyst has a complex structure consisting mostly of a solid solu-

tion of Ru in Pt, with a small contribution of pure Ru or a solid solution of Pt in Ru. Consequently, electrochemical characterization by cyclic voltammetry can provide only the general characteristics of the surface structure, such as the hydrogen adsorption/desorption region (0.05 V < E < 0.3 V) followed by the reversible and irreversible formation of oxygen-containing species (RuOH, Ru_2O, $RuO_x \cdot H_2O$)[15,16] at E > 0.3 V. The continuous and fast transition from reversible to irreversible state of oxides results in a broad capacitive feature of a Ru rich alloy such as Pt_2Ru_3.

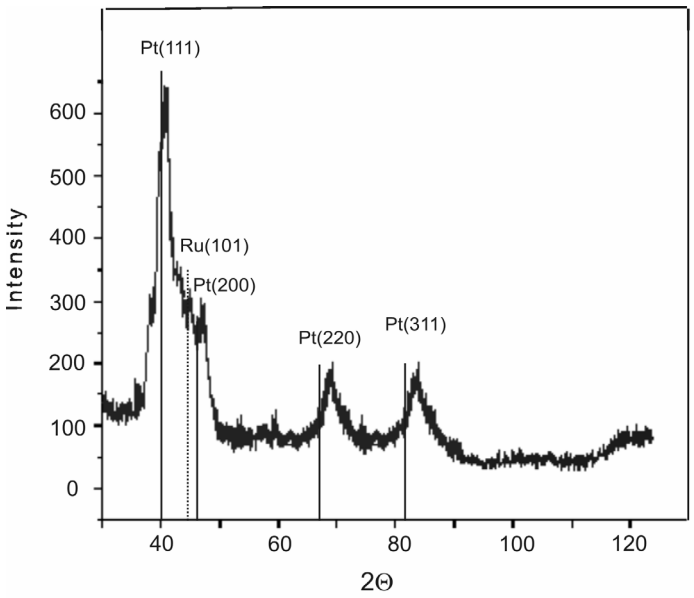

Fig. 1. XRD Pattern of Pt_2Ru_3/C (54 wt. % alloy) catalysts. Vertical lines represent the position of the peaks of pure Pt and pure Ru.

The onset of the methanol oxidation reaction at E_{in} = 0.35 V coincides with the beginning of surface oxidation. The current densities increase with potential up to 0.9 V and then sharply decrease. The current maximum is attained at potentials where the kinetics is optimized by a balance between the rate of methanol dehydrogenation and the rate of oxidation of dehydrogenated products with OH_{ad} species.[10,17] This balance is rapidly disturbed immediately upon reaching the maximum reaction rate, probably due to the fast transformation of the reversible to the irreversible state of oxygenated species.[18,19]

The quasi steady state polarization curve for methanol oxidation on Pt_2Ru_3/C recorded at a slow sweep of 1 mV s^{-1}, shown in Fig. 3, has a Tafel slope of ≈ 120 mV dec^{-1}.

The influence of the methanol concentration was examined in 0.1 M NaOH containing 0.05−1 M methanol. In the entire concentration range, the reaction

rate increases with increasing methanol concentration. The current density at several potentials in the linear Tafel region as a function of the methanol concentration is shown in Fig. 4a. Parallel lines with a slope of about 0.55 imply that methanol oxidation follows half-order kinetics with respect to methanol. The same value was reported for a carbon-supported PtRu catalyst in $HClO_4$[7] as well as for a bulk PtRu catalyst.[12]

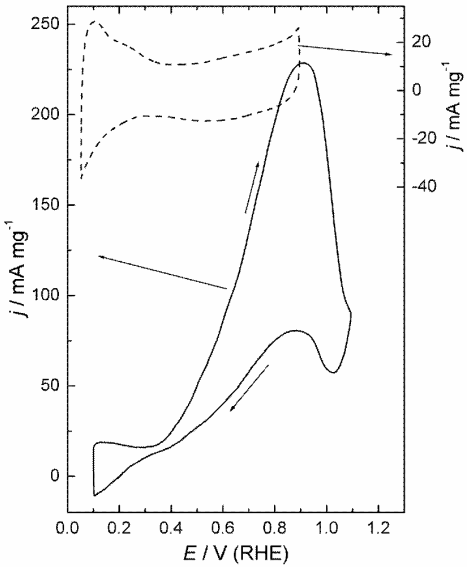

Fig. 2. Cyclic voltammograms for the oxidation of 0.5 M CH_3OH in 0.1 M NaOH at a Pt_2Ru_3/C electrode and the corresponding basic curve. Sweep rate: 50 mV s^{-1}; T = 295 K.

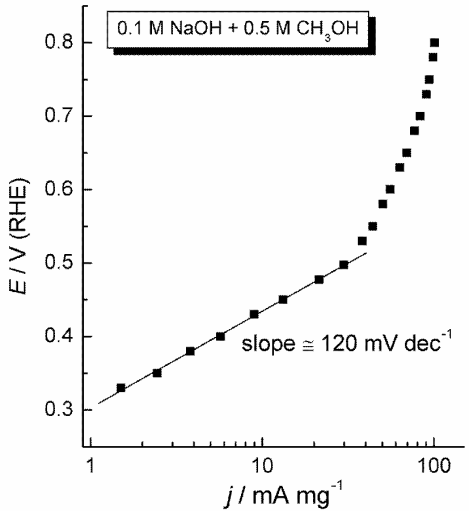

Fig. 3. Tafel plot for the oxidation of 0.5 M CH_3OH at Pt_2Ru_3/C in 0.1 M NaOH solution. Sweep rate: 1 mV s^{-1}; T = 295 K.

The pH dependence of methanol oxidation was investigated in electrolytes containing 0.5 M CH_3OH and 0.05−1 M NaOH. The reaction rate increases with increasing OH^- ion concentration. The estimated reaction order with respect to the OH^- ion is ≈ 0.5 (Fig. 4b).

Comparison of methanol oxidation at Pt_2Ru_3/C andPt/C catalysts and the reaction mechanism

The polarization curves for methanol oxidation at Pt/C and Pt_2Ru_3/C in 0.1 M NaOH recorded at the slow sweep of 1mV s^{-1} are shown in Fig. 5.

Methanol oxidation commences at Pt_2Ru_3/C at less positive potentials compared to Pt/C and proceeds at a higher reaction rate up to ≈ 0.55 V. Pt_2Ru_3/C is more active than Pt/C by a factor of two at E = 0.5 V. At higher potentials Pt/C is more active than Pt_2Ru_3/C, since the oxide covered Ru leads to a decrease of the Pt_2Ru_3/C activity.[13]

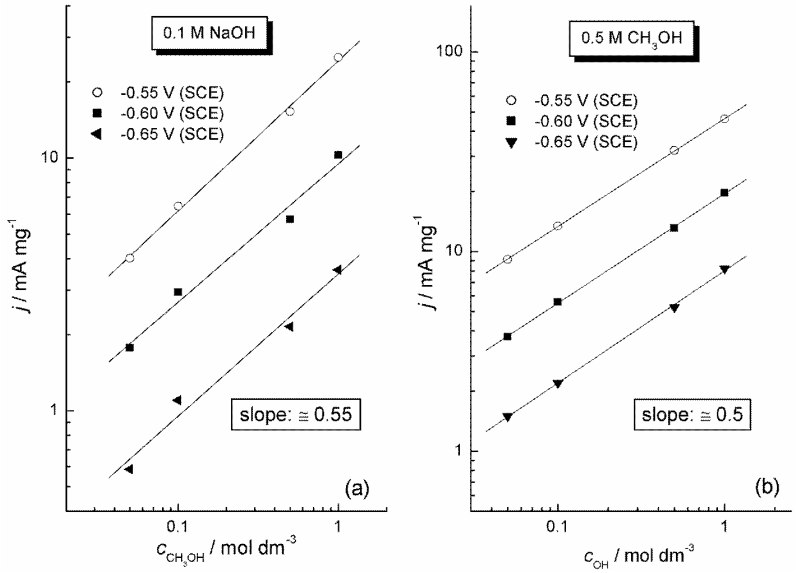

Fig 4. Dependence of the methanol oxidation rate on the CH_3OH and NaOH concentrations at a Pt_2Ru_3/C electrode.

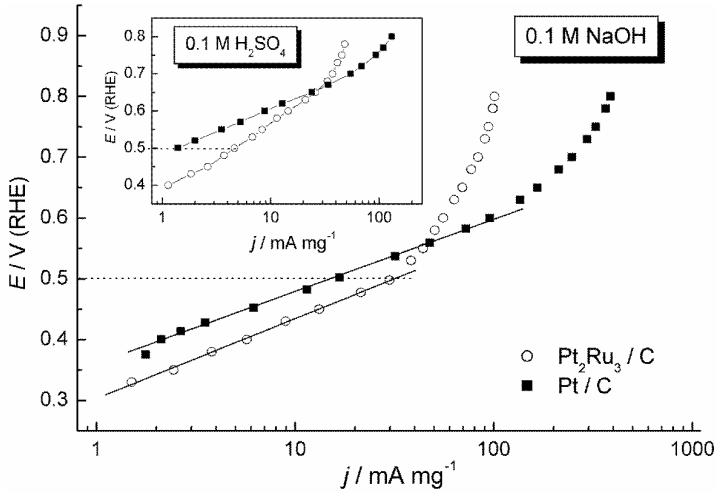

Fig. 5. Tafel plots for the oxidation of 0.5 M CH_3OH at Pt_2Ru_3/C and Pt/C electrodes in 0.1 M NaOH solution. Inset: Tafel plots for the oxidation of 0.5 M CH_3OH at Pt_2Ru_3/C and Pt/C electrodes in 0.1 M H_2SO_4 solution. Sweep rate: 1 mV s^{-1}; T = 295 K.

The enhanced activity of the PtRu catalyst for methanol oxidation compared to Pt can be explained by the bifunctional mechanism as was done in acid solution.[10] However, in alkaline solution, Pt is able to adsorb OH species at almost as low potentials as Ru causing the reaction also on Pt. For this reason the difference in activity between Pt/C and Pt_2Ru_3/C electrodes is smaller in alkaline

than in acid solution, as is shown in Fig. 5. In this sense, it could be concluded that Ru in alkaline media is not the only donor of OH_{ad} species as is the case in acid solution.

In fact, oxidation of methanol in alkaline solution proceeds through a quasi-bifunctional mechanism, summarized as follows:

$$Pt + CH_3OH_{sol} \rightarrow Pt–CH_3OH_{ad} \rightarrow Pt–CO_{ad} + 4H^+ + 4e^- \quad (1)$$

$$Ru + OH^- \rightarrow Ru–OH_{ad} + e^- \quad (2)$$

$$Pt + OH^- \rightarrow Pt–OH_{ad} + e^- \quad (3)$$

$$Pt–CO_{ad} + Ru–OH_{ad} \rightarrow Pt–COOH_{ad} + Ru \quad (4)$$

$$Pt–CO_{ad} + Pt–OH_{ad} \rightarrow Pt–COOH_{ad} + Pt \quad (5)$$

$$Pt–COOH_{ad} + Pt–OH_{ad} \rightarrow 2Pt + CO_2 + H_2O \quad (6)$$

In view of the kinetic parameters obtained by this study of methanol oxidation at Pt_2Ru_3/C, the chemical reaction between adsorbed CO_{ad} and OH_{ad} species is proposed as the rate-limiting step (Eqs. (4) or (5)). The kinetic expression for the rds has the form:

$$j = k_1 \theta_{CO} \theta_{OH} \quad (7)$$

Based on the experimental data (Tafel slope of ≈ 120 mV dec^{-1} and the reaction orders with respect to methanol and OH^- ions of 0.5), the current density of methanol oxidation for the overall reaction can be summarized as:

$$j = nFkc_{CH_3OH}^{0.5} c_{OH^-}^{0.5} \exp\left(\frac{\alpha FE}{RT}\right) \quad (8)$$

assuming that the adsorption of methanol and OH species obey Temkin isotherm.

Acknowledgement: This work was financially supported by the Ministry of Science of the Republic of Serbia, Contract No. H-142056.

И З В О Д

КИНЕТИКА ОКСИДАЦИЈЕ МЕТАНОЛА НА Pt_2Ru_3/C КАТАЛИЗАТОРУ У АЛКАЛНОЈ СРЕДИНИ

А. В. ТРИПКОВИЋ, К. Ђ. ПОПОВИЋ и Ј. Д. ЛОВИЋ

ИХТМ – Центар за електрохемију, Универзитет у Београду, Његошева 12, п. пр. 473, 11000 Београд

Електрохемијска оксидација метанола испитивана је на нанокатализатору Pt_2Ru_3 диспергованом на активном угљу као носачу у алкалној средини. Катализатор је карактерисан дифракцијом X-зрака (XRD) и добијени резултати су показали да се легура Pt_2Ru_3 састоји од две фазе: чврстог раствора Ru у Pt и од малих количина чистог Ru или чврстог раствора Pt у Ru. Поређењем активности Pt/C и Pt_2Ru_3/C катализатора у оксидацији метанола у алкалној средини, показано је да је та разлика знатно мања него у киселој средини. Предложен је квази-бифункционални механизам реакције. Добијени кинетички параметри указују на то да је хемијска реакција између адсорбованих CO_{ad} и OH_{ad} честица спори ступањ у оксидацији метанола на Pt_2Ru_3/C катализатору у алкалној средини.

(Примљено 20. јуна, ревидирано 6. августа 2007)

REFERENCES

1. N. M. Marković, H. A.Gasteiger, P. N. Ross, X. Jiang, I. Villegas. M. J. Weaver, *Electrochim. Acta* **40** (1995) 91
2. D. Kardash, C. Korzeniewski, N. Marković, *J. Electroanal. Chem.* **500** (2001) 518
3. A. Kabbibi, R. Faure, R. Durand, B. Beden, F. Hahn, J. M. Leger, C. Lamy, *J. Electroanal. Chem.* **444** (1998) 41
4. T. Frelnik, W. Visscher, A. P. Cox, J. A. R. van Veen, *Electrochim. Acta* **40** (1995) 1537
5. Y. Morimoto, E. B. Yeager, *J. Electroanal. Chem.* **444** (1998) 95
6. W. Chrzanowski, H. Kim, A. Wieckowski, *Catal. Lett.* **50** (1998) 69
7. S. Lj. Gojković, T. R. Vidaković, D. R. Đurović, *Electrochim. Acta* **48** (2003) 3607
8. A. S. Arico, A. K. Shukla, K. M. El-Khatib, P. Creti, V. Antonucci, *J. Appl. Electrochem.* **29** (1999) 671
9. T.J.Schmidt, H.A.Gasteiger, R.J.Behm, *Electrochem. Comm*. **1** (1999) 1
10. A. V. Tripković, K. Dj. Popović, B. N. Grgur, B. Blizanac, P. N. Ross, N. M. Marković, *Electrocim. Acta* **47** (2002) 3707
11. M. Watanabe, S. Motoo, *J. Electroanal. Chem.* **60** (1975) 267
12. H. A. Gasteiger, N. Marković, P. N. Ross Jr., E. J. Cairns, *J. Electrochem. Soc.* **141** (1994) 1795
13. A. V. Tripković, S. Štrbac, K. Dj. Popović, *Electrochem. Comm.* **5** (2003) 484
14. V. Radmilović, H. A. Gasteiger, P. N. Ross Jr., *J. Catal.* **154** (1995) 98
15. A. H. C. Sirk, J. M. Hill, S. K. Y. Kung, V. I. Birss, *J. Phys. Chem. B* **108** (2004) 689
16. G. Wu, L. Li, B.–Q. Xu, *Electrochim. Acta* **50** (2004) 1
17. A. V. Tripković, K. Dj. Popović, J. D. Lović, V. M. Jovanović, A. Kowal, *J. Electroanal. Chem.* **572** (2004) 119
18. A. V. Tripković, K. Dj. Popović, J. D. Lović, *Electrochim. Acta* **46** (2001) 3163
19. A. V. Tripković, S. Lj. Gojković, K. Dj. Popović, **J**. D. Lović, *J. Serb. Chem. Soc.* **71** (2006) 1333.

Journal of the Serbian Chemical Society
JSCS@tmf.bg.ac.yu • www.shd.org.yu/JSCS

J. Serb. Chem. Soc. 72 (11) 1103–1113 (2007)
JSCS–3645

UDC 66.021.3:62–218+54–138:54–72
Original scientific paper

Wall-to-liquid mass transfer in fluidized beds and vertical transport of inert particles

NEVENKA BOŠKOVIĆ–VRAGOLOVIĆ[1]*, RADMILA GARIĆ–GRULOVIĆ[2] and ŽELJKO GRBAVČIĆ[1]

[1]*Faculty of Technology and Metallurgy, Department of Chemical Engineering, University of Belgrade, Karnegijeva 4, 11000 Belgrade and* [2]*Institute for Chemistry, Technology and Metallurgy, Njegoševa 12 11000 Belgrade, Serbia*

(Received 23 February, revised 1 June 2007)

Abstract: Mass transfer coefficients in single phase flow, liquid fluidized beds and vertical hydraulic transport of spherical inert particles were studied experimentally using 40 mm and 25.4 mm diameter columns. The mass transfer data were obtained by studying the transfer of benzoic acid from a tube segment to water using the dissolution method. In all runs, the mass transfer rates were determined in the presence of spherical glass particles 1.2, 1.94 and 2.98 mm in diameter. The influence of different parameters, such as liquid velocity, particles size and voids on mass transfer in fluidized beds and hydraulic transport are presented. The data for mass transfer in all the investigated systems are shown using the Sherwood number (*Sh*) and mass transfer factor – Colburn factor (j_D) – as a function of Reynolds number (*Re*) for the particles and for the column. The data for mass transfer in particulate fluidized beds and for vertical hydraulic transport of spherical particles were correlated by treating the flowing fluid–particle mixture as a pseudo fluid by introducing a modified mixture Reynolds number (Re_m). A new correlation for the mass transfer factor in fluidized beds and in vertical hydraulic transport is proposed.

Keywords: mass transfer, fluidized bed, vertical transport, pseudofluid.

INTRODUCTION

Research of mass transfer in liquid–solid systems is very important for equipment design for many applications. Due to industrial use, especially following the fast development of bioprocesses and water cleaning processes, a better knowledge of these systems becomes increasing important. An industrial application of liquid–solid systems requires the determination of transfer characteristics, especially mass transfer. Mass transfer in fluidized beds has been widely investigated in terms of particle–fluid mass transfer by dissolution, by electrochemical and by ion-exchange methods.[1–7] Some of the results of mass transfer in fluidi-

* Corresponding author. E-mail: nevenka@tmf.bg.ac.yu
doi: 10.2298/JSC0711103B

zed beds have been obtained as the transfer between an immersed surface and the liquid.[8,9] Wall-to-bed mass transfer has been intensively studied for several years because of its theoretical and practical importance.[10,11] In contrast to fluidized beds data, there are no published data on mass transfer in vertical and horizontal hydrotransport of particles.

This paper presents the experimental data for wall-to-liquid mass transfer in coarse particle–liquid systems: fluidized beds and vertical transport. A correlation for the mass transfer coefficient was developed on the bases of the Colburn j_D factor.

EXPERIMENTAL

The rates of mass transfer between a fluid and the wall in fluidized beds and vertical transport of spherical inert particles were studied. A schematic diagram of the experimental systems is shown in Fig. 1.

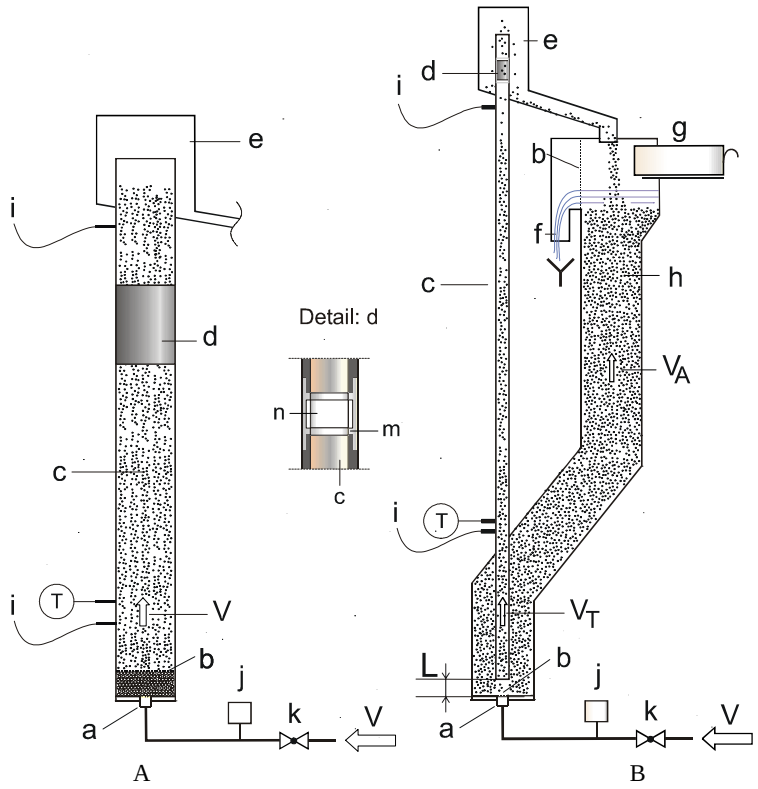

Fig. 1. Schematic diagram of the experimental system: A) fluidization setup; B) vertical transport setup (a – inlet nozzle, 20 mm ID; b – screen; c – fluidizing column 40 mm ID, transport tube 25.4 mm ID; d – segment prepared with benzoic acid; e – overflow; f – water overflow; g – box for water and particle flowrate measurements; h – modified spouted bed 70×70 mm^2 in cross-section; i – pressure taps; j – rotameter; k – valve; L – distance of 20 mm; T – thermocouple; V – inlet flowrate; V_T – tube flow; V_A – annular flow. Detail d: m – segment, n –melt of benzoic acid).

The experiments were conducted using 40 mm (fluidized beds, Fig. 1A) and 25 mm (fluidized beds and vertical transport, Fig. 1B) diameter columns. The fluidizing and transporting fluid was water. The experiments were conducted using inert glass spheres 1.20, 1.94 and 2.98 mm in diameter. The relevant properties of the fluid and particles are summarized in Table I.

TABLE I. Particle and fluid characteristics

Particles (glass spheres)				
d_p / mm	ρ_p / kg m^{-3}	ε_{mf}	U_{mf} / m s^{-1}	U_t / m s^{-1}[14]
1.2	2641	0.39	0.013	0.19
1.94	2507	0.42	0.026	0.29
2.98	2509	0.46	0.044	0.37
Fluid (water at 25 °C)				
ρ_f / kg m^{-3}	μ / Pa s	D / m^2 s^{-1}	c^* / kg m^{-3}	Sc
977	0.893×10^{-3}	9.24×10^{-10}	3.3554	969

In the vertical transport experiments, the fluid and particle flowrates were measured using a specially designed box (g), which allows all of the flow (fluid and particles) to be collected, separated and weighed (Fig. 1B). Normally, the particles recirculate and the suspension overflows at (e), while water overflows at (f). When the fluid and particle flowrates were to be measured, the box (g) was moved to the left to collect the entire flow for a short period of time (10 s to 1 min). The water was then separated from the particles. The particles were dried and weighed and the volume of water was recorded.

The range of experimental conditions is summarized in Table II.

TABLE II. Range of experimental conditions

d_p / mm	1.2	1.94	2.98
U/U_{mf} (Fluidized beds)	1.66–6.67	1.56–4.54	1.45–3.2
ε (Fluidized beds)	0.49–0.83	0.48–0.72	0.53–0.71
U/U_t (Transport)	0.475–4.904	0.405–4.724	0.267–3.884
W_p / kg m^{-2} s^{-1}	9.7–218.8	15.2–318.6	2.5–372.4
G_p/G_f	0.108–0.253	0.113–0.474	0.026–0.331
ε (Transport)	0.827–0.923	0.729–0.897	0.712–0.864

The dissolution of benzoic acid from a tube segment was followed. The tube segment was coated with benzoic acid by immersing an empty ring on a wire support into molten benzoic acid. By repeating the procedure, a compact layer of benzoic acid was formed on the ring segment of the column. The mass transfer coefficient was calculated from the equation:

$$k_c = \frac{\Delta m}{A\, t\, \Delta c} = \frac{\Delta m}{(D_c \pi\, h)\, t\, \Delta c} \tag{1}$$

The transferred mass, Δm, was determined by measuring the weight loss of benzoic acid. The mass transfer area A was calculated from the mean value of the diameter of the tube segment before and after dissolution. Since the weight loss of benzoic acid Δm is small, the bulk concentration was negligible; hence the equilibrium concentration c^* was taken as a driving force Δc.

The benzoic acid solubility and diffusivity were taken from the literature.[12,13] In each run, the average fluid temperature was recorded and the corresponding values of the diffusion coefficients, fluid viscosity, fluid density and equilibrium solubility were considered in the calculations.

RESULTS AND DISCUSSION

The relationships between the particle Sherwood number and the particle Reynolds number for different particle diameters in fluidized beds and vertical transport are presented in Fig. 2. From this Figure, the influence of liquid velocity on mass transfer can be seen. The data are separated into three groups with the particle diameter as the critical parameter. The experimental results show that with increasing liquid velocity (or Reynolds number), the mass transfer coefficient (or Sherwood number) slightly decreases in fluidized beds.

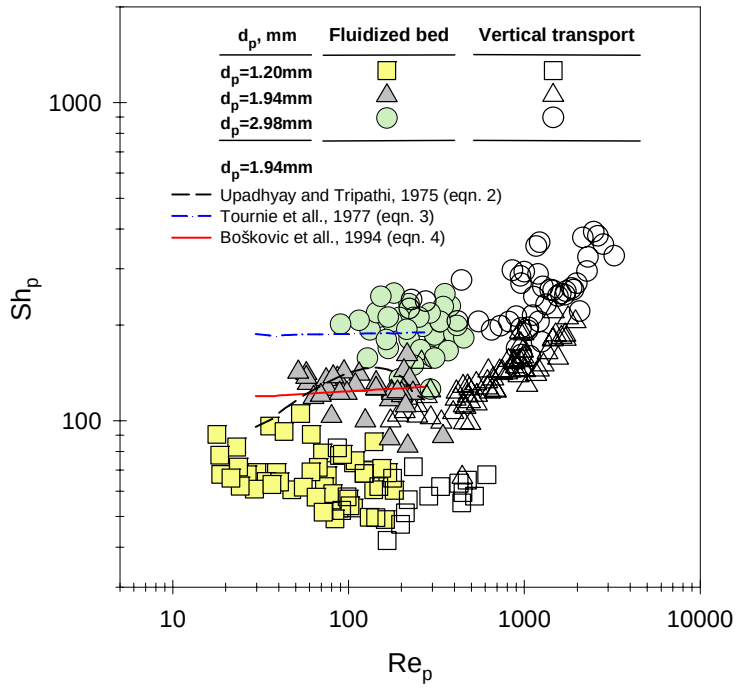

Fig. 2. The relationship between the Sherwood number and Reynolds number for the particles.

The influence of liquid velocity in fluidized beds is connected with the influence of the bed concentration (bed voidage). There are two modes of influence: increasing the liquid velocity increases the mass transfer, but increasing the liquid velocity decreases the particle concentration. Increasing velocity and concentration have a positive influence on mass transfer. Due to both effects, the diffusion boundary layer becomes thinner and mass transfer increases. Finally, as can be seen in Fig. 2, the influence of particle concentration is slightly greater than the influence of liquid velocity.

With increasing liquid velocity, the Sherwood number or mass transfer coefficient is constant for low transport velocities, but for higher transport velocities, the mass transfer increases. This implies that because of the low particle concen-

tration in a transport column, the influence of particles on the diffusivity boundary layer is smaller.

Comparison of the data for fluidized bed (d_p = 1.94 mm) with several literature correlations[9,15,16] show significant difference between our data and the available correlations. As shown, there are significant differences among the systems investigated. Upadhyay and Tripathi[15] proposed the following correlation for mass transfer in packed and fluidized beds (Fig. 2):

$$Sh_p = 1.6218 Re''^{0.5553} Sc^{1/3} \text{ for } Re'' > 20 \quad (2)$$

where $Re'' = Re_p/(1-\varepsilon)$, in the following range of variables: $0.01 < Re'' < 12000$, $572 < Sc < 70000$ and $0.268 < \varepsilon < 0.9653$. The data calculated using Eq. (2) show a maximum which was not confirmed by our experimental data.

Also, Tournie *et al.*[16] gave the following correlation for mass transfer particle–fluid in a fluidized bed:

$$Sh_p = 0.253 Re_p^{0.004} Ga^{0.319} Mv^{0.299} Sc^{0.4} \quad (3)$$

where $Mv = (\rho_p - \rho_f)/\rho_f$. Eq. (3) is recommended in the following range of variables: $1.6 < Re_p < 1320$, $2470 < Ga < 442106$, $0.27 < Mv < 1.14$, $305 < Sc < 1595$ (also shown in Fig. 2). The data show significant difference between this correlation and our experimental values.

Mass transfers in a liquid fluidized bed, were correlated by Bošković *et al.*, by the Equation:[9]

$$Sh_p = 0.261 Re_p^{0.03} Ga^{0.324} Sc^{1/3} \quad (4)$$

in the following range of variables: Re_p = 15−400, Sc = 1361−1932. The predicted values using correlation (4) for mass transfer between fluid and an immersed sphere in fluidized beds of spherical inert particles are in good agreement with the experimental data.

The influence of particle diameter on mass transfer can be seen in Fig. 3, which presents data for the Sherwood number as a function of the Reynolds number for the column in fluidized beds and vertical transport. The data for mass transfer for single phase flow are shown in the same plot for comparison. As can be seen, there is no influence of particle diameter on mass transfer in systems with particles. The presence of particles improves mass transfer for lower fluid velocities, *i.e.*, Reynolds number, when the particle concentration in the flowing mixture is generally higher. A decrease in the liquid velocity ($Re < 10000$), increases the mass transfer for fluidized bed relative to the values in single phase flow by a factor of about 10. For higher Reynolds number (approximately $Re > 10000$), there is no significant difference in mass transfer between single phase flow and hydraulic transport. For a high liquid velocity, the concentration of particles is small and their influence on the mass transfer coefficient is negligible.

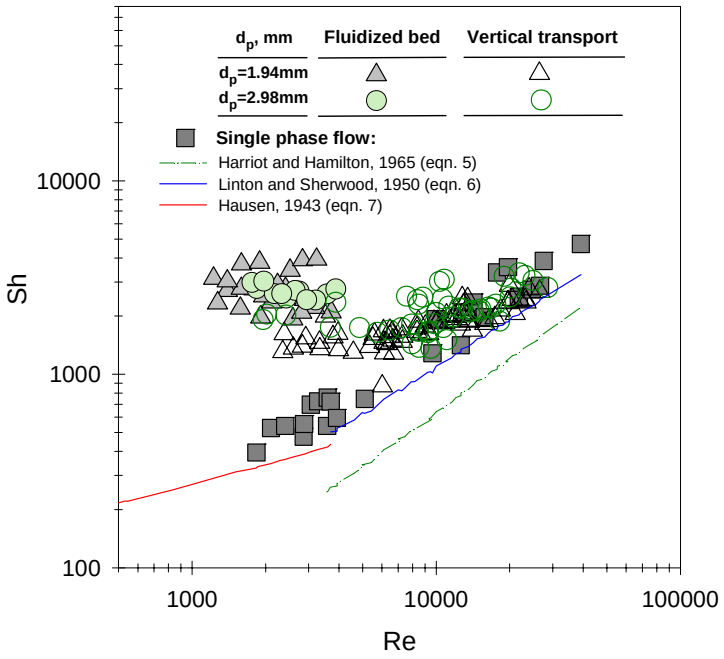

Fig. 3. The relationship between the Sherwood number and Reynolds number for the column.

A comparison of several literature correlations[17–19] of mass transfer for single phase flow are shown in Fig. 3.

The Harriot and Hamilton[17] Equation for a wide range of values of Reynolds and Schmidt numbers ($2000 < Re < 70000$ and $1000 < Sc < 2260$),

$$Sh = 0.0096 Re^{0.913} Sc^{0.346} \tag{5}$$

indicates the adverse ratio $L_{t,A}/D_t$, give a value of 0.73 in the present investigation. The predicted values from correlation (5) and the present experimental data show a significant difference.

For specific systems (concentration boundary layer is not formed, small ratio $L_{t,A}/D_t$), the Equation is:[18]

$$Sh = 0.023 Re^{0.8} Sc^{1/3} \left(1 + \left(\frac{D_t}{L_{t,A}} \right)^{0.7} \right) \tag{6}$$

The Linton and Sherwood, Eq. (6), for turbulent flow ($Re > 10000$), gives better results than Eq. (5).

An Equation for the average heat transfer coefficient for the entrance region and the latter part of the tube in laminar flow was proposed by Hausen,[19] which when applied to mass transfer is:

$$Sh_{\text{lam}} = 3.66 + \frac{0.0668 ReSc\left(\frac{D_t}{L_{t,A}}\right)}{1 + 0.4\left(ReSc\left(\frac{D_t}{L_{t,A}}\right)^{1/2}\right)^{2/3}} \left(\frac{\mu}{\mu_{\text{zid}}}\right)^{0.14} \tag{7}$$

The data calculated using Eq. (7) are in good agreement with the experimental data.

The experimental data of wall-to-liquid mass transfer in fluidized beds and hydraulic transport are presented using the Colburn mass transfer factor j_D. The mass transfer factor as a function of Reynolds number for particles is shown in Fig. 4 and as a function of Reynolds number for the column in Fig. 5. From the definition of the mass transfer factor:

$$j_D = \frac{Sh}{Re\, Sc^{1/3}} = \frac{k_c}{U} Sc^{2/3} \tag{8}$$

and the previous conclusions from Figs. 4 and 5, it is clearly seen that with the increasing fluid velocity, the mass transfer factor decreases. The same trend is observed for $Re > 10000$.

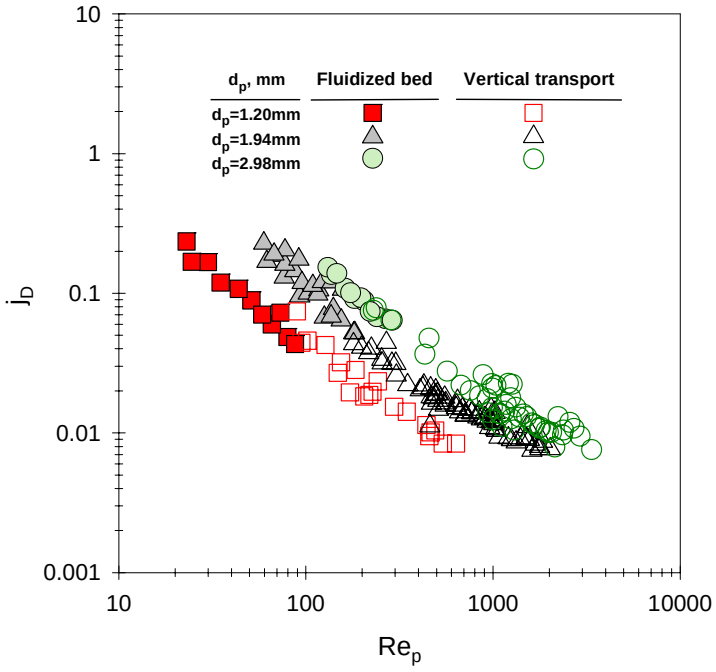

Fig. 4. Variation of the mass transfer factor with Reynolds number for the particles.

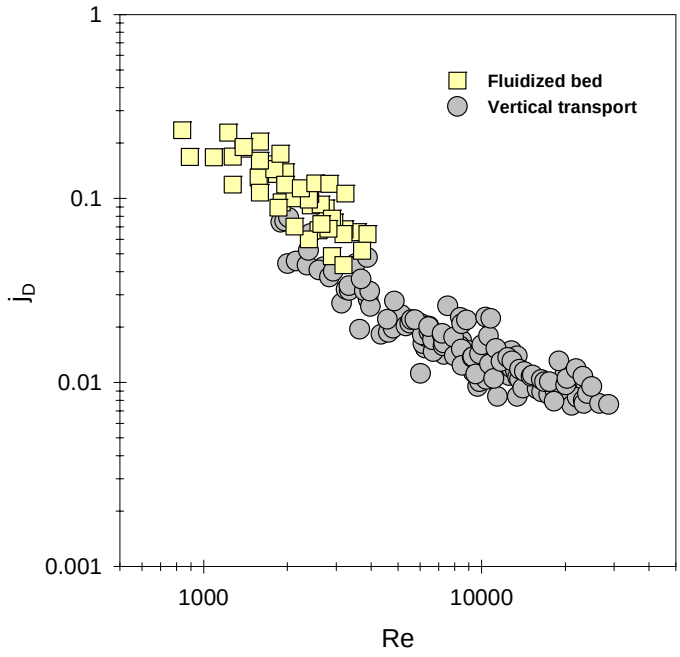

Fig. 5. Variation of the mass transfer factor with Reynolds number for the column.

As can be seen in Fig. 5, there is a significant difference between the experimental data for mass transfer in fluidized beds and vertical transport. As a result of this, the whole system was treated as a pseudo fluid or suspension with a mean density:

$$\rho_{\mathrm{m}} = \varepsilon\,\rho_{\mathrm{f}} + (1-\varepsilon)\,\rho_{\mathrm{p}} \tag{9}$$

An effective mixture viscosity:[20]

$$\mu_{\mathrm{m}} = \mu \exp\left(\frac{5(1-\varepsilon)}{3\varepsilon}\right) \tag{10}$$

and a mean mixture superficial velocity:

$$U_{\mathrm{m}} = \frac{G_{\mathrm{f}}}{\rho_{\mathrm{f}} A_{\mathrm{t}}} + \frac{G_{\mathrm{p}}}{\rho_{\mathrm{p}} A_{\mathrm{t}}} \tag{11}$$

For the suspension mixture, the Reynolds number is:

$$Re_{\mathrm{m}} = \frac{U_{\mathrm{m}} D_{\mathrm{c}} \rho_{\mathrm{m}}}{\mu_{\mathrm{m}}} \tag{12}$$

Also, the fluidized bed and the vertical transport data overlap for $2000 \le Re_{\mathrm{p}} \le 4000$ because the concentrations of the particles in these systems are nearly the same.

The results of the mass transfer factor as a function of the Reynolds number of the mixture are presented in Fig. 6. There is a unique correlation for the mass

transfer data for fluidized beds and vertical transport. These data are correlated by the Equation:

$$j_D = 45\,Re_{\mathrm{m}}^{-0.88} \tag{13}$$

with an absolute deviation of 15.7 % and a relative deviation of –2.0 %.

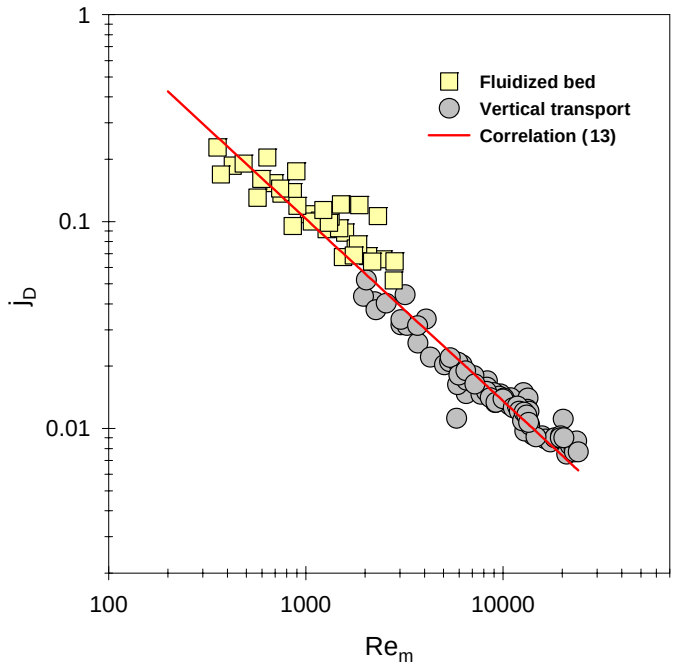

Fig. 6. Correlation between the mass transfer factor and the Reynolds number of the mixture.

CONCLUSIONS

Experiments were performed to determine the mass transfer coefficient between the fluid and the wall in liquid fluidized beds and vertical transport of inert particles. These experiments showed the following:

− With increasing liquid velocity, the mass transfer coefficient slightly decreases in fluidized beds. In vertical transport, the mass transfer coefficient is constant for low velocities and increases for higher velocities.

− The wall-to-liquid mass transfer in fluidized beds and in hydraulic transport is higher than in single phase flow for Reynolds number of the column lower than 10000. For higher Reynolds numbers, there is no significant difference between single phase flow and hydraulic transport.

− The mass transfer factor as a function of Reynolds number is independent of the particle size in fluidized beds and vertical transport.

− A new correlation for the mass transfer factor in particulate fluidized beds and vertical hydraulic transport is proposed.

NOMENCLATURE

A	Mass transfer area, m^2
c^*	Equilibrium concentration, kg m^{-3}
Δc	Concentration difference (driving force), kg m^{-3}
D	Molecular diffusion coefficient, m^2 s^{-1}
D_c	Column diameter, m
d_p	Particle diameter, m
G_f	Fluid mass flowrate, kg s^{-1}
G_p	Particle mass flowrate, kg s^{-1}
h	High of tube segment, m
j_D	Mass transfer factor, $(k_c/U)Sc^{2/3}$
k_c	Mass transfer coefficient, m s^{-1}
Δm	Total mass transferred, kg
Re	Reynolds number for column, $UD_c\rho_f/\mu$
Re_m	Mixture Reynolds number, $U_m D_c \rho_m/\mu_m$
Re_p	Reynolds number for particles, $Ud_p\rho_f/\mu$
Sc	Schmidt number, $\mu/\rho_f D$
Sh	Sherwood number for column, $k_c D_c/D$
Sh_p	Sherwood number for particles, $k_c d_p/D$
t	Exposure time, s
U	Superficial fluid velocity, m s^{-1}
U_t	Terminal velocity, m s^{-1}
U_m	Superficial fluid mixture velocity, m s^{-1}
U_{mf}	Minimum fluidization velocity, m s^{-1}
W_p	Particle mass flux, kg m^{-2} s^{-1}

Greek letters

ε	Voidage
ε_{mf}	Voidage at minimum fluidization
μ	Viscosity of the fluid, Pa s
μ_m	Viscosity of the fluid-particle mixture, Pa s
ρ_f	Fluid density, kg m^{-3}
ρ_p	Particle density, kg m^{-3}
ρ_m	Mean mixture density, kg m^{-3}

И З В О Д

ПРЕНОС МАСЕ ЗИД–ФЛУИД У ФЛУИДИЗОВАНИМ СЛОЈЕВИМА И ПРИ ВЕРТИКАЛНОМ ТРАНСПОРТУ ИНЕРТНИХ ЧЕСТИЦА

НЕВЕНКА БОШКОВИЋ–ВРАГОЛОВИЋ[1], РАДМИЛА ГАРИЋ–ГРУЛОВИЋ[2] и ЖЕЉКО ГРБАВЧИЋ[1]

[1]Технолошко–металуршки факултет, Катедра за хемијско инжењерство, Универзитет у Београду, Карнегијева 4, 11000 Београд и [2]Институт за хемију, технологију и металургију, Његошева 12, 11000 Београд

У овом раду је експериментално испитиван прелаз масе између зида и флуида при струјању флуида кроз колону и у присуству флуидизованих сферних инертних честица и честица у транспорту. За одређивање коефицијента прелаза масе коришћена је метода праћења растварања слабо растворне супстанце – бензоеве киселине – са дела зида колоне у води. Коришћене су колоне пречника 40 mm и 25,4 mm, а као инертне честице коришћене су стак-

лене сфере пречника 1,2; 1,94 и 2,98 mm. Приказани су утицаји различитих параметара као што су брзина флуида, величина честица и порозност слоја на коефицијент прелаза масе у флуидизованим слојевима и при вертикалном транспорту честица. Експериментални резултати су приказани у облику зависности Шервудовог броја и фактора преноса масе од Рејнолдсових бројева за колону и честице. Уведена је и величина псеудофлуид која третира двофазни систем течност–честице као суспензију одакле је проистекао модификовани Рејнолдсов број мешања. Увођењем ових величина дата је и завршна експериментална корелација, јединствена за флуидизоване слојеве и вертикални транспорт честица.

(Примљено 23. фебруара, ревидирано 1. јуна 2007)

REFERENCES

1. S. Damronglerd, J. P. Couderc, H. Angelino, *Trans. Inst. Chem. Engrs*. **53** (1975) 175
2. P. N. Dwivedi, S. N. Upadhyay, *Ind. Eng. Chem. Proc. Des. Dev.* **16** (1977) 157
3. S. Kumar, S. N. Upadhyay, *Ind. Eng. Chem. Fundam.* **20** (1981) 186
4. T. Chhun, J. P. Couderc, *Chem. Eng. Sci*. **35** (1980) 1707
5. T. Koloini, M. Sopčič, M. Žumer, *Chem. Eng. Sci*. **32** (1976) 637
6. K. Rahman, M. Streat, *Chem. Eng. Sci*. **36** (1981) 293
7. N. Yutani, N. Ototake, L. T. Fan, *Ind. Eng. Chem. Res*. **26** (1987) 343
8. J. P. Riba, R. Routie, J. P. Couderc, *Fluidization*, J. F. Davidson, D. L. Keairns, Eds. Cambridge, University Press, Cambridge, England, 1979, p. 157
9. N. Bošković, Ž. B. Grbavčić, D. V. Vuković, M. Marković–Grbavčić, *Powder Techn.* **79** (1994) 217
10. J. Lee, H. Chun, L. Shemilt, *J. Chem. Eng. Jap*. **30** (1997) 246
11. S. Schmidt, J. Buchs, C. Born, M. Biselli, *Chem. Eng. Sci*. **54** (1999) 829
12. S. Kumar, S. N. Upadhyay, *Ind. Eng. Chem. Fundam*. **19** (1980) 75
13. S. Kumar, S. N. Upadhyay, K. V. Mathur, *J. Chem. Eng. Data* **23** (1978) 139
14. D. Kunii, O. Levenspiel, *Fluidization Engineering*, Wiley, New York, 1969
15. S. N. Upadhyay, G. Tripathi, *J. Chem. Eng. Data* **20** (1975) 20
16. P. Tournie, C. Laguerie, J. P. Couderc, *Chem. Eng. Sci.* **32** (1977) 1259
17. P. Harriot, M. R. Hamiltin, *Chem. Eng. Sci.* **20** (1965) 1073
18. W. H. Linton, T. E. Sherwood, *Chem. Eng. Progr*. **46** (1950) 258
19. H. Hausen, *Allg. Wärmetechnik* **9** (1959) 75
20. E. Barnea, J. Mizrahi, *Chem. Eng. J.* **5** (1973) 171.

Journal of the Serbian Chemical Society
JSCS@tmf.bg.ac.yu • www.shd.org.yu/JSCS

J. Serb. Chem. Soc. 72 (11) 1115–1125 (2007)
JSCS–3646

UDC 546.56+661.183.8:620.1:536.421.5
Original scientific paper

Sintering of Cu–Al_2O_3 nano-composite powders produced by a thermochemical route

MARIJA KORAĆ[1]*, ZORAN ANĐIĆ[2], MILOŠ TASIĆ[2] and ŽELJKO KAMBEROVIĆ[1]

[1]*Faculty of Technology and Metallurgy, Karnegijeva 4, 11000 Belgrade and*
[2]*The Scientific Research Center, Nikole Pasica 26, 31000 Užice, Serbia*

(Received 25 April 2006)

Abstract: This paper presents the synthesis of nano-composite Cu–Al_2O_3 powder by a thermochemical method and sintering, with a comparative analysis of the mechanical and electrical properties of the obtained solid samples. Nano-crystalline Cu–Al_2O_3 powders were produced by a thermochemical method through the following stages: spray-drying, oxidation of the precursor powder, reduction by hydrogen and homogenization. Characterization of powders included analytical electron microscopy (AEM) coupled with energy dispersive spectroscopy (EDS), differenttial thermal and thermogravimetric (DTA–TGA) analysis and X-ray diffraction (XRD) analysis. The size of the produced powders was 20–50 nm, with a noticeable presence of agglomerates. The composite powders were characterized by a homogenous distribution of Al_2O_3 in a copper matrix. The powders were cold pressed at a pressure of 500 MPa and sintered in a hydrogen atmosphere under isothermal conditions in the temperature range from 800 to 900 °C for up to 120 min. Characterization of the Cu–Al_2O_3 sintered system included determination of the density, relative volume change, electrical and mechanical properties, examination of the microstructure by SEM and focused ion beam (FIB) analysis, as well as by EDS. The obtained nano-composite, the structure of which was, with certain changes, presserved in the final structure, provided a sintered material with a homogeneous distribution of dispersoid in a copper matrix, with exceptional effects of reinforcement and an excellent combination of mechanical and electrical properties.

Keywords: copper, alumina, powder, nano-composite, sintering.

INTRODUCTION

Research of nano-crystalline materials has intensified in recent years, primarily due to their attractive potential, *i.e.*, their properties which are significantly improved compared to conventional grain materials.[1–3] Nano-structured materials rank in the group of ultra fine, metastable structures containing a high concentration of defects (point defects, dislocations) and boundaries (grain boundaries, interphase boundaries, *etc*.). These materials are structurally different from crystals and amor-

* Corresponding author. E-mail: marijakorac@tmf.bg.ac.yu
doi: 10.2298/JSC0711115K

phous forms because of the fact that grain boundaries and interphases represent a specific state of the solid matter, since the atoms on boundaries are subjected to a periodical potential field of the crystal from both sides of the boundary.[2] Nano-structured materials can be synthesized in controlled processes by the following methods: condensation from the gas phase, synthesis in vacuum, high energy reactive milling, solution precipitation (sol–gel, hydrothermal synthesis, electrochemical synthesis, reactions in aerosol-reactive spraying, sublimation drying).[2,4]

The introduction of fine dispersed particles into a metal matrix has significant reinforcing effects, which can be maintained at elevated temperatures. For such a reinforcement, ultra fine and nano-particles of oxides are suitable, which, due to their hardness, stability and insolubility in the base metal, also represent obstacles to dislocation motion at elevated temperatures. The maximum effects of reinforcement are achieved by an even distribution of oxide particles and short distances of their fine dispersion in the matrix of the base metal.[4] Research of dispersion reinforced materials, indicates the significance of the properties of the starting powders and the importance of the starting structure, which, although undergoing certain changes during the further processing, basically remains preserved in the structure of the final product.[3,5] A very important aspect of dispersion strengthening is also the introduction of as small as possible amount of dispersed particles into the volume of the base material.

The above characteristics significantly determine the later-stage processing and sintering properties and eventually determine the microstructure of the composite. Uniform powder shape and a narrow size distribution provide reduced microstructural defects in the sintered composites, by enhancing powder flow and packing efficiency during slip casting and cold isostatic pressing (CIP).[6]

Obtaining powders by a thermochemical method, in which the input materials are in the liquid state, is not a new procedure but recently, due to the development of contemporary materials with advanced properties, intensive interest in this method for production of ultra fine and nano-powders has occurred.[7–9] According to Jena *et al.*[8,10] the synthesis of nano-composite powders by a chemical method is possible in two ways. The first method comprises adding of a certain quantity of CuO into a solution of aluminum nitrate. In the second synthesis method, aluminum nitrate and CuO are also mixed in appropriate proportions in distilled water. However, in this case, ammonium hydroxide is added to form a gel for the hydrolysis of aluminum nitrate to hydroxide. In both cases, the mixture was annealed at 850 °C and then reduced in a hydrogen atmosphere at 975 °C for 2 h until the final structure was obtained.

Nano-powders give better performance in sintering due to their high surface area and, therefore, can tremendously improve the sintering process. The part produced with nano-powders will have a high density, hardness and fracture toughness.[11]

Sintering of ultradispersed powders occurs due to sliding of the particles along their borders,[7] followed by a dislocative mechanism responsible for the creation

of surplus vacancies. The concentration of surplus vacancies can reach a value corresponding to the concentration of vacancies in the range of temperatures near the melting temperature of the materials. On this basis, it could be concluded that diffusion activity during sintering of ultradispersed particles in the area of really low temperatures (0.1–0.3 T_m) is conditioned by the presence of unbalancing "recrystallization" vacancies. The high recrystallization rate of ultradispersed particles is the consequence of a self-activated recrystallization process.

EXPERIMENTAL

Previous papers related to a similar topic[12] show soluble nitrates of copper and aluminum, $Cu(NO_3)_2{\cdot}3H_2O$ and $Al(NO_3)_3{\cdot}9H_2O$, could be used as a transient components for the thermochemical synthesis of nano-composite Cu–Al_2O_3 powders.

The synthesis process in this work followed four stages:

– making a 50 wt. % aqueous solution of $Cu(NO_3)_2$ and $Al(NO_3)_3{\cdot}9H_2O$; the quantities of salts were taken so that the required composition of the Cu–Al_2O_3 nano-composite system with 3 and 5 wt. % of alumina would be attained;

– spray drying using a modified house sprayer at a temperature 180 °C to produce the precursor powder;

– annealing of precursor powder in an air atmosphere at 900 °C for 1 h, thereby forming copper oxide and the phase transformation of Al_2O_3 to the thermodynamically stable phase (α-Al_2O_3);

– reduction of thermally treated powders in a hydrogen atmosphere at a temperature of 400 °C for one hour, whereby the copper oxide was transformed into elementary copper and the α-Al_2O_3 remained unchanged;

– homogenization in a jar mill, type TMF HM1, with milling chamber dimensions of: internal diameter 180 mm, height 160 mm and volume 4 l.

Characterization of the synthesized powders included AEM (JEOL 200CX), XRD (Siemens D500 PC, CuKα, 2θ = 1–100°, step (2θ) 0.02° and DTA–TGA (Netzch STA model 49EP).

After characterization, the powders were cold pressed from the both sides in an appropriate tool, 8×32×2 mm^3 at a compacting pressure of 500 MPa. A laboratory hydraulic power press "Zim", Russia, was used for the pressing. The obtained samples were sintered in a hydrogen atomsphere under isothermal conditions at two different temperatures, 800 and 900 °C, for 30, 60, 90 and 120 min. Sintering was performed in a laboratory electroresistance tube furnace, power 3 kW with thermoregulation ±1 °C. The internal diameter of the furnace was 45 mm and the length 100 cm. The maximum temperature in working area (55 cm) was 1300±1 °C.

The characterization of the sintered system of nano-composite Cu–Al_2O_3 included determination of the density, relative volume change, electrical and mechanical properties and examination of the microstructure by SEM, as well as by EDS analysis.

RESULTS AND DISCUSSION

Characterization of the Cu–Al_2O_3 powders

DTA–TGA Analysis of the nano-composite Cu–Al_2O_3 powder with 5 wt. % Al_2O_3, obtained by the thermochemical procedure, showed two endothermic peaks, at approximately 150 and 250 °C, which are related to the evaporation and dehydration of the residual moisture. The exothermic peak at 324 °C is accompanied by a mass increase of 5.88 %, which represents the beginning of the oxidation process of the fine copper powder present. An intensive mass increase was

registered on the TG curve at a temperature of approximately 550 °C, thereafter only an insignificant mass increase of some percents occurred, whereas the overall mass increment during heating was 28.43 %. A further increase of the temperature indicated the existence of four exothermic peaks at 684, 820, 885 and 938 °C, which correspond to the phase transformations of Al_2O_3 occurring in the system.

Only peaks corresponding to the nitrates of copper and aluminum were identified in the structure during XRD examination of the precursor powder produced by spray drying an aqueous solution of copper and aluminum nitrates, which is in accordance with the experiment set-up.[13] X-Ray diffraction analysis after annealing the dried powder exhibited peaks corresponding to CuO and Al_2O_3, as well as one unidentified peak. According to Lee,[9] this peak corresponds to a third phase, $Cu_xAl_yO_z$ which appears in the structure due to the eutectic reaction of ($Cu+Cu_2O$) with Al_2O_3. The formation of this phase is thermodynamically possible on Cu–Al contact surfaces. During eutectic joining of copper and Al_2O_3, the eutecticum formed by heating up to the eutectic temperature expands and reacts with Al_2O_3 creating $Cu_xAl_yO_z$, which is compatible with both phases on the inter-surface. XRD analysis of the powder after reduction shows the presence of peaks corresponding to elementary copper and Al_2O_3.[13]

The characterization of the nano-composite Cu–Al_2O_3 powder obtained by the thermochemical procedure also included examination by AEM, the results of which are shown in Fig. 1.

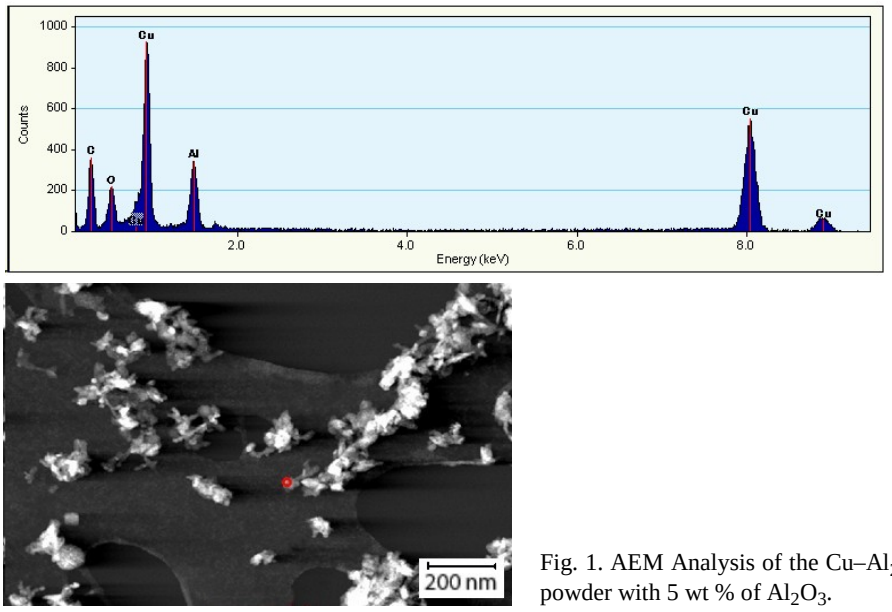

Fig. 1. AEM Analysis of the Cu–Al_2O_3 powder with 5 wt % of Al_2O_3.

Typical microstructural analysis of the powders shows the possibility of synthesis of the nano-composite Cu–Al_2O_3 system by the thermochemical proce-

dure, starting from aqueous nitrate solutions. Particles with a size of 20–50 nm are clearly visible, as well as the presence of agglomerates >100 nm. The particles are irregularly shaped, with the presence of individual nodular particles with a rough surface morphology.

The agglomeration of finer particles is a consequence of their large surface, *i.e.*, high surface energy, and the effect of bonding forces between them. Due to the contacts between the particles, interatomic bonds were formed. The magnitude of those bonds depends directly on surface energy of particles. Taking into account the appearance of agglomerates, particular attention will be paid in future research to the production of non-agglomerated powders, where surface-active agents will be used for de-agglomeration. Presently, the application of poly(ethylene glycol)[14] and ultrasonification[15–17] are considered.

Sintering

The results of density examination, relative volume change, specific electric resistance and hardness are given in Table I.

TABLE I. Average density, $\Delta V/V_0$, specific electric resistance and hardness of the sintered samples of Cu–Al_2O_3 with different aluminum content

t / °C	Time min	Density g cm^{-3}	$\Delta V/V_0$ (average)	Specific electric resistance 10^{-6} Ω m	Hardness HRB 10/40 (average)
Cu + 3 wt. % Al_2O_3					
800	15	5.58	0.1042	0.07413	88.2
	30	5.62	0.1194	0.07128	94.1
	60	5.70	0.1442	0.06581	102.1
	120	5.68	0.1448	0.06232	107.1
900	15	5.84	0.1821	0.06127	96.2
	30	6.14	0.1932	0.04027	101.9
	60	6.42	0.1933	0.03971	102.7
	120	6.44	0.1929	0.03927	102.3
Cu + 5 wt. % Al_2O_3					
800	15	5.28	0.0612	0.08941	89.1
	30	5.34	0.0982	0.08827	101.2
	60	5.52	0.1191	0.08146	107.5
	120	5.58	0.1332	0.08007	109.1
900	15	5.94	0.1763	0.07413	99.1
	30	5.98	0.1824	0.06981	108.4
	60	6.14	0.1894	0.06218	118.5
	120	6.20	0.1888	0.06127	124.7

At temperatures higher than 900 °C, *e.g.*, 1000 °C, the sintered plates were distorted because of the presence of a molten phase. Due to the small size of the

Cu–Al_2O_3 nano-powders, their maximum temperature of sintering is 900 °C, which is lower than for conventional powders.[5]

The results given in Table I show that the density of the sintered samples prepared at the same sintering temperature and time decrease with increasing content of Al_2O_3. However, with increasing temperature, the density of sintered samples increases. In the higher temperature range, where the diffusion mobility of the atoms is sufficiently high, a complex diffusion mechanism of mass transport, responsible for the sintering process occurred. With increasing sintering temperature, the actions of the complex mechanisms are more intense, directly affecting the formation of contacts between the particles, contact surface growth, formation of closed pores and grain growth. Therefore, with increasing temperature, the sintered density increases with time.

The available phenomenological sintering equations are based on the kinetics description of real dispersion systems, from the analysis of relative volume change. Relative volume change represents a measure of the activity a system as a function of temperature and time and is independent of the porosity of a pressed sample.[3] Regarding this, the influence of temperature, time and different content of Al_2O_3 on the relative volume change was investigated in this study. The change of relative volume, as a measure of system activity, increased with increasing sintering temperature for the same time and Al_2O_3 content. At a given Al_2O_3 content and temperature, the relative volume change increased with increasing time of sintering. The values of the relative volume change decreased with increasing content of Al_2O_3 for a constant temperature and time of sintering. Commencing from the general kinetic equations, with the aim of analyzing the sintering kinetics, the obtained results are in accordance with other research results and certainly confirm earlier investigations on the possibility employing existing phenomenological equations of sintering.[3]

The dependence of the specific electric resistance and hardness on the temperature, time of sintering and alumina content are presented in Figs. 2 and 3, respectively.

With increasing content of Al_2O_3, the duration of the sintering process increases. However, with increasing sintering temperature for the same time, the value of specific electric resistance decreases. In accordance with all these facts and bearing in mind that the change of specific electric resistance represents a measure of the structural stabilization of the system, it can be concluded that at certain temperatures structural stabilization of the system did not occur, *i.e.*, the structural stabilization process was not completed. Also, with increased sintering temperature, the duration of the sintering process is shortened (Fig. 2). Based on the value of specific electric resistance for the system with 3 % Al_2O_3 during sintering at 800 °C, the sintering process lasted for 120 min, while for the same system sintered at 900 °C, the sintering process lasted for 30 min.

The values of hardness of the sintered samples are in agreement with the values of the specific electric resistance, *i.e.*, the structural stabilization of the sys-

tem. These results also show an increase of hardness with increasing content of Al_2O_3, for the same temperature and sintering time. The obtained hardness results are the consequence of the relatively even distribution of Al_2O_3 particles in the copper matrix. A relatively even distribution of alumina in the nano-composite system, achieved during the synthesis of the powder during deposition from the liquid phase, leads to stabilization of the dislocation structure and achievement of significant reinforcing effects by the complex action of several mechanisms. Thereby, reinforcement of the small-grain material structure can be caused by reinforcing of the grain boundaries, dissolving reinforcement and the Orowan mechanism. Also dislocations can disappear in the grain boundaries or cease to multiply, since the Frenk–Read sources of dislocations cannot be activated in small-grained multi-phase materials, which represents an additional mechanism of reinforcement.[18]

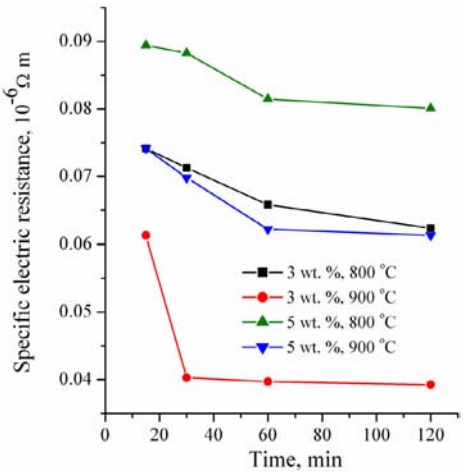

Fig. 2. Dependence of the specific electric resistance on the sintering time at different temperatures and different alumina contents.

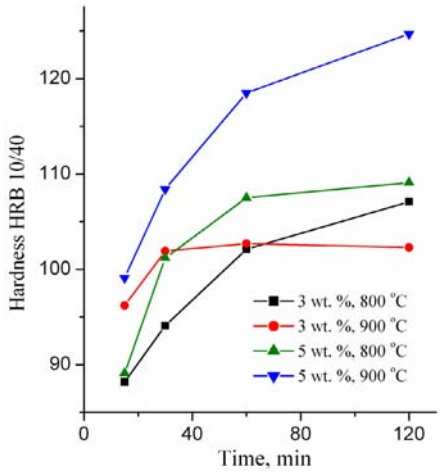

Fig. 3. Dependence of the hardness on the sintering time at different temperatures and different alumina contents.

Analysis of the electrical and mechanical properties of Cu–Al_2O_3 sintered systems showed that for the system with 3 wt. % of Al_2O_3 the structural stabilization had finished after 30 min of sintering at 900 °C, with significant reinforcement effects. For the other systems, the structural stabilization was not completed even after 120 min. As the optimal solution for the production of dispersed strengthened Cu–Al_2O_3 is the process conducted at 900 °C for 30 min with 3 wt. % of Al_2O_3, which was confirmed by microstructural analysis, presented in Figs. 4–6.

Analysis of the microstructure of the different sintered samples confirms these assumptions. The microstructure of the sample sintered at 800 °C for 30 min is given in Fig. 4, which clearly shows that the structural stabilization process was not completed. The microstructure is characterized by the formation of closed pores, typical for the medium stage of sintering. In certain areas, contacts between cer-

tain particles were achieved, which is typical for the starting stage of sintering. The microstructure of samples sintered at 900 °C for 15 and 30 min are presented in Figs. 5 and 6, respectively. The shown microstructures are characteristic for the medium (Fig. 5) and final stage (Fig. 6) of sintering, confirming the analysis of structural stabilization of the system based on the values of the specific electric resistance of sintered samples. In addition to this, a relatively even distribution of pores can be seen in the examined samples, which, together with other factors, significantly contributes to the reinforcement of the highly-conductive copper matrix.

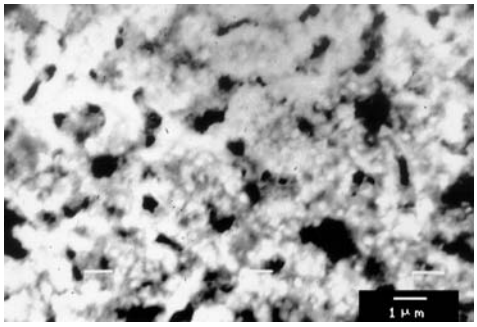

Fig. 4. SEM Microphotograph of the sintered Cu + 3 wt. % Al_2O_3 system (800 °C, 30 min).

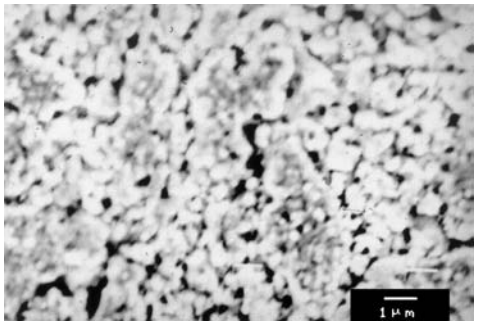

Fig. 5. SEM Microphotograph of the sintered Cu + 3 wt. % Al_2O_3 system (900 °C, 15 min).

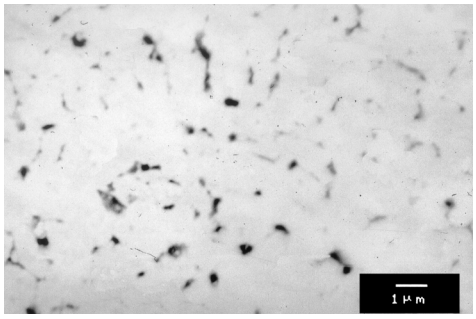

Fig. 6. SEM Microphotograph of the sintered Cu + 3 wt. % Al_2O_3 system (900 °C, 30 min).

In order to determine the distribution of elements in the structure, surface analysis of the sample was performed by EDS. The SEM microphotograph of the examined sample with the surface on which the surface scanning was performed marked is shown in Fig. 8, and the results of the examination of the sample of the sintered Cu–3 wt. % Al_2O_3 system by EDS are given in Fig. 9.

The results of surface scanning show a homogeneous distribution of elements in the structure. From Fig. 9, it can be seen that copper covers almost the entire surface of the sample. The results of surface scanning for aluminum and oxygen show that these two elements are present less in the structure of the sintered sample and the surfaces they occupy are inter-lapping, which corresponds to the existence of an Al_2O_3 dispersoid in the structure. Except for aluminum and oxygen, an inter-lapping of all three elements is also noticeable, which leads to the assumption of

the presence of a $Cu_xAl_yO_z$ phase.[10] Finally, for a detailed characterization of the third $Cu_xAl_yO_z$ phase, an apparatus of exceptionally high resolution is necessary.

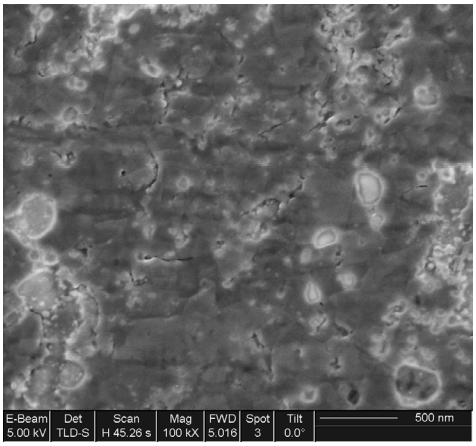

Fig. 7. Focused Ion Beam (FIB) analysis of the sintered Cu + 5 wt. % Al_2O_3 system.

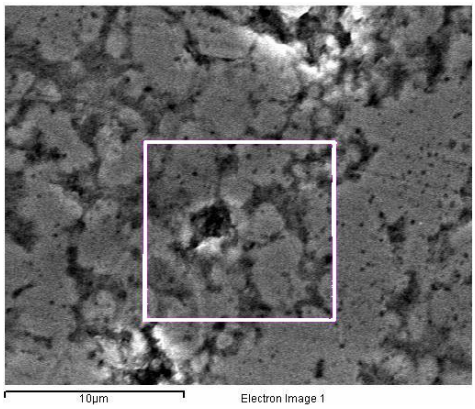

Fig. 8. SEM Microphotograph of a sintered Cu–3 wt. % Al_2O_3 sample with the surface scanning area marked.

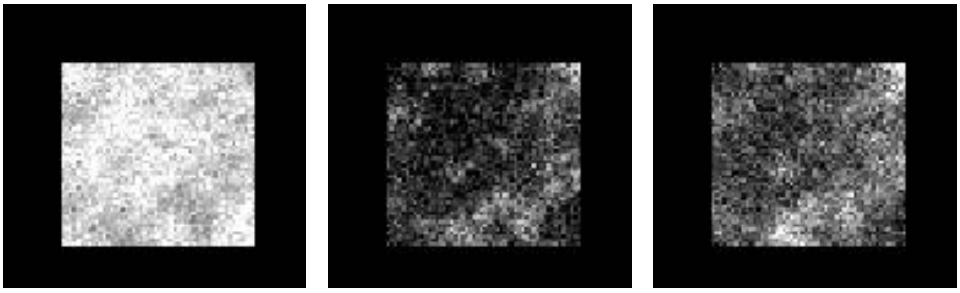

Copper Aluminum Oxygen

Fig. 9. Surface scanning of a sintered Cu–3 wt. % Al_2O_3 sample by EDS.

CONCLUSIONS

Detailed characterization of the obtained powders indicate the possibility of the synthesis of nano-composite Cu–Al_2O_3 powders, with a particle size 20–50 nm, by a thermochemical method.

Such obtained nano-composite powders, the structures of which are preserved in the structure of the final product, enabled the production of a sintered system with exceptional reinforcement and a good combination of mechanical and electrical properties. Thus, the results of hardness examination of the sintered samples showed that the increase of the hardness is in reverse relationship to the reduction of the specific electric resistance, *i.e.*, structural stabilization of the system, which was confirmed by microstructural examination. The significant effects of reinforcement achieved are the consequence of a relatively even distribution of Al_2O_3 in a copper metal matrix, already achieved in the process of pow-

der synthesis by depositing from the liquid phase. This was also confirmed by the results of analysis by EDS of the surface of the samples.

The identification of $Cu_xAl_yO_z$ phases in the structure and a study its influence on the stabilization of the dislocated structure and consequential improvement of mechanical properties, as well as the attainment of a better combination of mechanical and electrical properties of the sintered systems are essential aspects of this research, which will be continued.

Acknowledgement: The authors are grateful to Prof. Dr. Velimir Radmilovic from the National Center for Electron Microscopy, Berkeley, USA, for his assistance with the AEM and FIB analysis.

И З В О Д

СИНТЕРОВАЊЕ НАНО-КОМПОЗИТНИХ ПРАХОВА Cu–Al_2O_3 ДОБИЈЕНИХ ТЕРМОХЕМИЈСКИХ ПОСТУПКОМ

МАРИЈА КОРАЋ[1], ЗОРАН АЊЂИЋ[2], МИЛОШ ТАСИЋ[2] и ЖЕЉКО КАМБЕРОВИЋ[1]

[1]Технолошко–металуршки факултет, Карнегијева 4, 11000 Београд и
[2]Научно-истраживачки центар, Николе Пашића 26, 31000 Ужице

У овом раду представљена је синтеза нано-композитног праха Cu–Al_2O_3 термохемијском методом и синтеровањем, уз упоредну анализу механичких и електричних својстава добијених чврстих узорака. Нано-кристални Cu–Al_2O_3 прахови добијени су термохемијском методом у следећим корацима: сушење распршивањем, оксидација полазних прахова, редукција водоником и хомогенизација. Прахови су окарактерисани аналитичком електронском микроскопијом (AEM) спрегнутом са спектроскопијом енергије расејања (EDS), диференцијалном термијском и термогравиметријском анализом (DTA–TGA) и дифракцијом X-зрака (XRD). Величина честица добијених прахова износила је 20–50 nm, уз знатно присуство агломерата. Композитни прахови карактеришу се хомогеном расподелом Al_2O_3 у бакарној матрици. Прахови су пресовани на хладно притиском од 500 MPa и синтеровани у атмосфери водоника под изотермским условима у температурном опсегу од 800 до 900 °C у трајању до 120 мин. Карактеризација Cu–Al_2O_3 синтерованог система укључивала је одређивање густине, релативне промене запремине, електричних и механичких својстава, испитивање микроструктуре техником SEM, анализом помоћу усмереног јонског снопа (FIB) и техником EDS. Добијени нано-композит, чија је структура, уз извесне промене, присутна и у коначној структури синтерованог материјала, омогућава хомогену расподелу дисперзоида у бакарној матрици синтерованог материјала, са израженим ефектима ојачања, и одличну комбинацију механичких и електричних својстава.

(Примљено 25. априла 2006)

REFERENCES

1. J. Karch, R. Birringer, H. Gleiter, *Nature* **330** (1987) 556
2. O. Milošević, *Material Science Monograph of the Serbian Academy of Science and Arts, SANU*, **38** (1999) 55
3. M. M. Ristić, *Fundamental problems of material science*, Technical Faculty of Čačak and SANU, Belgrade, (2003) p. 41
4. F. H. Froes, O. N. Senkov, E. G. Baburaj, *Mat. Sci. Eng.* **A301** (2001) 44
5. Z. Anđić, M. Tasić, M. Korać, B. Jordović, A. Maričić, *Mater. Technol*. **38** (2004) 245
6. O. Vasylkiv, Y. Sakka, *J. Am. Ceram. Soc*. **84** (2001) 2489

7. Y.–Q. Wu, Y.–F. Zhang, X.–X. Huang, J.–K. Guo, *Ceram. Internat.* **27** (2001) 265
8. P. K. Jena, E. A. Brocchi, M. S. Motta, *Mater. Sci. Eng*. **A313m** (2001) 180
9. D. W. Lee, G. H. Ha, B. K. Kim, *Scripta Mater*. **44** (2001) 2137
10. P. K. Jena, E. A. Brocchi, I. G. Solórzano, M. S. Motta, *Mater. Sci. Eng*. **A317** (2004) 72
11. NanoPowder Industries, http://www.nanopowders.com/applications.htm (Jan 28, 2006)
12. M. Korać, *M.Sc. Thesis*, Faculty of Technology and Metallurgy, University of Belgrade, 2005 (in Serbian)
13. Z. Anđić, M. Korać, Ž. Kamberović, M. Tasić, *Book of Abstracts*, in *Proceeding of V Scientific Meeting: Physics and Technology of Materials, FITEM '04*, Čačak, SCG, (2004), p. 71
14. Y.–Q. Wu, Y.–F. Zhang, X.–X. Huang, J.–K. Guo, *Ceram.Internat*. **27** (2001) 265
15. P. K. Jena, E. A. Brocchi, M. S. Motta, *Mater. Sci. Eng*. **C15** (2001) 175
16. M. Entezarian, R. A. Drew, *Mater. Sci. Eng.* **A212** (1996) 206
17. D. W. Johnson Jr., D. J. Nitti, L. Berrin, *Bull. Amer. Ceram. Soc*. **51** (1972) 896
18. D. G. Morris, M. A. Morris, in *Structural Applications of Mechanical Alloying*, F. H. Froes, J. J. DeBarbadillo, Eds., ASM, Metals Park, Ohio, 1992, p. 265.

Journal of the Serbian Chemical Society
JSCS@tmf.bg.ac.yu • www.shd.org.yu/JSCS

J. Serb. Chem. Soc. 72 (11) 1127–1138 (2007)
JSCS–3647

UDC 546.284–31.002.2:539.22:666.293.35
Original scientific paper

Fabrication of SiO_2-based microcantilevers by anisotropic chemical etching of (100) single crystal Si

VESNA JOVIĆ*#, JELENA LAMOVEC, MIRJANA POPOVIĆ# and ŽARKO LAZIĆ

Institute of Chemistry, Technology and Metallurgy – Center for microelectronic technologies and single crystals, Njegoševa 12, Belgrade, Serbia

(Received 19 July 2006)

Abstract: The undercutting process of thermal SiO_2 microcantilevers with different orientations on (100) Si wafer was studied. The silicon substrate was removed by anisotropic chemical etching with a 25 wt. % aqueous solution of TMAH or a 30 wt. % aqueous KOH solution at 80 °C. It was found that ⟨110⟩ oriented cantilevers were undercutting frontally along the length and ⟨100⟩ oriented cantilevers experience undercutting along the width of the cantilever, which is a less time consuming process. The studies showed that the ⟨100⟩ orientation of SiO_2 microbridges enables theirs fabrication on a (100) oriented Si substrate.

Keywords: anisotropic wet chemical etching, TMAH, KOH, SiO_2 microcantilever, SiO_2 microbridge, (100) oriented Si substrate.

INTRODUCTION

Since its discovery in the middle of the 1960s, anisotropic wet chemical etching[1] of single crystal silicon (sc Si) has been widely used in the semiconductor industry. Nowadays this technique is applied in the fabrication of different types of sensors and actuators and optical components in micro-electro-mechanical-system (MEMS) technologies.[2]

Microcantilevers and microbridges are one of the major diagnostic structures not only in a variety of sensors,[3] but also for measuring mechanical (*e.g.* residual stress and Young's modules)[4] or thermal (*e.g.* thermal expansion coefficients)[5] properties of thin films used in MEMS technologies.

This paper describes the experimental results used to investigate the correlation between the orientation of the microcantilevers and microbridges after anisotropic wet etching of silicon substrates. In the fabrication of SiO_2 microcantilevers or microbridges, anisotropic wet etching of Si substrate beneath the SiO_2 film creates free standing structures. Silicon dioxide is relatively insoluble in aque-

* Corresponding author. E-mail: vjovic@nanosys.ihtm.bg.ac.yu
# Serbian Chemical Society member.
doi: 10.2298/JSC0711127J

ous alkaline solutions of TMAH (tetramethylammonium hydroxide) or KOH which are used for anisotropic etching.[2] SiO_2 thin films are transparent which enables the observation of the Si undercut processes during etching. Conclusions about the anisotropic etching of sc Si substrates could be useful in etching microcantilevers made from opaque materials insoluble in these solutions. Also, many SiO_2-based microcantilever systems are successfully designed and fabricated for various MEMS applications.[6,7] Hence, the main aim of this work was to establish the conditions for Si substrate undercutting during the course of etching and find the optimal orientation of the released microcantilevers and microbridges.

EXPERIMENTAL

The SiO_2 microcantilevers used for these experiments had been fabricated on n-type (boron-doped) sc Si wafers with the (100) orientation. The Si wafers were mirror polished and has resistivity values between 5 and 3 Ω cm. Approximately 1 μm thermal oxide was grown on the Si substrate in oxygen ambient saturated with H_2O vapor. The temperature for the silicon oxide growth was 1115 °C. Designed structures were patterned using a standard photolithographic technique[8] and openings in the SiO_2 were etched using a buffer oxide etch. The cantilevers patterns were aligned to the prime wafer flat on the (100) Si substrate, *i.e.*, along the ⟨110⟩ direction. Two types of cantilevers and microbridges orientations were investigated: one parallel to the prime flat or aligned to the ⟨110⟩ direction and the other was oriented to the ⟨100⟩ direction, which is 45° from the prime wafer flat. The dimensions of the designed cantilevers and microbridges were 25, 50 or 100 μm in width and 100, 200, 300 or 500 μm in length.

The etching process was carried out using two alkaline solutions which are the most frequenttly used in MEMS processing, namely: a 25 wt. % aqueous TMAH solution or a 30 wt. % aqueous KOH solution. The solutions are held in a thermostated Pyrex glass vessel at the etching temperature of 80 °C (temperature stabilization ±0.5 °C) for both solutions. The vessel was sealed with a screw on lid which included a tap water cooled condenser, to minimize evaporation during the etching. During the etching, the wafer was held in a Teflon holder in the horizontal position above a magnetic stirrer bar. The solution was electromagnetically stirred at 700 rpm. A detailed description of the apparatus is given in the literature.[9]

After the etching process, the etched wafers were removed from the solution and thoroughly rinsed with deionized water without the application of any procedure[10] for the prevention of cracking or stiction of the released microcantilevers. In future work with the aim of fabricating microcantilevers for specific application, drying and stiction problems should be resolved because they are directly connected with yield of fabricated devices.

The released structures were subjected to microscopic observations using a high power optical microscope “Epival Interphako”, Carl Zeiss, Germany, which allows for longitudinal in plane measurement. To estimate the etch rates of the examined crystal planes, the depth of etching was measured using a special micrometric gauge.

RESULTS AND DISCUSSION

It is well known that Si has a diamond cubic structure and its anisotropic etching behavior strongly depends on the crystal orientation.[2] The family of {100} planes in silicon posses four fold symmetry and their anisotropic etching can produce either vertical {100} walls or sloping {110} or {111} walls, inclined at 45° or 54.7°, respectively.[11] Plane formation of a sidewall during anisotropic wet chemical etching is the one with the slowest etch rate aligned to the mask edge. All these possibilities are shown in Fig. 1.

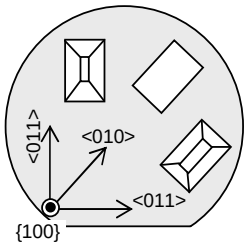

Fig. 1. Different structure types which can be produced by anisotropic etching on a (100) Si substrate. Gray field represents the masking material (SiO_2).

To achieve {111} walls, the pattern edges must be in the ⟨110⟩ direction, which is also the direction of the prime flat in (100) Si wafers. {111} Planes are the slowest etching planes in both the solutions examined in this work.

When the pattern edge is aligned along the ⟨100⟩ direction, *i.e.*, 45° from the prime flat, the selection of walls bounded pattern depends on relative etch rates of the {110} and {100} planes. There is small difference between these two etch rates and they are very sensitive toward the employed solution, etching conditions, temperature, additives, impurities in solution, *etc*.

The method of evaluation of the etching rates of some crystallographic plane is illustrated in Fig. 2. The etched depths (*d*) on Si (100) substrate were measured using a micrometer gauge and the lateral distances were measured under an optical microscope.

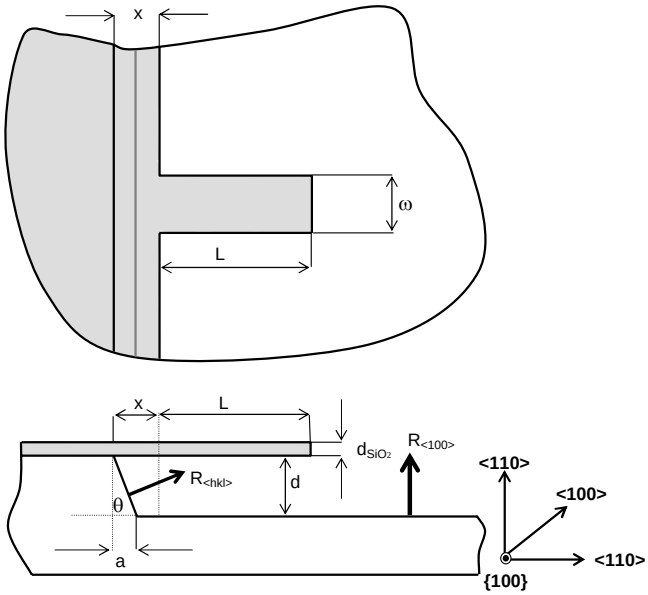

Fig. 2. The method for estimating the etch rate of Si crystallographic planes. A SiO_2 microcantilever is released by undercutting of the Si substrate.

By measuring the etching depth (*d*) in the ⟨100⟩ direction and knowing the etching time (τ), the etch rate of the (100) plane, $R_{\langle 100\rangle}$, is calculated from the Equation:

$$R_{\langle 100\rangle} = d\,\tau^{-1} \tag{1}$$

By measuring the distance a, which is the side wall projection on the (100) surface, the angle of inclination, θ, of the developed plane toward the (100) substrate surface can be estimated as:

$$\theta = \text{arctg}\,\frac{d}{a} \tag{2}$$

This angle determines unambiguously which crystallographic plane has developed in the considered crystal direction. The etch rate of a developed sloped plane with {hkl} orientation can be estimated from the formula:

$$R_{\langle hkl\rangle} = \frac{x \sin\theta}{\tau} \tag{3}$$

where x is the undercutting of the oxide mask. It is important to notice that x denotes not only the undercutting of the oxide mask, but also the distance which defines how ideally the microcantilever is clamped. For ideally clamped microcantilevers, $x = 0$.

By measuring the etching depth in the ⟨100⟩ direction for a given etching time, it is possible to determine the etching rate (Eq. (1)) of the (100) planes in both solutions. Etching rates are 0.44 μm min^{-1} for the 25 wt. % aqueous TMAH solution at 80 °C and 1.30 μm min^{-1} for the 30 wt. % aqueous KOH solution at 80 °C. The etching rate of the sloped {111} planes were determined in both solutions using Eq. (3), knowing the slope angle ($\theta = 54.7°$) and measuring x for a given etching time. The determined etching rates of the {111} planes are 2.2×10^{-2} and 5.0×10^{-3} μm min^{-1} for the TMAH and KOH solution, respectively.

The etching rates experimentally determined in this work are in agreement with those reported in the literature.[11]

The photographs in Fig. 3 display the undercut process of various microcantilevers oriented in the ⟨110⟩ direction on a (100) Si wafer. The photographs were obtained using the optical microscope (OM) working in reflected light. The microcantilevers of different widths and lengths were etched in a 25 wt. % aqueous TMAH solution for two different etching times. These photographs illustrate the Si undercutting process and the release of SiO_2 microcantilevers. The lateral sides of the microcantilevers are bounded with the slowest etching {111} planes and the release process was practically performed by undercutting of the convex-corners at the top of the microcantilever.

The successive steps during undercutting of the substrate below the masking material are schematically presented in Fig. 4. The dashed lines are traces of Si planes in the (100) substrate during the course of undercutting. For microcantilevers oriented in the ⟨110⟩ direction, the general picture of Si undercutting was similar for both applied solutions (*i.e.*, TMAH and KOH).

This is well illustrated for etching in 30 wt. % KOH solution in Fig. 5. The OM photographs of microcantilevers oriented in the ⟨110⟩ directions are shown in

Fig. 5a after their etching for 30 min. in the KOH solution. Completely released SiO_2 microcantilevers of 200 μm length but of different widths are shown in Fig. 5b.

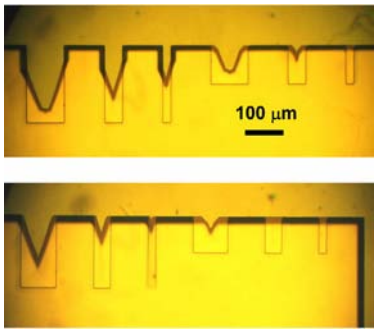

Fig. 3. OM Photographs of the microcantilevers undercut process in 25 wt. % TMAH solution on (100) Si wafers when the etching time was 0.75 h (top) and 1.25 h (bottom). The microcantilevers were oriented in the ⟨110⟩ direction.

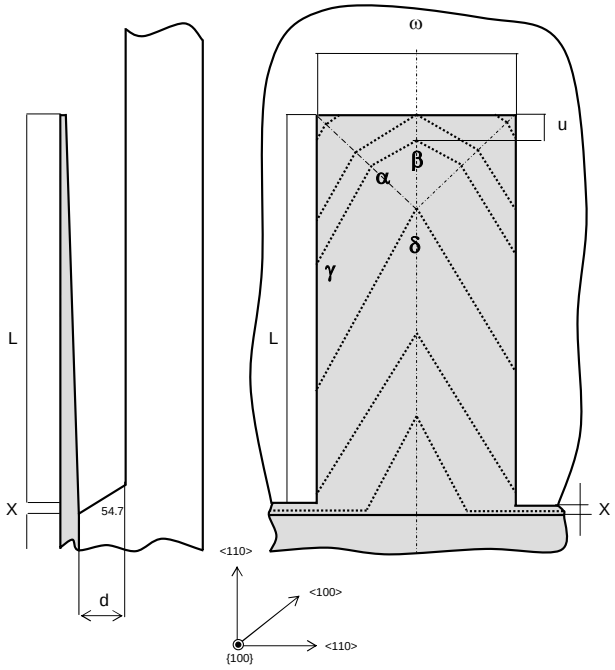

Fig. 4. Schematic presentation showing the evolution of an undercutting configuration of ⟨110⟩ orientted microcantilevers, which results in their release.

From the evolution of Si undercutting during the release of ⟨110⟩ oriented microcantilevers, it can be seen that {111} crystallographic planes stop the undercut from the edge of the microcantilevers. Hence, for ⟨110⟩ oriented microcantilevers the undercutting results from the convex corner effect, this spreads along the cantilever length. The undercutting mechanism was the same in both solution, and only difference lay in type of the fastest etching planes which bound the convex corners at the fronts of the microcantilevers. This means that the angles shown in Fig. 4 are different for each solution. Details of the values of the angles from Fig. 4 for both solutions are compiled in Table I. Traces in the (100) substrate of

the fastest etching planes, the undercutting of which determines the undercutting of the convex corner,[2,13] are given in Table I.

(a)

(b)

Fig. 5. OM Photographs of ⟨110⟩ oriented microcantilevers released by wet chemical etching in 30 wt. % aqueous KOH solution: (a) etching time 30 min, (b) completely released SiO_2 microcantilever. The released SiO_2 microcantilever shows color variations due to the change in thickness as a result of chemical dissolution in the used solution.

TABLE I. Numerical values of the angles characterizing the undercutting of the substrate for ⟨110⟩ oriented microcantilevers on (100) Si substrate for etching in KOH and TMAH solutions at the temperature of 80 °C (according to the sketch in Fig. 4)

Angle	30 wt. % KOH	25 wt. % TMAH
	{410}	{520}
α / °	152	136.4
β / °	118	133.6
δ / °	62	46.5
γ / °	149	156.8

Knowledge of the exact orientation of the planes binding the convex corner of Si is very important when the microcantilever is made from silicon itself. In this case, undercutting of the convex corners must be avoided in order for the microcantilever to maintain its predetermined shape.[14]

The schematic presentation in Fig. 3 shows a cross-section of a released SiO_2 microcantilever along its longer axis, from which it can be seen that there is continuous thickness change. The change in the thickness of a microcantilever is more pronounced when the etch rate of the material (SiO_2 in this case) is higher. The geometry (especially thickness) of a microcantilever is a key factor for the accuracy of a measurement when microcantilevers are applied as measurement or diagnostic devices.[15]

By measuring the height of the SiO_2 steps after etching, the etching rates of cantilever's material were estimated as: 0.13 nm min^{-1} in the TMAH solution (25 wt. %, 80 °C) and 7.3 nm min^{-1} in the KOH solution (30 wt. %, 80 °C). Thus SiO_2 is much more stable in the TMAH solution, which is well illustrated in Fig. 5b. The completely released microcantilevers in this photograph show a variety colors, which is the outcome of the different thickness of the SiO_2. Such

color changes were not observable for the SiO_2 microcantilevers released in the TMAH solution, which is quite understandable bearing in mind that the SiO_2 etch rate is approximately sixty times slower in TMAH than in KOH under the given etching conditions.

Sometimes, microcracks were observed during the etching of microcantilevers oriented along the ⟨110⟩ direction, as can be seen in Fig. 6a. In addition, some cantilevers broke along the microcracks (Fig. 6b). The appearance of cracks is due to the effect of stress concentration at the tip of the sharp corner shown in Fig. 4 (angle δ).

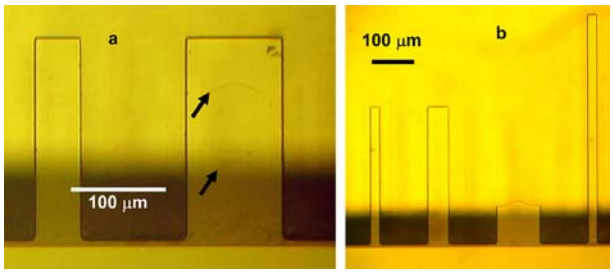

Fig. 6. MO Photographs of (a) ⟨110⟩ oriented SiO_2 microcantilevers with microcracks on the wider one (marked with the arrows) and (b) the breakage of a microcantilever along a previously formed microcrack.

Concerning microcracks in SiO_2 microcantilevers, it must be born in mind that internal stress is unavoidable in thermally grown silicon dioxide.[16] Undoubtedly, the interference of these stresses facilitate cantilever breakage.

Knowledge of the etching time required to fabricate a cantilever with a given length (L) and width (ω) is very important. Every time a wafer with cantilevers has to be removed from the etching solution to control the completeness of undercutting, the probability for the cantilever to break or stick increases. As indicated by the dashed lines in Fig. 4, the undercut of a ⟨110⟩ oriented cantilever is along its length. This means that cantilevers of the same lengths are going to undercut for a longer time the broader they are. The measured results for undercutting Si substrate in ⟨110⟩ direction (u, in μm) in dependence of etching time (τ, in min) is shown in Figs. 7a and 7b, for the KOH solution and TMAH solution, respectively.

When the undercutting, u, equals to the length of cantilever (L), it is completely released. The sloped plane under the place where the microcantilever was clamped is a plane from the {111} family, the slowest etching plane in the examined solutions, thus $\theta = 54.7°$ (Fig. 2).

To release a SiO_2 microcantilever of 500 μm length and 25 μm width with a ⟨110⟩ orientation on a (100) Si substrate, 120 min etching in the KOH solution and 180 min etching in the TMAH solution were required. The etching depth of a (100) substrate (d in Fig. 2) was 79 μm for the TMAH solution and 156 μm for the KOH solution. The SiO_2 undercutting (denoted by x in Figs. 2 and 4 and calculated from Eq. (3)) for these etching times was 0.7 μm and 4.3 μm for etching in the KOH and TMAH solutions, respectively.

Considering SiO_2 microbridges as beams clamped at both ends, it can be seen that their fabrication for the ⟨110⟩ orientation on Si (100) substrates is impossible.

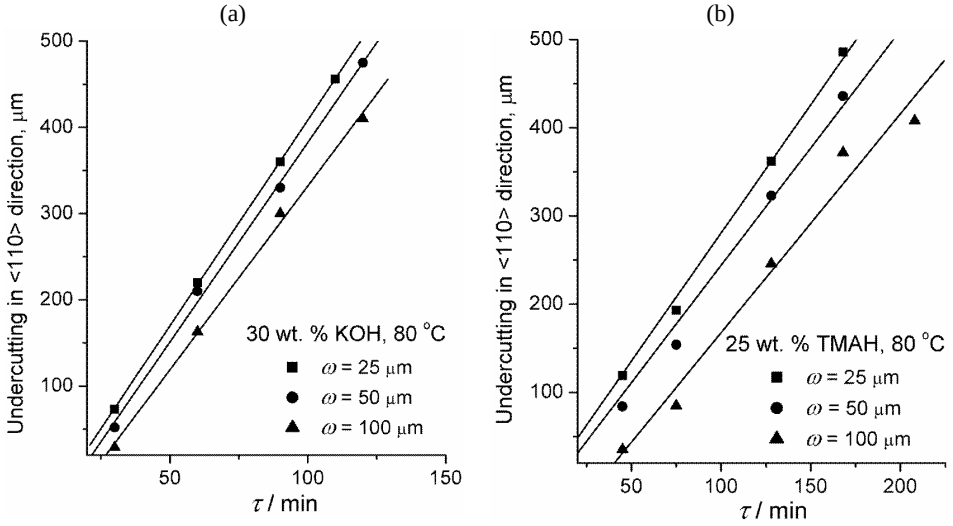

Fig. 7. The experimental relation between undercutting and etching time for ⟨110⟩ oriented SiO_2 cantilevers on a (100) Si substrate with different widths (ω). The cantilevers were released by anisotropic chemical etching in (a) 30 wt. % aqueous KOH solution and (b) 25 wt. % aqueous TMAH solution. The etching temperature was 80ºC.

Photographs from the optical microscope of microcantilevers oriented in the ⟨100⟩ direction on a Si (100) substrate (*i.e.*, 45° from the prime wafer flat) after etching in the TMAH solution and KOH solution are shown in Figs. 8 and 9, respectively.

From these photographs it is obvious that the release of ⟨100⟩ oriented SiO_2 microcantilevers on a (100) Si substrate occurs by undercutting of the substrate along the length of a microcantilever. At the very first moments of undercutting, the Si structure beneath the cantilever is bound by high index planes with the highest etch rates but as the etch time elapses, the dominant undercutting mechanism is lateral etching, as is schematically shown in Fig. 10.

This undercut process protects the cantilever from the formation of microcracks due to the stress concentration effect of the sharp corner. Also, the etching time required to fabricate a cantilever is independent of the cantilever length and depends only of its width. The cross-section of microcantilever is trapezium (Fig. 10) and the change of thickness is symmetrical about longitudinal axis of the microcantilever.

For ⟨100⟩ oriented microcantilevers fabricated by etching in the TMAH solution, the sloped plane underneath the clamp position is from the {110} family, hence the angle $\theta = 45°$ (Fig. 10). In the TMAH solution, under the given etching conditions, $R_{\langle 110\rangle} < R_{\langle 100\rangle}$, θ is determined from Eq. (2) by measuring the etching depth (d) of the Si substrate (in the ⟨100⟩ direction) and the length of the side-wall projection of this oblique plane on the (100) substrate surface (a). The etching rate

of the {110} planes was calculated from Eq. (3) and the measured value of x, as $R_{\langle 110\rangle} = 0.32\ \mu m\ min^{-1}$.

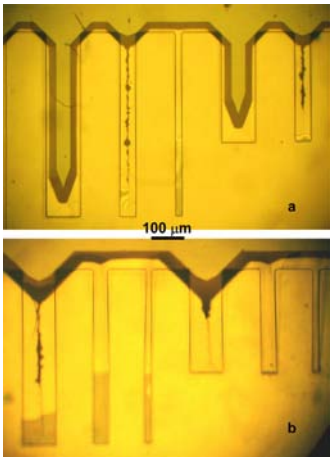

Fig. 8. OM Photographs of SiO_2 microcantilevers etched in a 25 wt. % aqueous TMAH solution at 80 °C. The microcantilevers are oriented in ⟨100⟩ direction on a (100) Si substrate. The etching time was: (a) 60 min. and (b) 120 min. It can be seen that some of the microcantilevers are stuck on the substrate.

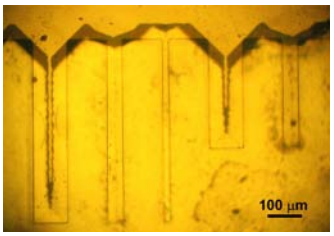

Fig. 9. OM Photographs of SiO_2 microcantilevers etched in a 30 wt. % KOH solution at 80 °C for 30 min. The microcantilevers are oriented in the ⟨100⟩ direction on a (100) Si substrate.

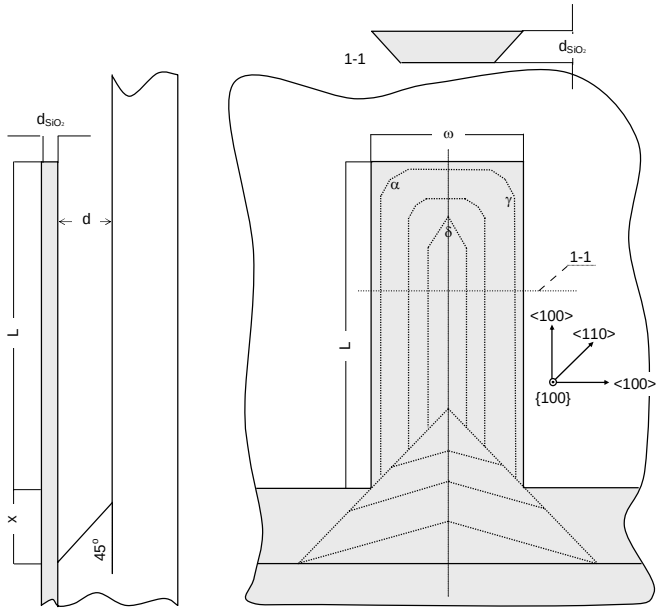

Fig. 10. Undercut process of a SiO_2 microcantilever oriented in the ⟨100⟩ direction on a (100) Si substrate.

For the etching of ⟨100⟩ oriented microcantilevers in the KOH solution, there is no sloping planes underneath the clamp positions because under these etching

conditions $R_{\langle 100\rangle} < R_{\langle 110\rangle}$. From Fig. 9 and the calculations from the measured values, it can be seen that $\theta = 90°$ (in Fig. 2).

The results shown in Fig. 11 indicate that the etching time for ⟨100⟩ oriented microcantilevers is smaller than for microcantilevers oriented in the ⟨110⟩ direction if they have same width and length. This is true for both examined solutions.

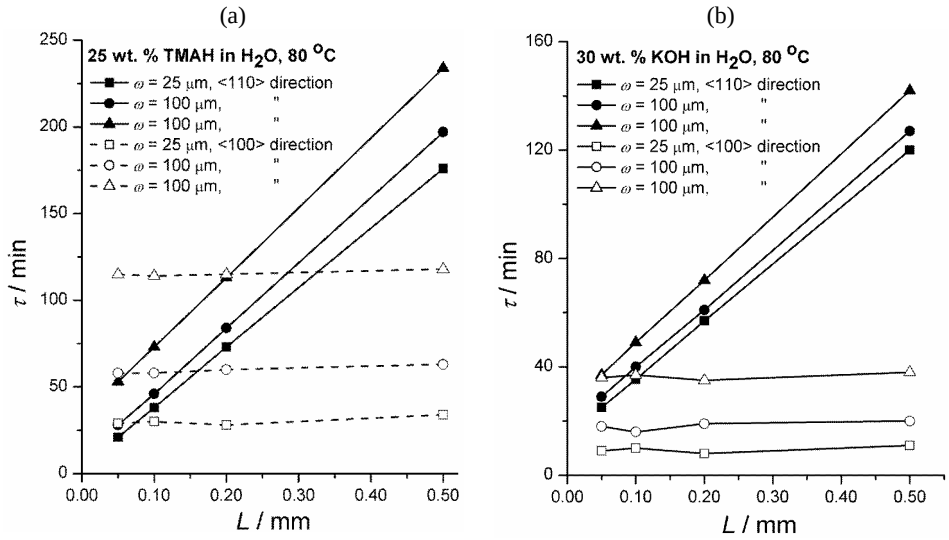

Fig. 11. The relation between beam length, L, and etching time, τ, for microcantilevers orientated in the ⟨110⟩ direction (black symbols) and the ⟨100⟩ direction (open symbols) on aSi (100) substrate for both employed etching solutions: (a) 25 wt. % aqueous TMAH solution and (b) 30 wt. % KOH solution at 80 °C.

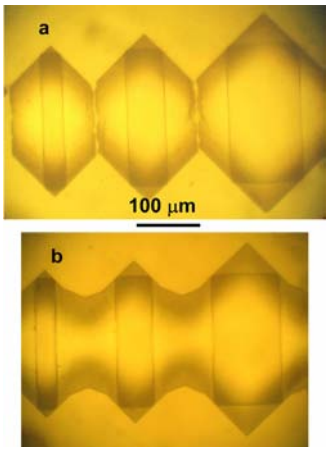

Fig. 12. SiO_2 microbridges oriented in the ⟨100⟩ direction on a (100) Si substrate which were (a) almost released by chemical etching in a 30 wt. % aqueous KOH solution and (b) completely released after etching in a 25 wt. % aqueous TMAH solution.

According to the undercut mechanism and the results shown in Fig. 11, the advantages of fabricating a microcantilevers with a ⟨100⟩ orientation over ones oriented in the ⟨110⟩ direction on a (100) Si substrate is the reduction of the etching time and the more appropriate cross-section of the cantilever for various applications.

Inspecting the SiO_2 microbridges oriented in the ⟨100⟩ direction in the Si (100) substrate, it is obvious that they could be released by wet chemical etching in these solutions, as is shown in Fig. 12.

CONCLUSIONS

This paper introduces some aspects of fabricating microcantilevers made from thermally grown SiO_2, with different orientation on Si (100) substrates. SiO_2 microcantilevers with either a ⟨110⟩ or ⟨100⟩ orientation were released by silicon undercutting in two solutions most often employed in micromachining technologies, namely 25 wt. % TMAH and 30 wt. % KOH aqueous solutions. The etching temperature was 80 °C for both solutions.

The ⟨110⟩ oriented microcantilevers are released by frontal undercutting and their etching time depends both on the width and length of the cantilevers. Also, such oriented microcantilevers exhibit thickness variation along their lengths and, due to the undercutting mechanism, are subject to microcrack development.

SiO_2 microcantilevers oriented in the ⟨110⟩ direction were fabricated by undercutting of the Si (100) substrate along theirs widths. The release of ⟨100⟩ oriented microcantilevers depends only of their widths and not on their lengths. The cross-section of SiO_2 microcantilevers oriented in such a way remains roughly rectangular, which is better for their further application.

It is possible to fabricate SiO_2 microbridges on a (100) oriented Si substrate by wet chemical etching only if they are oriented in the ⟨100⟩ direction.

*Acknowledgmen*t: This work was performed in the frame of the project “Micro and Nanosystems Technologies, Structures and Sensors”, supported by grants from the Ministry for Science of the Republic of Serbia, Grant No. TP-6151B.

И З В О Д

ИЗРАДА МИКРОГРЕДИЦА ОД SiO_2 АНИЗОТРОПНИМ ХЕМИЈСКИМ НАГРИЗАЊЕМ НА МОНОКРИСТАЛНОМ СИЛИЦИЈУМУ (100) ОРИЈЕНТАЦИЈЕ

ВЕСНА ЈОВИЋ, ЈЕЛЕНА ЛАМОВЕЦ, МИРЈАНА ПОПОВИЋ и ЖАРКО ЛАЗИЋ

Институт за хемију, технологију и металургију – Центар за микроелектронске технологије и монокристале, Његошева 12, Београд

Изучавана је реализација микрогредица од термички депонованог SiO_2 на монокристалним подлогама Si (100) оријентације. Гредице су реализоване анизотропним хемијским нагризањем у следећим воденим растворима: 25 теж. % TMAH (тетраметиламонијум хидроксид) и 30 теж. % KOH. Температура нагризања је била 80 °C. SiO_2 микрогредице оријентисане у ⟨110⟩ правцу на Si (100) подлози се ослобађају чеоним подгризањем Si подлоге и брзина реализације гредице зависи и од њене ширине и од њене дужине. Утврђене су и брзине нагризања SiO_2 у овим растворима и показало се да промена дебљине гредице, која за овако оријентисане гредице постоји по дужини, бива израженија у растворима KOH. На SiO_2 микрогредицама ове оријентације је опажена појава микропрскотина које су објашњене самим механизмом подгризања Si у циљу “ослобађања” микрогредица ове оријентације. SiO_2 микрогредице оријентисане у ⟨110⟩ правцу на (100) Si подлози се “ослобађају” бочним подгри-

зањем Si подлоге и брзина њихове реализације не зависи од дужине микрогредице већ само од њене ширине. Микромостиће од термички депонованог SiO_2 је могуће реализовати анизотропним хемијским нагризањем у разматраним растворима само када су оријентисани у ⟨100⟩ правцу на (100) Si подлози.

(Примљено 19. јула 2006)

REFERENCES

1. K. E. Bean, *IEE Trans. Electrin devices* **ED-25** (1978) 1185
2. M. Madou, *Fundamentals of microfabrication*, CRC Press, Boca Raton, 1997, p. 145
3. N. V. Lavrik, M. J. Sepaniak, P. G. Datskos, *Review of Scientific Instruments* **75** (2004) 2229
4. Y. Zhang, Y.–P. Zhao, *Microsyst. Technol*. **12** (2006) 357
5. W. Fang, H.–C. Tsai, C.–Y. Lo, *Sens. Actuators* **A77** (1999) 21
6. Y. Tang, J. Fang, X. Yan, H.–F. Ji, *Sens. Actuators* **B97** (2004) 109
7. V. Chivukula, M. Wang, H.–F. Ji, A. Khaliq, J. Fang, K. Varahramyan, *Sens. Actuators* **A125** (2006) 526
8. S. Wolf, R. N. Tauber, *Silicon processing for the VLSI era*, Vol. 1, *Process technologies*, Lattice Press, Sunset Beach, California, 1986, p. 407
9. V. Jović, Ž. Lazić, M. Popović, *Proc. XLVII ETRAN Conference*, Čačak, June 6–10, IV, (2004), p. 164
10. C.–J. Kim, J. Y. Kim I, B. Sridharan, *Sens. Actuators* **A61** (1998) 17
11. O. Powell, H. B. Harrison, *J. Micromech. Microen.* **11** (2001) 217
12. E. Steinsland, T. Finstad, A. Hanneborg, *Sens. Actuators* **86** (2000) 73
13. V. Jović, Ž. Lazić, M. Popović, *ICOSECS 4*, Belgrade, July 18–21, Book of Abstracts, (2004), p. 119
14. K. Biswas, S. Das, S. Kal, *Microelectron. J*. **37** (2006) 765
15. A. W. McFarland, M. A. Poggi, L. A. Bottomley, J. S. Colton, *J. Micromech. Microeng*. **15** (2005) 785
16. A. Rawicz, M. Parameswaran, J. M. Chen, *Microelectron. Reliab*. **36** (1996) 1369.

Journal of the Serbian Chemical Society
JSCS@tmf.bg.ac.yu • www.shd.org.yu/JSCS

J. Serb. Chem. Soc. 72 (11) 1139–1153 (2007)
JSCS–3648

UDC 531.3:547.391.1+541.182.41
Original scientific paper

Comparison of the swelling kinetics of a partially neutralized poly(acrylic acid) hydrogel in distilled water and physiological solution

ALEKSANDAR KOSTIĆ[1], BORIVOJ ADNADJEVIĆ[2#], ALEKSANDAR POPOVIĆ[3#] and JELENA JOVANOVIĆ[2#*]

[1]*Faculty of Agriculture, Nemanjina 6, 11080 Zemun, Belgrade,* [2]*Faculty of Physical Chemistry, Studentski trg 16, 11000 Belgrade and* [3]*Faculty of Chemistry, Studentski trg 12–16, 11000 Belgrade, Serbia*

(Received 23 February 2006, revised 19 February 2007)

Abstract: The isothermal kinetics curves of the swelling of a poly(acrylic acid) hydrogel in distilled water and physiological solution at temperatures ranging from 20 to 40 ºC were determined. The possibility of applying both the Fick's kinetics model and kinetics model of the first order chemical reaction to the swelling kinetics of the PAA hydrogel in distilled water and physiological solution were examined. It was found that the possibilities of applying these models were limited. The new model of the kinetics of swelling in distilled water and physiological solution was established. The kinetic parameters (E_a, ln A) for the swelling in distilled water and physiological solution were determined. The decrease of the equilibrium degree of swelling and the saturation swelling rate of the swelling of the PAA hydrogel in physiological solution compared to swelling in distilled water could be explained by the decreased differences in the ionic osmotic pressures between the hydrogel and the swelling medium. The increase of the initial swelling rate in the physiological solution might be caused by an increased density of charges at the network and by an increased affinity of the network towards the water molecules. The increase of the activation energy of the swelling of the PAA hydrogel in the physiological solution is a consequence of its additional "ionic crosslinking".

Keywords: swelling kinetics, kinetics parameters, model, poly(acrylic acid) hydrogel.

INTRODUCTION

Hydrogels are three-dimensional cross-linked polymeric structures which are able to swell in an aqueous environment. Due to their characteristic properties, such as swellability in water, hydrophilicity, biocompatibility, and lack of toxicity, hydrogels have been utilized in a wide range of biological, medical, pharmaceutical and environmental applications.[1,2] In the biomedical field, hydrogels are

Serbian Chemical Society member.
* Corresponding author. E-mail: jelenaj@ffh.bg.ac.yu
doi: 10.2298/JSC0711139K

used in diagnostics, therapeutics and implantable devices (catheters, biosensors, artificial skin, controlled release drug delivery systems and contact lenses). Environmental chemists are interested in utilizing these superabsorbent materials to purify waste water by removing heavy metal ions and organic pollutants.[3,4]

The application of hydrogels could be affected significantly by their swelling properties. The swelling kinetics and equilibrium degree of swelling are influenced by many factors, such as the type of monomers, pH, ionic strength, network structure, hydrophilicity, degree of ionization of functional groups, cross-linking ratio, *etc*. The equilibrium degree of swelling is also a function of the properties of the swelling medium, including the pH and the ionic strength.[5] Ionizable "environmentally sensitive" hydrogel networks are especially attractive because their properties can be controlled not only by changing their molecular structure but also by adjusting external conditions.[5]

Hydrogels of acrylic polymers and their copolymers have been reported as having adjustable swelling kinetics, which display special properties[6] and that the presence of polyacrylic segments in the hydrogels significantly increases their ability to uptake water.[7] It is predictable that, due to the presence of carboxylic acid side groups, the swelling behavior of a poly(acrylic acid) (PAA) hydrogel would be highly dependent on the pH of the surrounding medium.[5] The swelling behavior of copolymeric acrylic hydrogels also depends on the pH value of the solution.[8,9] It was shown that the swelling equilibria are primarily governed by an energy balance between the osmotic pressure within the polymer network and the elastic repulsive force of the network structure.[8] It is known that PAA hydrogels swell significantly in a medium with a pH higher than 5 and that they do not swell significantly in an environment with pH below 4, which is the pH of the stomach. Thus one of the major applications of acrylic acid gels is in sustained gastro-intestinal drug delivery systems.[5,10] A change in pH from 3–6 causes the ionization of the hydrogels and an increase of the degree of swelling.[5]

In the field of hydrogels, research on the kinetics of swelling is important and numerous papers have been published on this topic, dealing with the swelling kinetics of various types of hydrogels. The kinetics of the swelling of hydrogels are most frequently formally described as first order chemical reaction or as a process controlled by diffusion.

The swelling behavior of hydrogels synthesized by γ-radiation cross-linking of poly(acrylic acid) was investigated by swelling the hydrogels in buffered media of pH 4 and 7. It was found that the swelling mechanism was dependent on the pH of the swelling medium and the concentration of PAA during irradiation. Based on the results of Jabbary *et al*., all possible mechanisms of transport of the solution into the gel were observed: Fickian diffusion, a combination of Fickian and anomalous diffusion, anomalous diffusion and diffusion between anomalous diffusion and case-II diffusion.[11]

Completely neutralized poly(acrylic acid) showed the highest degree of swelling in pure water compared to several salt solutions. In this case, free counter ions remain inside the gel to neutralize the fixed charges on the network chains. The driving force of the swelling process is the presence of mobile osmotically active counter ions. When salt is added to the system (1:1 salts; LiCl, NaCl, KCl and CsCl), ions diffuse from the solution into the network. The overall concentration of mobile ions in the gel is higher than before but the difference between ion concentrations inside and outside is reduced. Consequently, the driving force of swelling decreases gradually with increasing salt concentration.[12]

Bearing in mind the possible biomedical applications of PAA hydrogels, the kinetics of the isothermal swelling of a PAA hydrogel in bidistilled water and physiological solution in the temperature range of 20 to 40 °C were investigated. This investigation employed both usual and newly-established methods. The aim of this work was to compare the swelling kinetics of the PAA hydrogel in bidistilled water and a physiological solution and to determine the kinetic parameters (activation energy and pre-exponential factor) for the investigated swelling processes.

EXPERIMENTAL

Materials

Acrylic acid, in glacial form, was obtained from Merck, Darmstadt, Germany and was stored in a refrigerator before use. Sodium persulfate and sodium thiosulfate both p.a. purity, were also supplied by Merck and were used as a redox initiator pair with 30 % hydrogen peroxide, obtained from Zorka–Šabac, Serbia. *N*,*N*'-Methylenebisacrylamide (NMBA), purchased from Merck, Darmstadt, Germany, was used as the cross-linking agent. An activator, ethylenediaminetetraacetic acid (EDTA), p.a., was purchased from Merck, Darmstadt, Germany. Sodium carbonate (Na_2CO_3), p.a., Zorka–Šabac, Serbia, was used for neutralization. All chemicals were used as received. Bidistilled water was used in the polymerization and swelling experiments. Physiological solution was purchased from Hemofarm, Vršac, Serbia.

Synthesis of the partially neutralized poly(acrylic acid) hydrogel

The partially neutralized poly(acrylic acid) hydrogel used in this investigation was synthesized following a procedure based on the simultaneous radical polymerization of acrylic acid and cross-linking the formed poly(acrylic acid) according to the procedure described in a previous investigation,[13] which is described below.

The hydrogel was synthesized under a nitrogen atmosphere in a polymerization reactor equipped with a magnetic stirrer, reflux condenser, nitrogen inlet and thermometer. The monomer solution was prepared from 80 ml of acrylic acid dissolved in 180 ml of distilled water and 0.8 g of NMBA and 0.08 g of EDTA, both dissolved in 60 ml of distilled water. This monomer solution was placed in the reactor, stirred and de-oxygenated with nitrogen gas bubbling through the solution for 60 min. Initiator stock solutions were: sodium persulfate and sodium thiosulfate (both 2.5 g dissolved in 22.5 ml bidistilled water) and hydrogen peroxide, 30 %. After completion of the de-oxygenation, the initiator solutions were added to the monomer solutions: 2.4 ml of sodium persulfate solution, 10 ml of hydrogen peroxide and 1.2 ml of sodium thiosulfate solution. Then, the reaction mixture was slightly warmed up to 50 ºC until the temperature of the reaction mixture dramatically increased (gel point) and it was then left at 50 ºC for a further 4 h. The obtained gel-type product was converted to the Na^+ form (60 %) by neutralizing it with a 3 % solution of Na_2CO_3. Next, the

synthesized hydrogel was thoroughly washed with distilled water. The water was changed 7 times every 5 h or left over night and changed the following morning in order to remove the residual monomers and soluble fraction of the polymer. The hydrogel obtained in bulk was cut into small discs approximately the same size and then dried in an air oven in the temperature regime of 2 ºC min^{-1} up to 105 ºC, to constant mass. The obtained product was stored in a vacuum desiccator before use.

Swelling experiments

To determine the swelling parameters, the samples of xerogels (with diameter of about 0.5 cm and thickness of 1 mm) of average weight of 0.1 g (±5 %) were left to swell in distilled water and a physiological solution at temperatures ranging from 20 to 40 ºC. At the beginning of each experiment, a piece of xerogel was weighed and immersed in an excess of the desired swelling medium to swell. At predetermined time intervals until a constant mass was attained, the swollen gel was removed from the swelling medium and weighed. Since the swollen gels appeared to be fragile, they were put on a grid boat with a mesh size of 1 mm. This technique allowed the polymer to be placed in water and to be weighed without it breaking. Each time the grid boat with the polymer was removed from the swelling medium, it was gently dried with a paper tissue in order to remove excess liquid.

Determination of the degree of swelling

The isothermal degree of swelling (*SD*), defined as the difference between the weight of the swollen hydrogel sample at time *t*, m_t, and the weight of the xerogel sample, m_0, divided by the xerogel weight, was calculated according to Eq. (1) and determined as a function of time:

$$SD[\%] = \frac{m_t - m_0}{m_0} \times 100 \tag{1}$$

The equilibrium degree of swelling, SD_{eq}, is the degree of swelling of the swollen hydrogel at equilibrium, *i.e.*, the hydrogel sample which had reached constant mass, m_{eq}. At least three swelling measurements were performed for each sample and the mean values are reported. The maximal error of the measurements was 0.5 %, *i.e.*, 10 % of the determined *SD*.

The normalized swelling degree, α, is defined as the ratio between the degree of swelling, *SD*, at time, *t*, and the equilibrium swelling degree, SD_{eq}:

$$\alpha = \frac{SD}{SD_{eq}} \tag{2}$$

Physico–chemical characterization of the xerogel

The xerogel was characterized by the following structural properties: density, ρ_{xg}, cross-link density, ρ_c, and the distance between the macromolecular chains, *d*, according to the methods proposed by Gudeman and Peppas.[5]

Xerogel density, ρ_{xg}, determination. The apparent density of the synthesized sample was determined by the picnometry method using *n*-hexane as the non-solvent.

The cross-link density, ρ_c, and the distance between the macromolecular chains were calculated using the following equations:

$$\rho_c = \frac{\rho_{xg}}{M_c} \tag{3}$$

$$d = 0.154 v_2^{1/3} (0.19 M_c)^{1/2} \tag{4}$$

where M_c is the molar mass between the network cross-links and is a nominal value estimated from the initial composition:

$$M_c = \frac{72}{2X} \tag{5}$$

where X is the nominal cross-link ratio (moles of NMBA/moles of acrylic acid in the reaction mixture) and v_2 is the volume fraction of the polymer gel in the equilibrium swollen state at 25 ºC, which was determined as follows (Eq. 6):

$$v_2 = \frac{V_p}{V_{g,s}} \tag{6}$$

where V_p is the volume of the xerogel sample and $V_{g,s}$ is the volume of the gel sample after equilibrium swelling:

$$V_{g,s} = \frac{W_{a,s} - W_{h,s}}{\rho_h} \tag{7}$$

where $W_{a,s}$ is the weight of the polymer after swelling in air, $W_{h,s}$ is the weight of the polymer after swelling in *n*-hexane and ρ_h is the density of *n*-hexane.

RESULTS AND DISCUSSION

The determined basic structural properties of the synthesized PAA xerogel and the nominal cross-linking ratio, X, are given in Table I. Based on the results presented in Table I, it may be concluded that the synthesized xerogel was of a medium cross-linking density and macroporous (pores with average diameter ≥ 50 nm).

The swelling isotherms of the synthesized partially neutralized poly(acrylic acid) (PAA) xerogel in (a) distilled water and (b) physiological solution at temperatures from 20 to 40 °C are shown in Fig. 1.

TABLE I. The basic structural properties of the synthesized PAA xerogel sample and its nominal cross-linking ratio (X) in the reaction mixture

X	ρ_{xg} / kg m^{-3}	M_c / g mol^{-1}	$\rho_c \times 10^4$ / mol cm^{-3}	v_2	d / nm
0.005	994	7200	1.4	0.6	1.02

As can be seen from the results presented in Fig. 1, the swelling isotherm curves are similar in shape at all of the investigated temperatures, both in distilled water and in the physiological solution. Three characteristic regions of the degree of swelling changes with swelling time may be distinguished in all the swelling curves: a linear part, a non-linear part and a saturation range or plateau.

To analyze the influence of temperature on the kinetics curves of swelling, the following specific parameters were used: the initial swelling time, t_{in}, the initial swelling degree, SD_{in}, the initial swelling rate, v_{in}, the equilibrium swelling time, t_{eq}, the saturation swelling rate, v_{eq}, and the equilibrium swelling degree, SD_{eq}. These parameters are defined as follows: t_{in} is the time interval within which the degree of swelling increases linearly with swelling time (from the beginning of the process), SD_{in} is the degree of swelling at the end of this linear increase, v_{in} is the rate of swelling during the initial, linear region of swelling (Eq. (8)):

$$v_{in} = \frac{SD_{in}}{t_{in}} \tag{8}$$

t_{eq} represents the time when the equilibrium swelling degree is first attained, v_{eq} is the saturation swelling rate and is defined as the swelling rate when SD_{eq} is attained for the first time (Eq. 9):

$$v_{eq} = \frac{SD_{eq}}{t_{eq}} \tag{9}$$

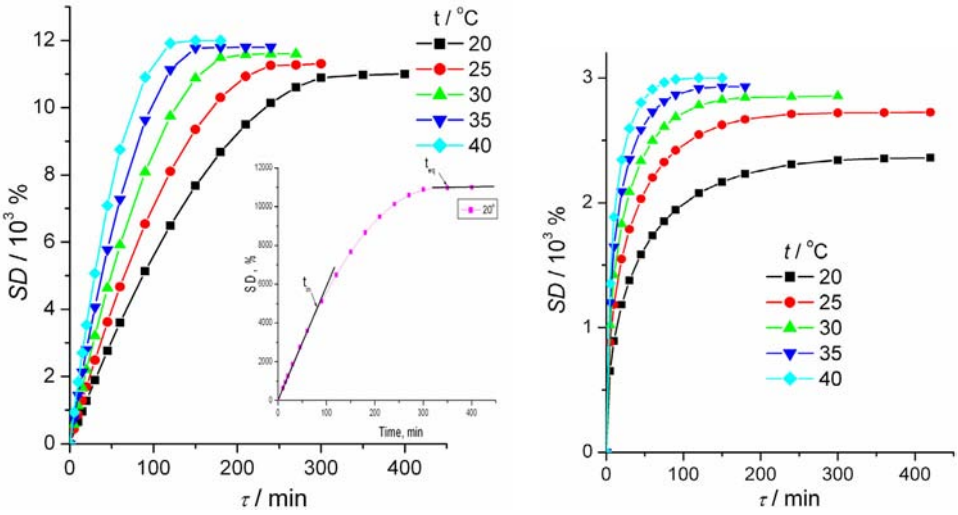

Fig. 1. Swelling isotherms of the PAA hydrogel at different temperatures in (a) distilled water and (b) physiological solution.

The changes of t_{in}, v_{in}, t_{eq}, v_{eq} and SD_{eq} with temperature for the swelling of the investigated hydrogel in water and the physiological solution are presented in Table II.

TABLE II. The influence of temperature on the specific parameters of the swelling kinetics curves: t_{in}, v_{in}, t_{eq}, v_{eq} and SD_{eq}

t / °C	Distilled water					Physiological solution				
	t_{in} min	v_{in} % min^{-1}	t_{eq} min	v_{eq} % min^{-1}	$SD_{eq}\times10^{-3}$ %	t_{in} min	v_{in} % min^{-1}	t_{eq} min	v_{eq} % min^{-1}	$SD_{eq}\times10^{-3}$ %
20	90	55.5	350	31.43	11.0	10.0	89.2	300	7.87	2.36
25	60	78.3	250	45.20	11.3	9.2	118.3	250	10.88	2.72
30	38	105.2	180	64.44	11.6	8.8	141.8	200	14.25	2.85
35	30	133.3	150	78.67	11.8	8.7	164.7	150	19.53	2.93
40	22	182.0	120	100.00	12.0	8.5	188.5	100	30.00	3.00

From the presented results, it is clear that as the temperature of the swelling increased, the initial swelling rate and the equilibrium degree of swelling increased in both investigated systems, while simultaneously, the values of t_{in} and t_{eq} decreased. The values of the initial swelling time and equilibrium degree swel-

ling, at the same swelling temperature, were significantly higher in water (2–9 times) than in the physiological solution. On the contrary however, the calculated values for the initial swelling rate were higher in the physiological solution than in distilled water.

When the kinetics of swelling are determined by the kinetics of penetration of molecules of the swelling medium, Fick's law of diffusion: $SD = kt^{1/2}$,[14,15] could be used as a model for the kinetics of the isothermal swelling.

Plots of the degree of swelling as a function of the square root of time at different swelling temperatures in distilled water and in the physiological solution are presented in Fig. 2. These results deviate significantly from straight lines, both for distilled water and the physiological solution. In fact, it is possible to obtain straight lines only in certain period of swelling. For swelling in distilled water, the middle region of the swelling process gives a straight line for the dependence *SD vs.* $t^{1/2}$, while for swelling in the physiological solution, only the first stages give straight lines. Also, the shapes of the obtained curves of the process in water and in the physiological solution differ significantly from each other. These results imply that the so-called Fickian type of solvent diffusion into the hydrogel is not the dominant factor influencing the swelling kinetics of the hydrogel. They also imply that the swelling mechanisms in water and in the physiological solution are probably different.

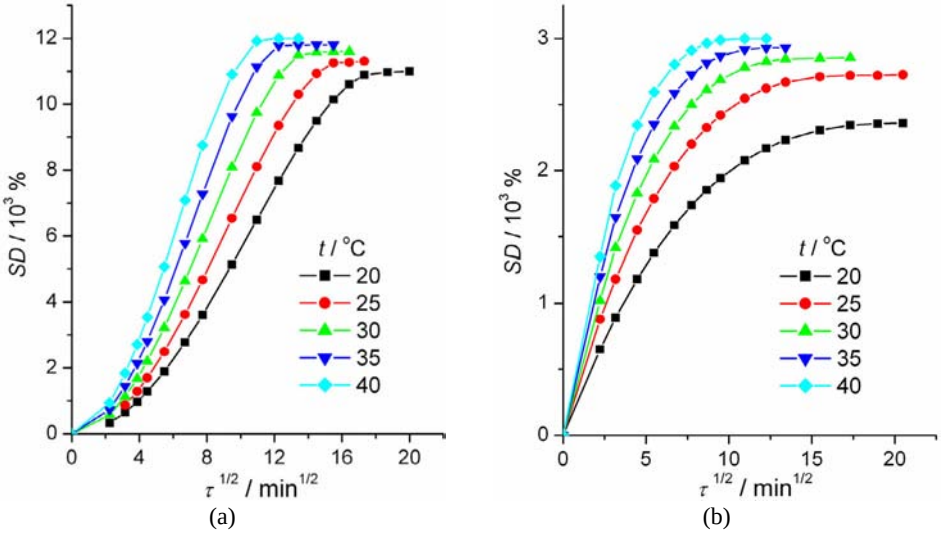

Fig. 2. Plots of the degree of swelling as a function of the square root of time in (a) distilled water and (b) physiological solution.

If the kinetics of swelling is determined by diffusion of the network, the isothermal swelling kinetics of the gel could be described by the Eq. (10):

$$\ln \frac{SD_{eq}}{SD_{eq} - SD} = k\,t \tag{10}$$

i.e., the plots of ln (SD_{eq}/(SD_{eq}–SD)) *vs.* t give straight lines.

The dependences of ln (SD_{eq}/(SD_{eq}–SD)) on time for the swelling of the investigated hydrogel at the investigated temperatures are presented in Fig. 3, from which it can be seen that the plots of ln (SD_{eq}/(SD_{eq}–SD)) as a function of time give straight lines only in parts of both of the investigated swelling processes.

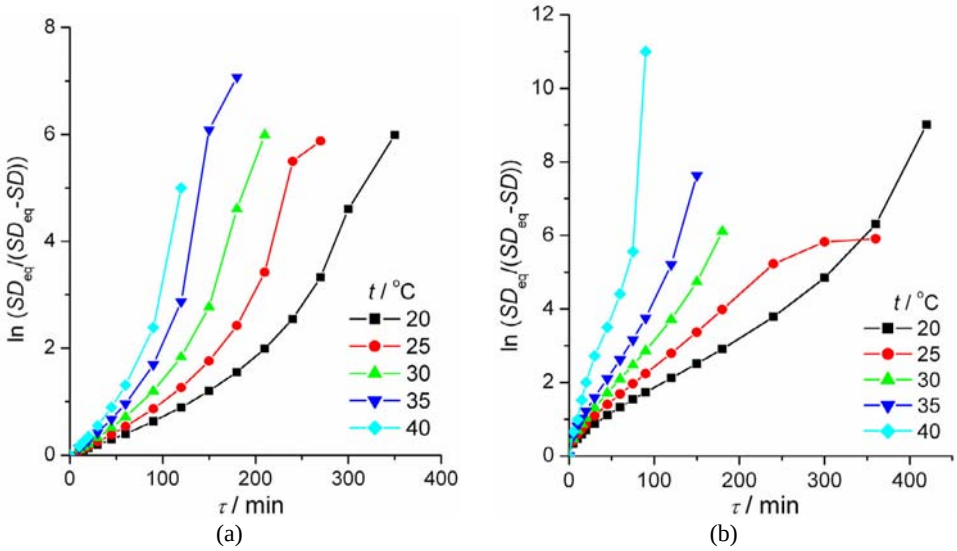

Fig. 3. Plot of ln (SD_{eq}/(SD_{eq}–SD)) *vs.* time in (a) distilled water and (b) physiological solution.

Bearing in mind that the isothermal swelling kinetics, both in water and in the physiological solution may be described by the actually known models of swelling only over limited time intervals, an attempt was made to investigate the possible applicability of a new model for swelling kinetics. The choice of the new model is based on the so-called "model-fitting method" which is widely used to establish the reaction models for reactions occurring in the solid state.[16]

According to this procedure, the best choice of the approximate reaction model of the swelling process is achieved by comparing (both graphically and analytically) the shapes of the function: $\alpha_e = f(t^*_{e,red})$ of the investigated systems to the shape of the function $\alpha = f(t^*_{red})$ of common reaction kinetics models for heterogeneous processes, where, α is the normalized degree of swelling and t^*_{red} is the reduced time:

$$t^*_{red} = t_\alpha / t_{0.9} \tag{11}$$

where t_α is the swelling time which corresponds to the normalized degree of swelling α, while $t_{0.9}$ is the swelling time which corresponds to $SD = 0.9SD_{eq}$.

The sets of the common kinetics reaction models which were used to analyze the investigated swelling kinetics models are presented in Table III.[17,18]

TABLE III. The set of kinetics models used for the determination of the kinetics model of the swelling of the PAA hydrogel

Model	Reaction mechanism	General expression of the kinetics model, $f(\alpha)$	Integral form of the kinetics model, $g(\alpha)$
P1	Power law	$4\alpha^{3/4}$	$\alpha^{1/4}$
P2	Power law	$3\alpha^{2/3}$	$\alpha^{1/3}$
P3	Power law	$2\alpha^{1/2}$	$\alpha^{1/2}$
P4	Power law	$2/3\alpha^{-1/2}$	$\alpha^{3/2}$
R1	Zero-order (Polany–Winger equation)	1	α
R2	Phase-boundary controlled reaction (contracting area, *i.e.*, bidimensional shape)	$2(1-\alpha)^{1/2}$	$[1-(1-\alpha)^{1/2}]$
R3	Phase-boundary controlled reaction (contracting volume, *i.e.*, tridimensional shape)	$3(1-\alpha)^{2/3}$	$[1-(1-\alpha)^{1/3}]$
F1	First-order (Mampel)	$(1-\alpha)$	$-\ln(1-\alpha)$
F2	Second-order	$(1-\alpha)^2$	$(1-\alpha)^{-1}-1$
F3	Third-order	$(1-\alpha)^3$	$0.5[(1-\alpha)^{-2}-1]$
A2	Avrami–Erofe'ev	$2(1-\alpha)[-\ln(1-\alpha)]^{1/2}$	$[-\ln(1-\alpha)]^{1/2}$
A3	Avrami–Erofe'ev	$3(1-\alpha)[-\ln(1-\alpha)]^{2/3}$	$[-\ln(1-\alpha)]^{1/3}$
A4	Avrami–Erofe'ev	$4(1-\alpha)[-\ln(1-\alpha)]^{3/4}$	$[-\ln(1-\alpha)]^{1/4}$
D1	One-dimensional diffusion	$1/2\alpha$	α^2
D2	Two-dimensional diffusion (bidimensional particle shape)	$1/[-\ln(1-\alpha)]$	$(1-\alpha)\ln(1-\alpha)+\alpha$
D3	Three-dimensional diffusion (tridimensional particle shape), Jander equation	$3(1-\alpha)^{2/3}/2[1-(1-\alpha)^{1/3}]$	$[1-(1-\alpha)^{1/3}]^2$
D4	Three-dimensional diffusion (tridimensional particle shape), Ginstling–Brounshtein	$3/2[(1-\alpha)^{-1/3}-1]$	$(1-2\alpha/3)-(1-\alpha)^{2/3}$

Fig. 4 shows the plots $\alpha_e = f(t^*_{e,red})$ for the theoretical reaction models presented in Table III (solid curves) and the experimental plots $\alpha_e = f(t^*_{e,red})$ for the swelling of the employed partially neutralized poly(acrylic acid) hydrogel in distilled water and in physiological solution, 4a and b, respectively.

Based on the results presented in Fig. 4, it may be concluded that the isothermal swelling kinetics of PAA in distilled water could be described with the so-called kinetics model of "contracting area" which is characteristic for phase-boundary controlled reactions, of bidimensional shape.[19] Furthermore, the isothermal swelling kinetics in the physiological solution could be described by the so-called kinetics model of tridimensional diffusion, which is characteristic for tridimensional shaped particles (Jander equation).[20] This means that the following expressions are, respectively, valid:

$$1-(1-\alpha)^{1/2} = k_m t \quad (12)$$

$$[1-(1-\alpha)^{1/3}]^2 = k_m t \quad (13)$$

where k_m is the model rate constant.

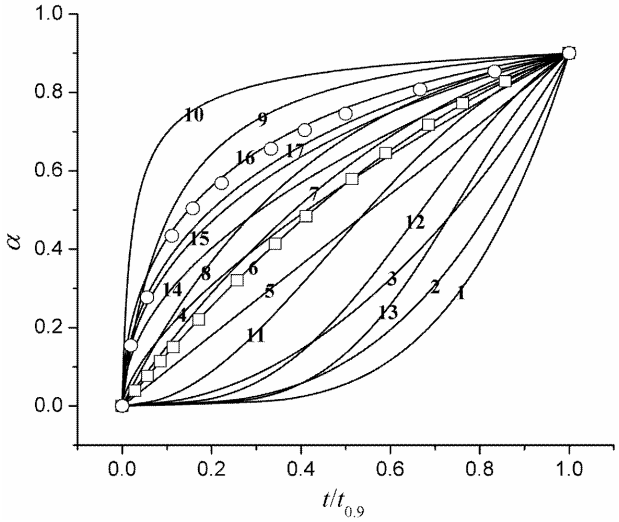

Fig. 4. Plot of $\alpha_e = f(t^*_{e,red})$ for swelling in distilled water (□) and in physiological solution (○) and the theoretical models (solid lines).

Fig. 5 presents the dependence of $1–(1–\alpha)^{1/2}$ on time for the swelling of PAA in distilled water at the investigated temperatures.

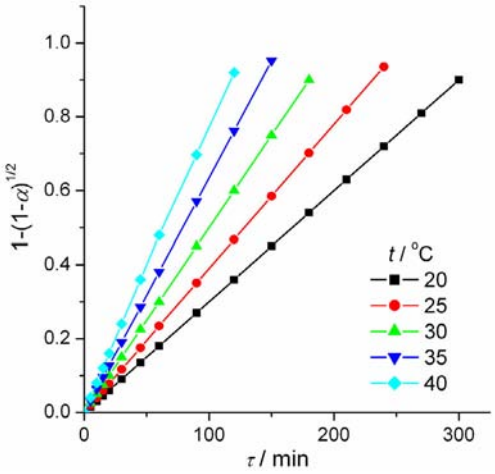

Fig 5. Plot of $1–(1–\alpha)^{1/2}$ *vs.* time for swellling in distilled water at the investigated temperatures.

Over a very wide range of "periods of applicability" ($P \geq 90$ %) at all the investigated temperature in distilled water, the dependence $1–(1–\alpha)^{1/2}$ *vs.* time gives a straight line. The values of the model swelling rate constants (k_m) were determined from the slopes of the lines obtained according to Eq. (12), which are presented in Fig. 5. These values are shown in Table IV.

The dependences of $1–(1–\alpha)^{1/3}$ on the square root of time at the varying investigated temperatures are in Fig. 6 shown for the swelling process of PAA in the physiological solution.

TABLE IV. The temperature changes of model swelling rates constants (k_m) and their periods of applicability (P) for the swelling of the PAA hydrogel in distilled water and physiological solution

t / °C	Distilled water		Physiological solution	
	P / %	k_m / 10^{-3} min^{-1}	P / %	k_m / 10^{-3} min^{-1}
20	0–99	3.0	0–100	2.1
25	0–94	3.9	0–100	3.1
30	0–90	5.0	0–100	4.2
35	0–95	6.4	0–100	5.7
40	0–92	7.8	0–98	7.7

Over a very wide range of "periods of applicability" ($P \geq 90$ %), namely for the entire range at all of the investigated temperatures in the physiological solution, the dependence $1–(1–\alpha)^{1/3}$ on the square root of time gives a straight line. The swelling rate constants (k_m) of the model were determined based on the slopes of the lines obtained according to Eq. (13), which are presented in Fig. 6. These values are also shown in Table IV.

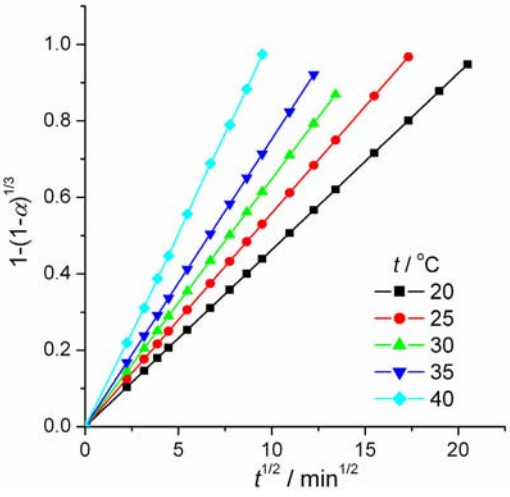

Fig 6. A plot of $1–(1–\alpha)^{1/3}$ *versus* the square root of time for swelling in the physiological solution at the investigated temperatures.

Based on the results presented in Table IV, it is easy to observe that as the temperature of swelling increases, the swelling rate constants (k_m) of the model also increases. As the swelling rate constants calculated for the determined "periods of applicability" (P) using the applied models exponentially increase with increasing temperature, it is possible to determine the kinetic parameters: activation energy (E_a) and pre-exponential factor ($\ln A$) for the applied kinetic models using the well-known Arrhenius equation.

The results of the determined values of the kinetic parameters (E_a and $\ln A$) determined for the reaction models and their corresponding "periods of applicability" (P) in distilled water and the physiological solution are summarized in Table V.

TABLE V. The values of the kinetics parameters obtained using the different kinetics models

Model	Distilled water			Physiological solution		
	P / %	E_a / kJ mol^{-1}	ln(A / min^{-1})	P / %	E_a / kJ mol^{-1}	ln(A / min^{-1})
Initial rate	0–(30–46)	44.36	22.24	0–(37.7–70)	27.9	16.01
Fickian diffusion	22–82	21.68	15.69	0–(37–62)	27.7	17.06
First order	0–(50–70)	32.07	8.38	0–(50–78)	49.6	16.14
Model	0–(9–95)	35.01	8.60	0–(99–100)	48.3	13.7

For all of the swelling kinetics models examined, the calculated kinetic parameters for the swelling of PAA hydrogels in the physiological solution are higher than the calculated values for the same process in distilled water.

The values of the kinetic parameters for both investigated processes, determined by the newly established models and those of the first order kinetics model, are mutually comparable and differ from one another by 5–10 %. The numerical values of the kinetics parameters determined using Fick's kinetics model are significantly lower. The established changes of the swelling kinetics model and the swelling kinetics parameters in physiological solution when compared to those obtained with distilled water imply that the swelling mechanism in the physiological solution when compared to distilled water is changed. Based on the obtained results, it may be proposed that the swelling kinetics of PAA hydrogel in distilled water are caused by the rate of two-dimensional movement of the reactive interface, which is formed during the interaction of the polymer network with the molecules of the swelling medium. On the contrary, the isothermal swelling kinetics in physiological solution can be described by the kinetics model of three-dimensional movement of the reactive phase boundary.[21]

According to Flory's theory,[22] the degree of swelling of a gel in a specific medium is a function of its characteristic properties (cross-link density, affinity towards the molecules of the swelling medium, concentrations of the bonded charges, degree of ionization of the functional groups, *etc*.), as well as of the characteristics of the swelling medium (pH, ionic strength, valences of the opposite ions). This theory simply explains the established decrease of both the equilibrium degrees of swelling and the saturation swelling rate at all applied temperatures in the physiological solution when compared to those in distilled water. The penetration of the physiological solution into the gel, due to the higher content of cations, leads to an increase in the Na^+ concentration onto the gel, as well as to an increase of the osmotic pressure in the gel, *i.e*., to a decrease in the difference in the osmotic pressure between the gel and the swelling medium,[23] which leads to decrease of SD_{eq} and v_{eq}.

The established increase of the rate of the initial swelling in the physiological solution compared to that in distilled water can be explained as a consequence of the increased concentration of the charges bonded to the network and

the affinity of the network to the molecules of the swelling medium compared to the molecules of distilled water. In the physiological solution (pH 6.4) the network's functional carboxylic groups of the network of the PAA hydrogel are completely ionized because the pK_a of PAA is 4.6. Thus, increasing the concentration of COO^- groups, *i.e.*, the fixed charges, leads to an increase of the affinity towards the molecules of the swelling medium, which in turn leads to electrostatic repulsion. This causes the initial swelling rate to increase in the physiological solution more than in distilled water (note: this comparison concerns two different time intervals. Approximately 10 min for the swelling in the physiological solution and about 80–100 min in distilled water). If the activation energy of the swelling process is equal to the energy necessary to cause elastic shrinkage of the hydrogel network, the established increase of the activation energy of the swelling process in the physiological solution compared to the one in distilled water, can be explained by the existence of so-called "ionic cross-linking"[23] in the physiological solution. That is, "ionic cross-linking" occurs due to the interaction of Na^+ ions with COO^- (of the network), which mainly occurs at the surfaces and makes them stronger, which additionally decreases the flexibility of the network.

The established changes of the swelling kinetics models in the physiological solution compared to that in distilled water, are in accordance with the theoretical and mathematical prediction of Wang and co-workers.[24] The hypothesis was postulated on the theory of gel swelling kinetics, which is based on the collective motions of both the network and swelling medium during the swelling process, *i.e.*, the diffusion motion of the "adsorption complex" formed from the network and diffusion of the swelling medium. According to their theory, the swelling medium moves together with the network, the swelling medium rate is the same as the network rate and the motion of the polymer network of a gel during the course of swelling is described by an equation called the "collective diffusion equation".[24] When the rate of axial movement of the reactive interface is higher than the rate of radial movement of the reactive interface (as is the case for PAA hydrogels swelling in water) then for higher degrees of swelling, the reactive interface increases because the rate of network shrinkage is lower than the rate of penetration of the molecules of the swelling medium. On the contrary, when the rates of the axial and radial movement of the reactive interface are identical, as is the case for a PAA hydrogel swelling in the physiological solution, for higher degrees of swelling, the reactive interface and reactive boundary volume will be diminished and, hence, the rate of swelling of the hydrogel will be decreased.

CONCLUSIONS

The isothermal swelling kinetics of a poly(acrylic acid) hydrogel in distilled water and physiological solution were described by Fick's kinetics model and the kinetics model of first order chemical reaction only during limited stages of the process.

The isothermal swelling kinetics of the PAA hydrogel in distilled water could be described by the so-called kinetics model of "contracting area", while the isothermal swelling kinetics in the physiological solution could be described by the so-called kinetics model of "tridimensional diffusion".

The decrease of the equilibrium degree of swelling and the saturation swelling rate of the PAA hydrogel swelling in the physiological solution compared to the swelling in distilled water could be explained by the decreased differences in the ionic osmotic pressures between the hydrogel and the swelling medium.

The increase of the initial swelling rate in the physiological solution might be caused by an increased density of charges at the network and by the increased affinity of the network towards the water molecules.

The increase of the activation energy of the PAA hydrogel swelling in the physiological solution is explained as a consequence of the additional "ionic cross-linking".

Acknowledgements: The Ministry of Science of Serbia supported this investigation through project 142025G.

И З В О Д

ПОРЕЂЕЊЕ КИНЕТИКЕ БУБРЕЊА ХИДРОГЕЛА ДЕЛИМИЧНО НЕУТРАЛИСАНЕ ПОЛИ(АКРИЛНЕ) КИСЕЛИНЕ У ДЕСТИЛОВАНОЈ ВОДИ И ФИЗИОЛОШКОМ РАСТВОРУ

АЛЕКСАНДАР КОСТИЋ[1], БОРИВОЈ АДНАЂЕВИЋ[2], АЛЕКСАНДАР ПОПОВИЋ[3] и ЈЕЛЕНА ЈОВАНОВИЋ[2]

[1]Пољопривредни факултет, Немањина 6, 11080 Земун, Београд, [2]Факултет за физичку хемију, Студентски трг 12–16, 11000 Београд и [3]Хемијски факултет, Студентски трг 12–16, 11000 Београд

У раду су испитиване изотермалне кинетичке криве бубрења хидрогела делимично неутралисане поли(акрилне) киселине у дестилованој води и физиолошком раствору у температурном опсегу од 20 до 40 °C. Испитивана је могућност примене Фиковог кинетичког модела као и кинетике и реда хемијских реакција на кинетику бубрења полиакрилног хидрогела.Утврђено је да су могућности за њихову примену врло ограничене. Из тих разлога примењен је нови модел кинетике бубрења. Одређени су кинетички параметри (E_a, $\ln A$) за процесе бубрења у дестилованој води и физиолошком раствору. Смањење равнотежног степена бубрења и сатурационе брзине бубрења хидрогела делимично неутралисане поли(акрилне) киселине у физиолошком раствору у односу на дестиловану воду може се објаснити смањењем разлике у јонском осмотском притиску између хидрогела и медијума за бубрење. Повећање иницијалне брзине бубрења у физиолошком раствору у односу на дестиловану воду проузроковано је повећањем густине наелектрисања на полимерној мрежи и повећаним афинитетом према молекулима воде. Повећање енергије активације хидрогела делимично неутралисане поли(акрилне) киселине при бубрењу у физиолошком раствору се објашњава додатним "јонским умрежењем" хидрогела у физиолошком раствору.

(Примљено 23. фебруара 2006, ревидирано 19. фебруара 2007)

REFERENCES

1. N. A. Peppas, A. G. Mikos, *Hydrogels in Medicine and Pharmacy*, N. A. Peppas, Ed., CRC Press, Boca Raton, Florida, Vol. I, 1986, p. 2

2. B. D. Ratner, A. S. Hoffman, *Hydrogels for Medical and Related Applications*, B. D. Ratner. Ed., Andrade and Andrade, American Chemical Society, Washington, DC, 1976, p. 1
3. D. R. Kioussis, P. Kofinas, *Polymer* **46** (2005) 9342
4. H.A.Essaway, H.S.Ibrahim. *React. Funct. Polym.* **61** (2004) 421
5. L. Gudman, N. A. Peppas , *J. Appl. Polym. Sci.* **55** (1995) 919
6. C. Elvira, J. F. Mano, J. S. Román, R. L. Reis, *Biomaterials* **23** (2002) 1955
7. S. J. Kim, K. J. Lee, S. I. Kim, *React. Funct. Polym*. **55** (2003) 69
8. J. P. Baker, H. W. Blanch, J. M. Prausnitz, *J. Appl. Polym. Sci*. **52** (1994) 783
9. E. Jabbary, S.Nazary, *Eur. Polym. J*. **36** (2000) 2685
10. H. Cheng Chiu, Y. Fong Lin, S. Hsiu Hung, *Macromolecules* **35** (2002) 5235
11. N. A. Peppas, S. Wright, *Macromolecules* **29** (1996) 8798
12. F. Horkay, I. Tasaki, P. Basser, *Biomacromolecules* **1** (2000) 84
13. J. Jovanović, B. Adnadjević, S. Ostojić, M. Kićanović, *Mater. Sci. Forum* **453**–**454** (2004) 543
14. I. Katime, J. L. Velada, R. Novoa, E. Diaz de Apodaca, J. Puig, E. Mendizabal, *Polym. Int*. **40** (1996) 281
15. H. Omidian, S. A. Hashemi, P. G. Sammes, I. Meldrum, *Polymer* **26** (1998) 6697
16. M. E. Brown, D. Dollimore, A. K. Galway, *Comprehensive Chemical Kinetics*, Vol. 22, Elsevier, Amsterdam, 1980
17. S. Vyzovkin, C. A. Wight, *Thermochim. Acta* **340–341** (1999) 53
18. A. Khawam, D. R. Flanagan, *Thermochim. Acta* **429** (2005) 93
19. S. F. Hilbert, *J. Br. Ceram. Soc* **6** (1969) 11
20. A. Ginstling, M. Brounshtein, *J. Appl. Chem. USSR* **23** (1950) 1327
21. Y. Li, T. Tanaka, *J. Chem. Phys*. **92** (1990) 1365
22. P. J. Flory, *Principles of Polymer Chemistry*, P. J. Flory, Ed., Cornell University Press, Ithaca, NY, 1953
23. G. R. Mahdavinia, A. Pourjavadi, H. Hosseeinzadeh, M. J. Zohuriaan, *Eur. Polym. J*. **40** (2004) 1399
24. C. Wang, L. Yong, H. Zhibing, *Macromolecules* **30** (1997) 4727.

Journal of the Serbian Chemical Society
JSCS@tmf.bg.ac.yu • www.shd.org.yu/JSCS

J. Serb. Chem. Soc. 72 (11) 1155–1169 (2007)
JSCS–3649

UDC 547.313.2+546.76–31+66.095.26
Original scientific paper

The charge percolation mechanism and simulation of Ziegler–Natta polymerizations. Part VI. Mechanism of ethylene polymerization by supported chromium oxide

DRAGOSLAV STOILJKOVIĆ[1]*#, BRANKA PILIĆ[1], MIŠA BULAJIĆ[2], NEBOJŠA ĐURASOVIĆ[2] and NIKOLAJ OSTROVSKI[3]

[1]*Faculty of Technology, University of Novi Sad, Bul. Cara Lazara 1, 21000 Novi Sad,* [2]*HIP-Petrohemija, 26000 Pančevo and* [3]*HIPOL, 25250 Odžaci, Serbia*

(Received 27 October 2006, revised 13 June 2007)

Abstract: Despite intensive research over the last 50 years, many questions concerning ethylene polymerization by supported chromium oxide are still unanswered. Hence, the very fundamental issues of this polymerization are discussed in this paper. It is shown that a charge percolation mechanism (CPM) of olefin polymerization by Ziegler–Natta transition metal complexes, recently proposed by us, can give the answers in this case, too.

Keywords: Ethylene polymerization, Phillips CrO_x/SiO_2, charge percolation mechanism.

INTRODUCTION

Ethylene polymerization by silica supported chromium oxide was discovered some fifty years ago and has attracted a great deal of academic and industrial research.[1] It is generally believed that the insertion mechanism[2,3] of Ziegler–Natta (ZN) polymerization can also be applied in this case. Despite the very extensive research, however, there are still many open questions:[1,4–8]

1. What is the oxidation state and structure of the active center?
2. What is the mechanism of initiation?
3. What is the mechanism of polymerization?
4. What is the physico–chemical state of the Cr species at the silica?
5. How to explain the polymerization kinetics, particularly the occasional appearance of an induction period?
6. How to explain the origin of the structure and very broad molecular weight distribution (MWD) of PEHD?
7. What is the role of silica and how to correlate its properties with the results of polymerization?

* Corresponding author. E-mail: dragos@uns.ns.ac.yu
# Serbian Chemical Society member.
doi: 10.2298/JSC0711155S

The same questions have been asked since the 1950s, when Hogan and Banks claimed that the Phillips catalysts "is one of the most studied and yet controversial system". In 1985, McDaniel[8] stated, "we seem to be debating the same questions posed over thirty years ago, being no nearer to a common view". Nowadays, in a review[4] published in 2005, it is stated that "it is interesting to underline that although in the last two decades a lot of progress has been made, no unifying picture has yet been achieved."

Fifty years – the same open questions, the same "Whats" and "Hows"!

Hence, at the beginning of this article, the fundamental facts and the presumptions trying to find out what is wrong will be re-examined. Then, a recently-proposed charge percolation mechanism (CPM) of olefin polymerization in presence of transition metal compounds[9–13] will be applied. The aim of this work was to show that the CPM also can be applied to explain ethylene polymerization by CrO_x supported on SiO_2 or some other supports. In a subsequent article[14] of this series, the most important and well-known empirical facts will be presented and explained by the CPM.

EMPIRICAL FACTS AND CONTROVERSIES OF CURRENT EXPLANATION

To find a way out of the deadlock it is necessary to return to the very beginning and to analyze the process in the most fundamental manner. There is no doubt that the Phillips process includes three basis participants, *i.e.*, monomer (ethylene) molecules, active centers (based on chromium) and the support (silica). The crucial question is: Why each participant (ethylene, chromium and support) enters into the process?

Ethylene polymerizability

Concerning ethylene, there is an excess of free energy stored in the dynamic movement of π-electrons, *i.e.*, four electrons are squeezed between two carbon atoms separated by 0.133 nm. (Hence, the ethylene molecule has a quadrupole moment, *i.e.*, the C–H bonds are partially polarized. The dipole moment of the C–H bond is 3.5×10^{-30} C m, *i.e.*, 1.05 D.[15] The partially positive charges are on the H atoms, while the partially negative charges are on and between the C atoms.) The second issue is the completely restricted rotation around the C=C bond. There is a thermodynamic tendency to liberate the free energy by polymerization, *i.e.*, to transform the double bonds into the single σ-bonds, which contain the only two electrons between the two more separated carbon atoms (0.154 nm). Simultaneously, rotation around the C–C bonds would be enabled. The negative change of enthalpy ($\Delta H = -92.7$ kJ mol^{-1}),[16] *i.e.*, the heat evolved in that process, is the thermodynamic "driving force" of the polymerization. To achieve this, however, it is necessary to sacrifice the relatively free movement of the ethylene molecules and to replace it by the segmental motion of the macromolecular chain. Hence, there is a large negative change of entropy of polymerization

($\Delta S = -0.14$ kJ mol^{-1} K). Despite this, the change in free energy even at atmospheric pressure and 500 K is negative, *i.e.*, $\Delta G = \Delta H - T\Delta S = -22.9$ kJ mol^{-1}. Hence, the high negative entropy change of polymerization is not a "limiting force" of the polymerization from the thermodynamic but from the kinetics standpoint.[16] Hence, it is necessary to achieve such polymerization conditions which enable both a negative change of free energy ($\Delta G = \Delta H - T\Delta S < 0$) and a less negative change of entropy. Ethylene alone can satisfy these requirements and can polymerize by the free radical mechanism only at extremely high pressures. Otherwise, it cannot polymerize without the aid of transition metal active centers and the help of a support which provides the conditions necessary for polymerization.[17]

Oxidation states of chromium active centers

But, why does chromium enter into the process and how does it help the ethylene molecules to polymerize? Let us consider the current explanation using the insertion mechanism.[1–3] Even the initiation reaction is not fully understood; it is believed that initially some alkylated chromium active centers are formed, *i.e.*, initial Cr−R species have to be formed. Whatever is the oxidation state of the active chromium centers, there is at least one empty d-orbital (□) on an alkylated chromium atom (□Cr–R). The chromium has a necessity to fill the empty orbital with electrons. According to the current explanation, propagation of the polymer chain consists of two steps. In the first one, an ethylene molecule (Et) is coordinated to a chromium atom supplying π-electrons to the empty orbital (Et···Cr–R). It seems that the chromium atom has filled the empty orbital. In the second step, however, it is proposed that the coordinated ethylene molecule escapes from the just filled chromium orbital and inserts itself into the Cr–R bond making the chromium orbital empty again (□Cr–Et Cr–R). It is believed that these two steps are repeated again and again, several thousands times. It is evident that the chromium active center is circumvented and deceived, again and again, several thousands times! Each time an ethylene molecule has fulfilled its tendency to polymerize, but the chromium active center has never filled the orbital! A similar insertion mechanism and quite similar open questions exist in the interpretation of the Phillips process, such as in the case of ZN polymerization of olefins.

In addition to the empty orbital, Cr atoms have a diversity of oxidation state. Various chromium compounds are used as precursors for the preparation of chromium active centers: oxides, acids, sulfates, acetates, *etc*. In the most cases, initially almost all Cr atoms of some precursor are in the same oxidation state, *i.e.*, Cr(III) or Cr(VI), sometimes Cr(II). After impregnation onto a support, the thermal treatment and activation in the presence of oxygen or an inert medium, and possible reduction by hydrogen or carbon monoxide, a diversity of Cr oxidation state is achieved. A typical Phillips catalyst with 1 wt. % Cr supported by silica, after calcination in dry air, shows the existence of mixed oxidation states: 70.4 %

Cr(VI) and 29.6 % Cr(III).[6] Further changes in the Cr oxidation states occur on addition of ethylene, *i.e.*, Cr(II), Cr(III), Cr(IV), Cr(V) and Cr(VI) oxidation states have been found.[4,6,7,18–29] Initially formaldehyde and ethylene oligomers are produced.[4,6,7] According to the proposed mechanism[7] (Fig. 1), some of the Cr(VI) atoms are transformed into the unstable transient Cr(IV), then reduced to Cr(II) species (steps 1 through 4, producing the species A, B, C, D and E). Starting from 70.4 % Cr(VI) and 29.6 % Cr(III), after ethylene addition, it was found that the fraction of Cr(VI) decreased to 47.8 %, while the fractions of Cr(III) and Cr(II) increased to 39.3 % and 12.9 %, respectively. It is believed that the increase of Cr(III) species is due to the interaction between Cr(II) and Cr(VI) species (step 5, producing F). It has been confirmed that surface Cr species in the oxidation states Cr(III) and Cr(V) showed no direct relationship with the polymerization activity and thus could be ruled out as the active Cr precursor.[25]

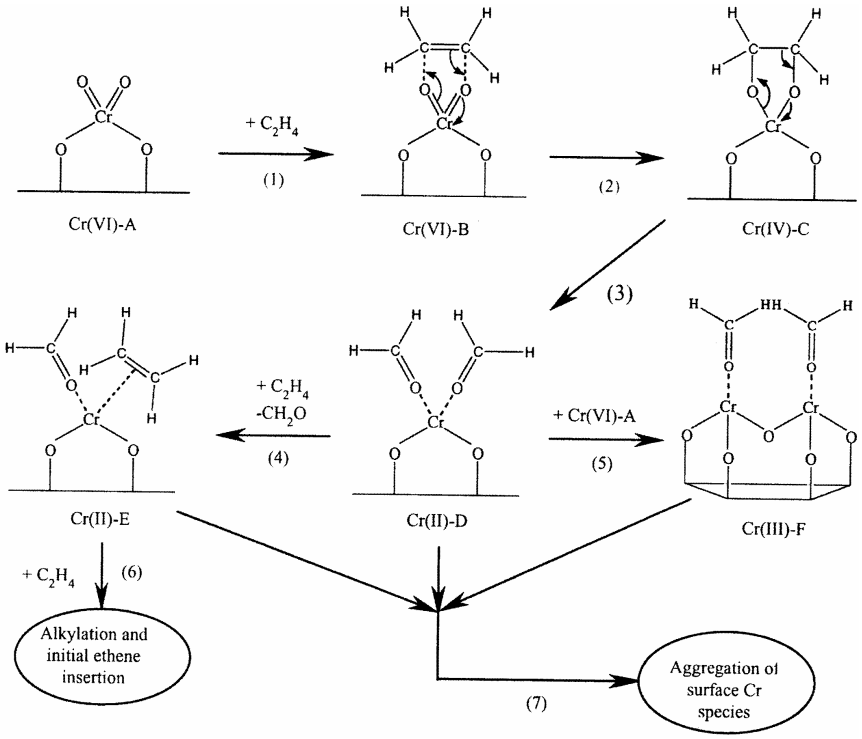

Fig. 1. Plausible mechanism of the reactions occurring on the CrO_x/SiO_2 catalyst engaged in the induction period through interaction with ethylene.[7]

In a case of Cr precursor treatment with CO, most of Cr atoms are reduced to the oxidation state Cr(II).[4,8,18–24] In the presence of ethylene, the oxidative addition of one, two or three ethylene molecules to Cr(II) species gradually converts them into various alkylated Cr(IV) species (Fig. 2).[4,26,28,29]

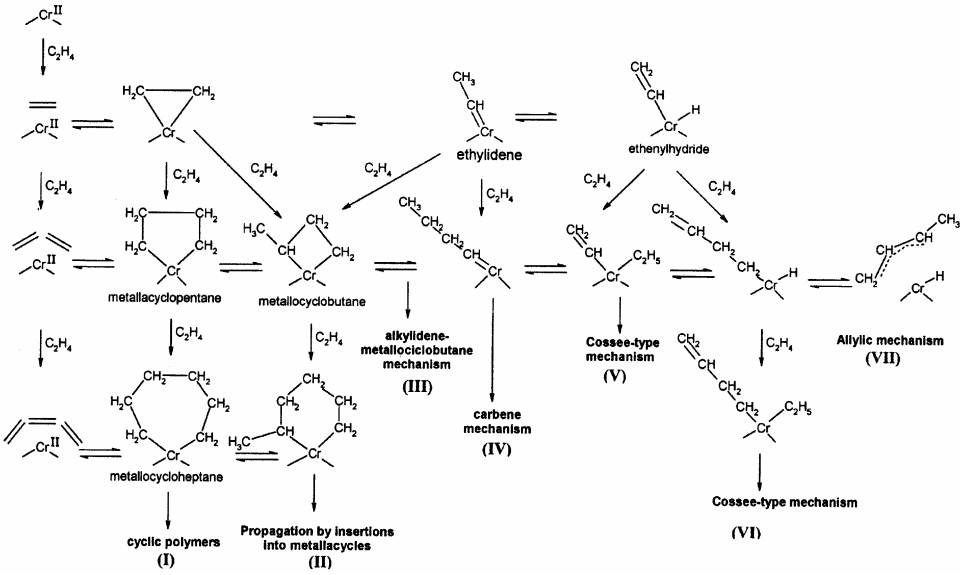

Fig. 2. Initiation mechanisms proposed for CO reduced Cr/SiO_2 precursors.[4]

Generally, starting from a relatively homogeneous oxidation state of Cr atoms in some precursor, a significant diversification of the oxidation state is achieved by the processes of impregnation, thermal treatment, activation and by the initial interaction with ethylene. The catalysts consist of Cr atoms which are heterogeneous in respect to their oxidation state. There is a tendency of chromium to re-homogenize its oxidation state and to stabilize itself to the oxidation state Cr(III). This happens by ethylene polymerization. The initially formed unstable Cr(II) and Cr(IV) species are transformed to the more stable Cr(III) species by simultaneous polymerization of ethylene to a macromolecular chain. Hence, during ethylene polymerization by Cr(II) precursors, the fraction of Cr(II) decreases while the fraction of Cr(III) increases.[4] Chromium active centers are deactivated, *i.e.*, stabilized, simultaneously with ethylene polymerization. Deactivation of the active centers and ethylene polymerization are mutually interdependent acts. Both of them are possible, however, only in the presence of some support (carrier).

Relaxation of silica surface strain by chromium and ethylene

"Usually the carrier does play an essential role, because without it such (chromium) compounds rarely exhibit any activity... In fact, neither (chromium) species is very active for ethylene polymerization until it has been supported on a carrier".[8] The catalyst support not only acts as a dispersing agent for the active Cr centers, but its properties have also a dramatic effect on the polymer characteristics. The most important factors are pore volume, pore size and surface area.

The crucial question is: Why a support enters into the process? During the thermal treatment and the calcination, silica dehydroxylation occurs, resulting in the formation of surface strained siloxane groups.[4] It has been explained that the hydroxyl and siloxane concentrations change with the thermal treatments and that they influence the silica surface strain. It has been noted that the grafting of Cr(II) ions decreases the silica surface strain. The role of surface strain in the Cr(II)/SiO_2 system activated at high temperature in influencing the activity is not completely clarified, even if the more recent information suggests that the effect is not negligible.[4] In any case, it is evident that Cr precursors reacting with hydroxyl groups help silica to reduce the strain.

The ethylene adsorption has a quite similar effect: "We have to consider that the adsorption of molecules is always associated with a surface relaxation phenomenon".[4] It was confirmed experimentally that the surface of the support and the pore volume were decreased significantly by ethylene adsorption.[30]

Importance of ethylene adsorption for polymerization

It is well know that ethylene and CO, as well as some other compounds are adsorbed on silica even in the absence of chromium or any other transition metal. Newalker *et al*.[31] reported the adsorption of light hydrocarbons on HMS type mesoporous silica (980 $m^2\ g^{-1}$, the pore size distribution was centered at about 20 nm) at pressures up to 1000 mm Hg (at 30 and 50 °C, respectively): ethane 0.5055 and 0.3366 mmol g^{-1}; ethylene 0.7531 and 0.5091 mmol g^{-1}; propane 1.316 and 0.8214 mmol g^{-1}; propylene: 1.9819 and 1.3757 mmol g^{-1}; acetylene 1.4241 and 0.9429 mmol g^{-1}; carbon monoxide 0.0667 mmol g^{-1} at 30 °C; nitrogen 0.0484 mmol g^{-1} at 30 °C. Padin and Yang[32] reported the adsorption of ethylene at 1 atm and 70 °C: 0.53 mmol g^{-1} at silica (670 $m^2\ g^{-1}$, pore volume 0.46 $cm^3\ g^{-1}$), and 0.32 mmol g^{-1} at silica (398 $m^2\ g^{-1}$). Ethylene adsorption on silica was up to 1.6 mmol g^{-1} at 0 °C and 800 mm Hg.[33] Data on ethylene adsorption on silica at temperatures 0, 25, 40, 142, 175 and 226 °C have also been reported.[33] (These empirical facts have been almost completely neglected by polymer scientists who have made efforts to identify the active sites in the Cr/SiO_2 system.)

Although chromium is fully attached at 300 °C during the thermal treatment of silica with a Cr precursor, the subsequent polymerizing activity of CrO_x/SiO_2 continues to increase right up to the point of silica sintering at a high temperature.[8] Silica sintering is a consequence of stress and strain relaxation. Sintering destroys the surface area and the porosity of the silica. Hence, the ability of silica to adsorb ethylene should decrease. Consequently, the polymerization activity increases with increasing calcination temperature up to a maximum at around 925 °C, and then declines.[8] (A similar result was obtained in the case of propylene adsorption and polymerization by classical supported ZN titanium catalysts.[34] The adsorptivities of various supports, without a titanium precursor, were determined

after calcination at different temperatures in the range of 100–1000 °C. It was found that the maximum values of adsorptivities were obtained after heat treatment of the support at 300–400 °C. Also, supports previously loaded with titanium precursor were calcinated separately in the same temperature range 100–1000 °C. So-prepared catalysts were used for propylene polymerization. It was found that supports calcinated at 300–400 °C exhibited the maximum polymerization activities. It was concluded that there was a parallelism of support adsorptivity and its catalytic activity, *i.e*., the maximum adsorptivity of an unloaded support corresponded to a maximum polymerizability of a titanium loaded support.)[34]

But, why does ethylene adsorbs on silica? The answer is: silica helps ethylene to partially deliberate its free energy as heat of adsorption, the value of which decreases from 32 to 16 kJ mol^{-1} with increasing coverage.[31] A nuclear magnetic resonance study confirmed that there are deformations in the electronic and geometric structure of ethylene adsorbed on zeolite, as well as the orientation of ethylene molecule due to neighboring molecules.[35] More recent data confirmed that there are several chemisorbed species of ethylene adsorbed on all the studied surfaces.[36–39] Physically adsorbed and ordered di-σ-bonded ethylene with a molecular plane parallel to a platinum surface was formed at low coverage. With increasing coverage, chemisorbed π-bonded ethylene intrudes into di-π-bonded ethylene layer onto the surface. The π-bonded ethylene is concluded to have its molecular plane tilted while the C=C bond remains parallel to the surface of platinum and silver.[38] In other words, the π-electrons are partially localized on the C atoms, the double bond is extended thus enabling a higher mobility of the CH_2 groups, but the movement of the ethylene molecule as a whole is restricted. (Very similar changes were noticed in the case of propylene adsorption, *i.e*., chemisorption of the first monolayer induces the rehybridization of the double bond in propylene towards a significant single character.[40] The C=C bond length of propylene in the gas phase is 0.133 nm, but that of chemisorbed propylene is 0.148 nm, thus approaching the single C–C bond length of 0.154 nm, with a concomitant significant reduction of the double bond character.[41] The extension of chemical bonds of adsorbed molecules is a typical phenomenon observed in adsorption processes).[36]

There is a great negative change of entropy if the free ethylene molecules have to be polymerized. This is the “limiting force” of the polymerization kinetics. The support also aids ethylene to partially solve this problem. Typically, a dependence of heat of adsorption with coverage is usually observed to display three regions, namely the adsorbent–adsorbate interaction, followed by the adsorbate–adsorbate interaction and finally by condensation.[31] Consequently, the entropy of adsorbed ethylene decreases with the coverage, (θ), approaching a minimum value when a monomer monolayer is completed, *i.e*., at the coverage $\theta = 1$.[33] Low entropy means that the ethylene molecules are organized at the surface of

the support. Such organized molecules have less to lose if they should polymerize. Hence, the entropy of polymerization of organized monomers should have a small negative value and the "limiting force" could be overcome. The molecular distortion, the reduced mobility and the self-assembling of the ethylene molecules are prerequisites for ethylene polymerization and they are achieved with the help of the support.[17] (The same prerequisites can be achieved by compression of ethylene gas. In this case, polymerization by the free radical mechanism is possible, but only under low entropy conditions in which different supramolecular ethylene species are present.)[10,42−44]

The importance of monomer adsorption for its polymerization was recognized immediately after the discovery of ZN catalysts and was discussed extensively.[17,45,46] According to our knowledge, there was no thorough research of monomer adsorption on the surface of supports that are used in ZN and Phillips polymerizations in order to explain their mechanism, since very soon after their discovery, the insertion mechanism was proposed and generally accepted. On the other hand, there are many investigations on olefin (ethylene, propylene, butylene-1, butylene-2, 1,4-pentadiene) adsorption on the various supports (metals, metal oxides, silica, aluminum oxide, aluminosilicates, *etc*.) important for olefin hydrogenation, oxidation, isomerization and other reactions.[47]

Today, the surface science of adsorption has advanced and approached many rules, findings and statements.[36] They are also of a great value for the interpretation of olefin polymerization, since according to the CPM that will be presented here, it is necessary to have monomer molecules adsorbed on the surface of a support. When the surface of some support is exposed to adsorption of some molecules, a surface film of adsorbate is formed. Two types of interactions contribute to the formation of a surface film: 1) the interactions (electronical and geometrical) between the support and molecule of adsorbate and 2) the lateral interactions between the adsorbed molecules. The evolution of a film depends on the coverage and time. The structure of the film and the orientation of the adsorbed molecules depend on the type of the dominating interactions and on the surface area available to each adsorbing molecule. If the coverage is low and the available area per adsorbing molecule is large, a disordered two-dimensional gaseous phase is formed. Each molecule of adsorbate is oriented to the surface occupying a relatively high surface area. The gas possesses neither short-range nor long-range order and there is little interaction between the adsorbed molecules. As the coverage increases, the available area decreases and a phase transition occurs into a two-dimensional liquid-like phase. Liquids exhibit short-range but no a long-range order. Further adsorption reduces the available area of the support and transforms the adsorbate film into a solid-like phase. The molecules stand up straight toward the surface because thus they occupy a minimum space on the surface. The types of condensed adsorbed phases which can be formed de-

pend greatly on the intermolecular interactions adsorbate–adsorbent and within the film, *i.e.*, lateral interactions between the adsorbate molecules. The lateral interactions are responsible for the formation of a two-dimensional ordered solid phase. The degree of ordering depends on the coverage, exposure time and the strength of the intermolecular interactions. The adsorbate undergoes self-assembling, *i.e.*, phase transition from a disordered phase into an ordered phase. If the adsorbate is appropriate and if sufficient time is given, the system locks into a final structure which is well-ordered. The self-assembling is enhanced by the presence of some nucleation centers, *i.e.*, surface defects or some nucleating agents (*e.g.*, metal ions). Once the ordered phase is formed, it does not spontaneously revert to a disordered phase.

Thus, it can be realized how olefins are adsorbed on a support. The gradual formation of a monomer monolayer is realized by a simultaneous change in the orientation of the molecules and degree of order, as was demonstrated for many other substances.[36] The role of support is to deform the monomer molecules as well as to concentrate and to orient them properly, thus facilitating their polymerization.

THE CHARGE PERCOLATION MECHANISM (CPM)

Based on the theory of the polymerization of organized monomers proposed by Semenov, Kargin and Kabanov,[45,46] which was applied to explain free radical polymerization of compressed ethylene gas[10,42–44] and liquid methyl methacrylate,[48] and based on an analysis similar to that presented in the previous section, the charge percolation mechanism (CPM) was suggested and applied it to explain olefin polymerization in ZN systems.[9–13] Here the CPM is adopted to explain ethylene polymerization in the presence of the Cr/SiO_2 system.

Starting from Cr(VI) precursors, after immobilization on silica, thermal treatment and addition of ethylene (or CO), immobilized Cr(II) species are produced (Figs. 1 and 2). After the oxidative addition of ethylene to the Cr(II) species, the various Cr(IV) species are formed. Both species, *i.e.*, Cr(II) and Cr(IV), exist simultaneously on the support.

The species Cr(IV) and Cr(II) are unstable. There is a tendency to equalize their oxidation states to Cr(III) by charge transfer from Cr(II) to Cr(IV), but it cannot be done since they are immobilized and highly separated on the support. However, the monomer molecules can help. It is well known that ethylene molecules are gradually adsorbed on silica, producing a layer of adsorbate even in the absence of Cr or any other transition metal.[31–33] The immobilized Cr(II) to Cr(IV) species on the support are gradually surrounded by an adsorbed monomer film. A cluster of monomer, with overlapped π-bonds, connects two immobilized Cr species (Fig. 3, top). Once the bridge is completed (the moment of percolation), a charge transfer occurs. The terminal monomer molecules, adjacent to Cr(IV) and Cr(II), are inserted into their vacancies, making π-complexes with them, if the

shape and size of the monomer molecule are in accordance with the vacant spaces of the active centers. Thus, monomer molecules form a bridge consisting of a π-electron cloud between the Cr(IV) and Cr(II). The whole π-electron cloud in the monomer cluster will be pulled toward Cr(IV), since it has a more positive charge than Cr(II). Thus, the monomer cluster is excited, *i.e.*, the π-electrons are displaced toward Cr(IV), producing a partially negative charge toward Cr(IV) side. This displacement of π-electrons attracts a proton from the alkyl group of Cr(IV) to terminal monomer molecule, leaving an electron pair on the alkyl group. Simultaneously, a partially positive charge is formed on the terminal monomer molecule coordinated to Cr(II), a proton from the terminal monomer molecule is repelled to Cr(II). The electron pair on the left terminal monomer molecule enables the simultaneous polymerization of all monomer molecules belonging to the bridge between Cr(II) and Cr(IV). Both Cr species equalize their oxidation states simultaneously with the polymerization of monomer (Fig. 3, bottom). The polymer chain is removed from the support making its surface free for subsequent monomer adsorption. The whole process is repeated by the oxidation–reduction of some other Cr(II)–Cr(IV) ensembles immobilized on the support.

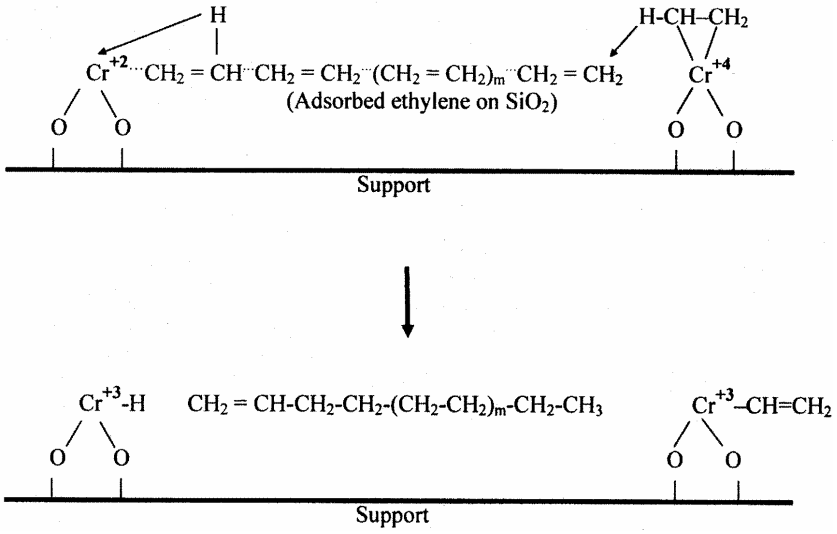

Fig. 3. An elementary step of the charge percolation mechanism.

Any of the Cr(II) and Cr(IV) species presented in Figs. 1 and 2 could be the active center. After charge percolation, various alkylated Cr(III) species could be formed, depending on the type of the alkyl group.

As the results of the process, unstable species Cr(II) and Cr(IV) are deactivated since they are transformed to the more stable green Cr(III) species, as was experimentally confirmed.[4,7,49,50] Monomer adsorption and its polymerization is a device for charge percolation between Cr(II) and Cr(IV), whereby the oxidation

state of the Cr atoms is homogenized. The polymerization is not possible without this kind of deactivation and this type of deactivation is not possible without the polymerization of the monomer. Both processes, *i.e.*, homogenization of the oxidation state of Cr and ethylene polymerization, are mutually interdependent acts, neither possible without the other.

The support plays a very important role. It offers the sites to bring both components together, by immobilization of Cr and by adsorption of monomer. Thanks to the support, it is possible that both reactions (the oxidation–reduction of Cr and the polymerization of monomer) are merged and performed at the same location, simultaneously, in a common process. Simultaneously, strain relaxation and fragmentation of the support occur due to the heat evolved in these processses. Furthermore, once both reactions are completed, a part of the support becomes free for subsequent monomer adsorption.

SIMILARITY OF THE CPM WITH SOME EXISTING EXPLANATIONS

Estimating the situation in the 1970s in his famous book "Ziegler–Natta Catalysts and Polymerizations" Boor stated: "Each worker has examined some aspect of the problem and has given his view of what is happening. The findings are similar to pieces of a puzzle which are coupled to form the whole picture; only here, some critical pieces are still missing".[51] In the previous section, it has been shown that the CPM gives the critical pieces asked for by Boor.

It seems that the CPM is something quite new and not known in current chemistry. This is not true.

A quite similar mechanism, however, was proposed very soon after the discovery of ZN and Phillips polymerizations. Friedlander and Oita[52] and Kargin and Kabanov[46] suggested that propagation occurs by the addition of adsorbed olefin molecules to an active center (Fig. 4). They also proposed that the polymer chains are detached from the support, thus making some adsorption sites free for subsequent monomer adsorption. They believed, however, that a polymer chain propagates by a radical or ion–radical mechanism. Since the presence of radicals was not confirmed, this mechanism was rejected, together with the proposal that the adsorbed monomer molecules were enchained.

It was proposed by Rebenstorf and Larsson[53] that the initiation reaction for the polymerization of ethylene could be the addition of one ethylene molecule to one dinuclear surface chromium complex by the formation of a $Cr–CH_2–CH_2–Cr$ bridge. More recent theoretical calculations showed that there was a slight bias toward Cr(II)−Cr(IV) over the Cr(III)−Cr(III) ensembles as active centers.[54] This is very similar to the proposal made by the CPM.

Similar electron transfer reactions between two transition metal atoms by a ligand bridge, which includes a transition metal oxidation–reduction and a chemical transformation of the ligand bridge, are described in inorganic chemistry as mutually interdependent acts.[55] In the case of olefin polymerization by the CPM, the bridging group is a monomer cluster between two Cr active centers.

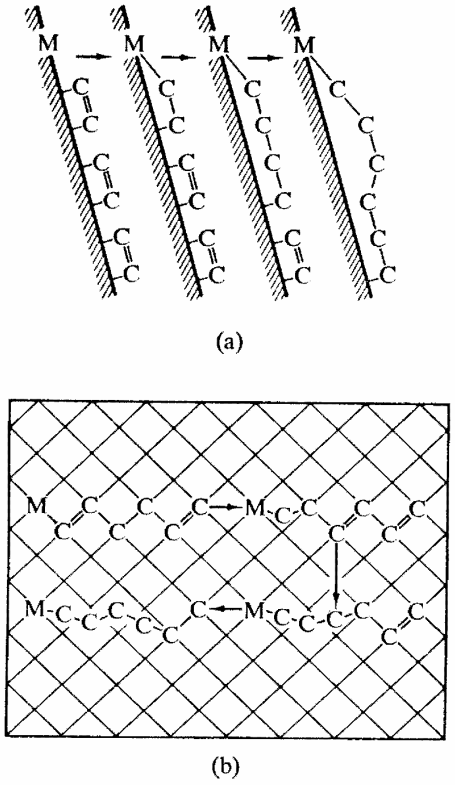

Fig. 4. Replica polymerization mechanism proposed by Friedlander and Oita[52] (a – cross section; b – surface view).

Also, the proposed CPM is quite similar to reactions catalyzed by enzymes, which are also highly entropy dependant. An enzyme usually contains an acid and some base residues. The high effectiveness of the action of an enzyme is often explained by the simultaneous action of these groups by the transfer of a proton from an acid group to a reacting substrate and a proton from the substrate to the base group ("push-pull" mechanism).[56] The mechanism of natural polymer synthesis, *i.e.*, proteins and DNA replication performed by enzymes are quite similar to the CPM of synthetic polymer synthesis by a supported transition metal complexes and a self-assembling adsorbed monomer.

CONCLUSIONS

The CPM includes three basic participants, *i.e.*, ethylene, chromium precursors and supports, in three mutually interdependent acts, *i.e.*, ethylene polymerization, chromium deactivation by oxidation–reduction and silica strain relaxation. The CPM is in good agreement with the experimental data on the polymerization of ethylene by supported CrO_x systems. It gives reasonable answers on all open questions mentioned in the introduction: (1) the active centers are Cr(II) and

Cr(IV) ensembles; (2) the mechanism of initiation includes the coordination of ethylene molecules with CrO_x species and the reduction of Cr(VI) to Cr(IV) and to Cr(II) (Fig. 1); (3) the polymerization is performed by the charge percolation mechanism proposed for supported CrO_x as well as for other Ziegler–Natta polymerizations by transition metals (Fig. 3); (4) the diversity of the Cr oxidation state (Figs. 1 and 2) and the tendency to stabilize them to Cr(III) is the "driving force" for polymerization.

The answers on the other open questions listed in the introduction, *i.e.*, 5., 6. and 7., as well as more evidence of the validity of the CPM will be given in a subsequent article (Part VII of this work).[14]

И З В О Д

МЕХАНИЗАМ ПОЛИМЕРИЗАЦИЈЕ ПЕРКОЛАЦИЈОМ НАЕЛЕКТРИСАЊА И СИМУЛАЦИЈА ЦИГЛЕР–НАТА ПОЛИМЕРИЗАЦИЈЕ. ДЕО 6. МЕХАНИЗАМ ПОЛИМЕРИЗАЦИЈЕ ЕТИЛЕНА ПОМОЋУ ОКСИДА ХРОМА НА НОСАЧУ

ДРАГОСЛАВ СТОИЉКОВИЋ[1], БРАНКА ПИЛИЋ[1], МИША БУЛАЈИЋ[2], НЕБОЈША ЂУРАСОВИЋ[2] и НИКОЛАЈ ОСТРОВСКИ[3]

[1]Технолошки факултет, Универзитет у Новом Саду, Булевар Цара Лазара 1, 21000 Нови Сад, [2]ХИП–Петрохемија, 26000 Панчево и [3]ХИПОЛ, 25250 Оџаци

Упркос обимним истраживањима у протеклих 50 година, остала су без одговора многа питања о полимеризацији етилена помоћу оксида хрома на носачу. Стога се у овом раду разматрају основне поставке ове полимеризације. Показано је да се и у овом случају могу наћи одговори помоћу механизма перколације наелектрисања, којег смо недавно предложили за полимеризацију олефина применом Циглер–Ната комплекса прелазних метала.

(Примљено 27. октобра 2006, ревидирано 13. јуна 2007)

REFERENCES

1. P. Hogan, *J. Polym. Sci., Part A-1*, **8** (1970) 2637
2. E. J. Arlman, *J. Catal*. **3** (1964) 89
3. P. Cossee, *J. Catal.* **3** (1964) 80
4. E. Groppo, C. Lamberti, S. Bordiga, G. Spoto, A. Zecchina, *Chem. Rev*. **105** (2005) 115
5. B. M. Weckhuysen, R. A. Schoonheydt, *Catal. Today* **51** (1999) 215
6. B. Liu, M. Terano, *J. Mol. Catal. A: Chem*. **172** (2001) 172
7. B. Liu, H. Nakatani, M. Terano, *J. Mol. Catal. A: Chem*. **184** (2002) 387
8. M. P. McDaniel, *Adv. Catal*. **33** (1985) 47
9. D. Stoiljković, B. Pilić, S. Jovanović, D. Panić, in *Current Achievements on Heterogeneous Olefin Polymerization Catalysts*, M. Terano, Ed., Sankeisha Co., Nagoya, 2004, p.135
10. D. Stoiljković, B. Pilić, R. Radičević, I. Bakočević, S. Jovanović, D. Panić, Lj. Korugić–Karasz, *Hem. Ind*. **58** (2004) 479
11. B. Pilić, D. Stoiljković, I. Bakočević, S. Jovanović, D. Panić, Lj. Korugić–Karasz, in *New Polymeric Materials*, Lj. Korugić–Karasz, W. MacKnight and E. Martuscelli, Eds., ACS Symp. Series, New York, 2005, p. 215
12. B. Pilić, D. Stoiljković, I. Bakočević, S. Jovanović, D. Panić, Lj. Korugić–Karasz, *J. Serb. Chem. Soc.* **71** (2006) 357

13. B. Pilić, D. Stoiljković, I. Bakočević, S. Jovanović, D. Panić, Lj. Korugić–Karasz, *Mat. Sci. Forum* **518** (2006) 381
14. D. Stoiljković, B. Pilić, M. Bulajić, N. Đurasović, N. Ostrovski, *J. Serb. Chem. Soc.*, in press
15. H. Berthod, *Ann. Chim.* **6** (1961) 286
16. E. Hunter, in *Polythene*, A. Renfrew, P. Morgan, Eds., Iliffe and Sons Ltd., London, 1957, Chapter 3
17. N. G. Geylord, H. F. Mark, *Linear and Stereoregular Addition Polymers*, Interscience Publishers, New York, 1959, Chapter 3
18. A. B. Gaspar, J. L. F. Brito, L.C. Dieguez, *J. Mol. Catal. A: Chem.* **203** (2003) 251
19. A. B. Gaspar, R. L. Martins, L. C. Dieguez, *J. Mol. Catal. A: Chem.* **169** (2001) 105
20. A. B. Gaspar, L. C. Dieguez, *Appl. Catal.: A. General* **227** (2002) 241
21. P. Hogan, in *Polyethylenes*, The Plastics and Rubber Institute, London, 1983, Chapter B3.1
22. E. Groppo, C. Prestipino, F. Cesano, F. Bonino, S. Bordiga, C. Lamberti, P. C. Rhune, J. W. Niemantsverdriet, A. Zecchina, *J. Catal.* **230** (2005) 98
23. B. M. Weckhuysen, A. A. Verbreckmoes, A. R. De Baets, A. Schoonheydt, *J. Catal.* **166** (1997) 160
24. A. B. Gaspar, L. C. Diegiez, *J. Mol. Catal. A: Chem.* **219** (2004) 357
25. B. Liu, P. Šindelár, Y. Fang, K. Hasebe, M. Terano, *J. Mol. Catal. A: Chem.* **238** (2006) 142
26. S. Scott, J. A. N. Ajjou, *Chem. Eng. Sci.* **56** (2001) 4155
27. E. Groppo, C. Lamberti, G. Spoto, S. Bordiga, G. Magnacca, A. Zecchina, *J. Catal*. **236** (2005) 233
28. E. Groppo, C. Lamberti, S. Bordiga, G. Spoto, A. Zecchina, *J. Catal*. **240** (2006) 172
29. F. Aubriet, J.–F. Muller, C. Poleunis, P. Bertrand, P. Di Groce, P. Grange, *J. Am. Soc. Mass Spectrom*. **17** (2006) 406
30. M. A. Landau, V. V. Shchekin, *Neftekhimiya* **3** (1963) 713
31. B. L. Newalkar, N. V. Choudary, U. T. Turaga, R. P. Vijayalakshmi, P. Kumar, S. Komarneni, T. S. G. Bhat, *Micropor. Mesopor. Mater.* **65** (2003) 267
32. J. Padin, T. Yang, *Chem. Eng. Sci.* **55** (2000) 2607
33. K. L. Mentell, in *Ethylene and Its Industrial Derivates*, S. A. Miller, Ed., E. Benn, London, 1969, Chapter 7
34. A. Simon, A. Grobler in *Makro Mainz – 26*th *Int. Symp. Macromol*., I. Lüderwald and R. Weiss, Eds., Vol. I, IUPAC, Mainz, 1979, ch. A2–39
35. G. M. Muha, D. J. C. Yates, *J. Chem. Phys.* **49** (1968) 5073
36. K. W. Kolasinski, *Surface Science – Foundation of Catalysis and Nanoscience*, John Wiley and Sons, Chichester, 2002, p. 270
37. U. Müller, U. Schmiemann, A. Dülberg, H. Baltruschat, *Surf. Sci*. **335** (1995) 333
38. J. Kubota, S. Ichihara, J. N. Kondo, K. Domen, C. Hirose, *Surf. Sci*. **357–358** (1996) 634
39. L. Clemen, R. M. Wallace, P. A. Taylor, M. J. Dresses, W. J. Choyke, W. H. Weinberg, J. T. Yates, *Surf. Sci.* **268** (1992) 205
40. F. Zaera, D. Chrysostomou, *Surf. Sci*. **457** (2000) 71
41. A. Valcárcel, J. M. Ricart, A. Clotet, A. Markovits, C. Minot, F. Illas, *Surf. Sci*. **519** (2002) 150
42. D. Stoiljković, S. Jovanović, *J. Polym. Sci: Polym. Chem. Ed*. **19** (1981) 741
43. D. Stoiljković, S. Jovanović, *Angew. Makromol. Chem.* **106** (1982) 195
44. D. Stoiljković, S. Jovanović, *Acta Polymerica* **39** (1988) 670
45. N. N. Semenov, *Khim. Tekhnol. Polimerov* **7–8** (1960) 196
46. V. A. Kargin, V. A. Kabanov, *Zh. Vses. Khim. Ob*. **9** (1964) 602
47. H. P. Leftin, M. C. Hobson, in *Advances in Catalysis*, D. D. Eley, H. Pines, P. B. Weisz, Eds., Vol. 14, Academic Press, New York and London, 1963–1964, p. 115
48. R. Radičević, Lj. Korugić, D. Stoiljković, S. Jovanović, *J. Serb. Chem. Soc.* **60** (1995) 347

49. J. P. Hogan, *J. Polym. Sci. A-1* **8** (1979) 2637
50. O. M. Bade, R. Blom, M. Dahli, A. Karlsson, *J. Catal.* **173** (1998) 460
51. J. Boor, *Ziegler–Natta Catalysts and Polymerizations*, Academic Press, New York, 1979
52. H. N. Friedlander, K. Oita, *Ind. Eng. Chem.* **49** (1957) 1885
53. B. Rebenstorf, R. Larsson, *J. Mol. Catal*. **11** (1981) 247
54. O. Espelid, K.J. Borve, *J. Catal*. **206** (2002) 331
55. F. A. Cotton, G. Wilkinson, *Advances Inorganic Chemistry, 5th ed.*, John Wiley and Sons, New York, 1988, p. 1311
56. G. M. Panchenkov, V. P. Lebedev, *Chemical Kinetics and Catalysis*, Mir Publishers, Moscow, 1976, p. 542.